Experimental and Numerical Characterization of Ion-Cyclotron Heated Protons on the Alcator C-Mod Tokamak

by

Vincent Tang

Submitted to the Department of Nuclear Science and Engineering
in partial fulfillment of the requirements for the degree of
Doctor of Philosophy in Applied Plasma Physics
at the
MASSACHUSETTS INSTITUTE OF TECHNOLOGY
August 2006
[September 2006]

Author .....
Department of Nuclear Science and Engineering
Aug 10, 2006

Certified by .....
Ronald R. Parker
Professor, Department of Nuclear Science and Engineering
Thesis Supervisor

Certified by .....
Paul T. Bonoli
Principal Research Scientist, Plasma Science and Fusion Center
Thesis Reader

Certified by .....
Robert S. Granetz
Principal Research Scientist, Plasma Science and Fusion Center
Thesis Reader

Certified by .....
John C. Wright
Research Scientist, Plasma Science and Fusion Center
Thesis Reader

Accepted by .....
Jeffrey A. Coderre
Chairman, Department Committee on Graduate Students

Experimental and Numerical Characterization of Ion-Cyclotron Heated Protons on the Alcator C-Mod Tokamak

by

Vincent Tang

Submitted to the Department of Nuclear Science and Engineering
on Aug 10, 2006, in partial fulfillment of the
requirements for the degree of
Doctor of Philosophy in Applied Plasma Physics

Abstract

Energetic minority protons with ~100 keV effective temperature are routinely created in Alcator C-Mod plasmas with the application of ICRF. A new multi-channel Compact Neutral Particle Analyzer is used to make measurements of these distributions in Alcator C-Mod's unique and reactor-relevant operating space via an active charge-exchange technique (CX). Using a detailed model that accounts for beam, halo, and impurity CX, core proton temperatures of ~30-120 keV are directly measured for the first time in lower density ($n_{e0} \sim 0.8 - 1.5 \times 10^{20}/\mathrm{m}^3$) Alcator C-Mod plasmas using only ~0.5 MW of ICRF power. The model found that the minority proton temperatures are peaked spatially away from r/a=0, even for an on-axis resonance. Additionally, noticeable phase-space anisotropy is seen as expected for ICRF heating. The measured effective temperatures scale approximately with the Stix parameter. The CNPA measurements are also compared with several leading simulation packages. Preliminary comparisons with results from the AORSA/CQL3D Full-wave/Fokker-Planck (FW/FP) code using a new synthetic diagnostic show good agreement and demonstrate that these complex codes are required to simulate Alcator C-Mod's energetic minority populations with accuracy. These FW/FP analyses represent the first comparison between predictions of such detailed codes and extensive minority ion experimental measurements.

Thesis Supervisor: Ronald R. Parker
Title: Professor, Department of Nuclear Science and Engineering

Thesis Reader: Paul T. Bonoli
Title: Principal Research Scientist, Plasma Science and Fusion Center

Thesis Reader: Robert S. Granetz
Title: Principal Research Scientist, Plasma Science and Fusion Center

Thesis Reader: John C. Wright
Title: Research Scientist, Plasma Science and Fusion Center

Acknowledgments

I must first thank Professor Ron Parker for being both my academic and project supervisor during my S.M. and Ph.D. degrees. His expertise in all matters contributed significantly to all aspects of my education. I also thank him for the faith he had in me when I decided to undertake this difficult and experimentally oriented topic for my doctorate. Also, many thanks to Carolyn Parker for the delicious meals my wife and I took advantage of. I also express thanks to Professor Jeff Freidberg for his insights and time, and Professor Hutchinson for his plasma diagnostics knowledge.

In the later part of the thesis, I had the privilege of working extensively with Drs. Paul Bonoli and John Wright. Without them and their SciDac team, the comparison of my data with cutting edge numerical simulations would not have been possible. Many thanks also to Drs. Bob Harvey at CompX and Fred Jaeger at ORNL for providing some of the simulation results in this thesis. Lastly, I also owe thanks to Dr. Peter Catto for his expertise in theory.

Concerning the scientists on the experimental side, I am indebted to Drs. Catherine Fiore, Bob Granetz, Martin Greenwald, Amanda Hubbard, Jerry Hughes, Jim Irby, Brian Labombard, Yijun Lin, Earl Marmar, John Rice, Bill Rowan, Steve Scott, Joe Snipes, Jim Terry, Steve Wolfe, and Steve Wukitch. I would also like to thank R. Petrasso and his HEDP group for the use of their deuterium beam. I am grateful to both Bob and Steve S. for ensuring the success of the new Diagnostic Neutral Beam (DNB), which I took full advantage of. They were both also very generous with their time. John Rice provided invaluable experimental help, whether in the form of an unique micrometer-controlled aperture or experimental neutral density data. I thank Joe Snipes for his willingness to discuss with me at length his TAE project. I am grateful to both Jim T. and Brian for their assistance when aspects of my project took me to unfamiliar territory, such as impurity density measurements and edge neutral phenomena. Thanks also to Amanda for keeping the ECE diagnostics running smoothly during my run days. As for Catherine, she spent an invaluable amount of time with me resurrecting the Alcator Calibration Neutral Beam, and was always available when I needed a NIM module or a sodium iodine detector. I am thankful to Jim I., Earl, and Steve Wolfe for the large amount of run time made available for this project. Finally, Jerry, who was both a student and a scientist during my stay, answered all the questions I had that might have been too embarrassing to ask a senior scientist.

As for my fellow graduate students and friends, I owe them many thanks. Working

day-to-day with John Liptac alleviated a lot of the pain associated with any Ph.D. project. In between routing cables and wondering why a certain CQL3D namelist failed, we had fascinating conversations with topics ranging from the political aspects of fusion energy to the role of religion in daily life. Sharing an office with Tim Graves was equally enlightening; his optimistic assessment of every problem was usually correct. Natalia Krasheninnikova was always available for a tough plasma physics question or just a cup of coffee. Jen Ellsworth provided a friendly ear for working out all my professional hang-ups. I also had the pleasure of interacting personally and professionally with Brock Bose, Alex Boxer, Eric Edlund, Marco Ferrara, Alex Ince-Cushman, Istak Karim, Jinseok Ko, Alex Kouznetsov, Davis Lee, Liang Lin, Ken Marr, Rachael McDermott, Eugene Ortiz, Alex Parisot, Matt Reinke, Andréa Schmidt, Jason Sears, Balint Veto, Greg Wallace, Howard Yuh, and Kirill Zhurovich.

The excellent staff at the PSFC also deserves recognition. To note, Ed Fitzgerald, Rich Danforth, Mark Iverson, Bob Silvia, Bill Keating, and Charlie Cauley manufactured parts of my diagnostic and taught me invaluable machining skills. I also had a lot of help from Bill Parkin, Dave Bellofatto, Wade Cook, and Maria Silveira at the Electronic Shop. Bob Childs, Tom Toland, and Ron Rosati at the Vacuum Shop were always on top of my vacuum needs. Many thanks also to Dexter Beals who kept the DNB running! My computing troubles were always handled professionally by Don Nelson and Henry Bergler. Lastly, I am grateful to Valerie Censabella, Megan Tabak, and Corrinne Fogg for fulfilling my administrative needs rapidly.

I would not be at this point without my family. Specifically, I am grateful to my parents and grandparents for their unconditional support during this difficult undertaking. To my wife Lily, I am forever thankful for your unending love, encouragement, and support, without which this would not have been possible.

Contents

List of Figures

List of Tables

Chapter 1

Introduction

With the potential of providing limitless clean energy, controlled nuclear fusion remains a holy grail of physics and engineering. Now more than ever, the possibility of a fusion reactor is realistically within sight. The conclusion of site negotiations for the International Thermonuclear Experimental Reactor (ITER)[1], shown in Figure 1-1, opens the path to demonstrating the feasibility of commercial fusion power. ITER is both a physics and engineering experiment, as it allows scientists to study fusion reactor physics that current machines are just on the fringe of, which requires assembling a reactor size fusion device.

The work presented in this thesis is composed of experimental and modeling results performed on the Alcator C-Mod Tokamak[2], an experiment that operates at some of the same parameters as ITER. The effort involves diagnosis of energetic particles created from plasma heating, and comparisons with theory. These are active research areas in fusion plasma physics, and ultimately relate to the viability of fusion as a commercial power source.

In order to explain further the motivation and scope of the research in this thesis, a review of fusion energy and the tokamak approach is first given. A comprehensive overview of both is available from Wesson[3]. The next section introduces the area of plasma heating, specifically the Ion-Cyclotron-Range-of-Frequency (ICRF) minority heating scheme, and provides details on the research performed for this thesis. Following this is a description of the Alcator C-Mod tokamak at the MIT Plasma Science and Fusion Center, and a detailed outline of the thesis.

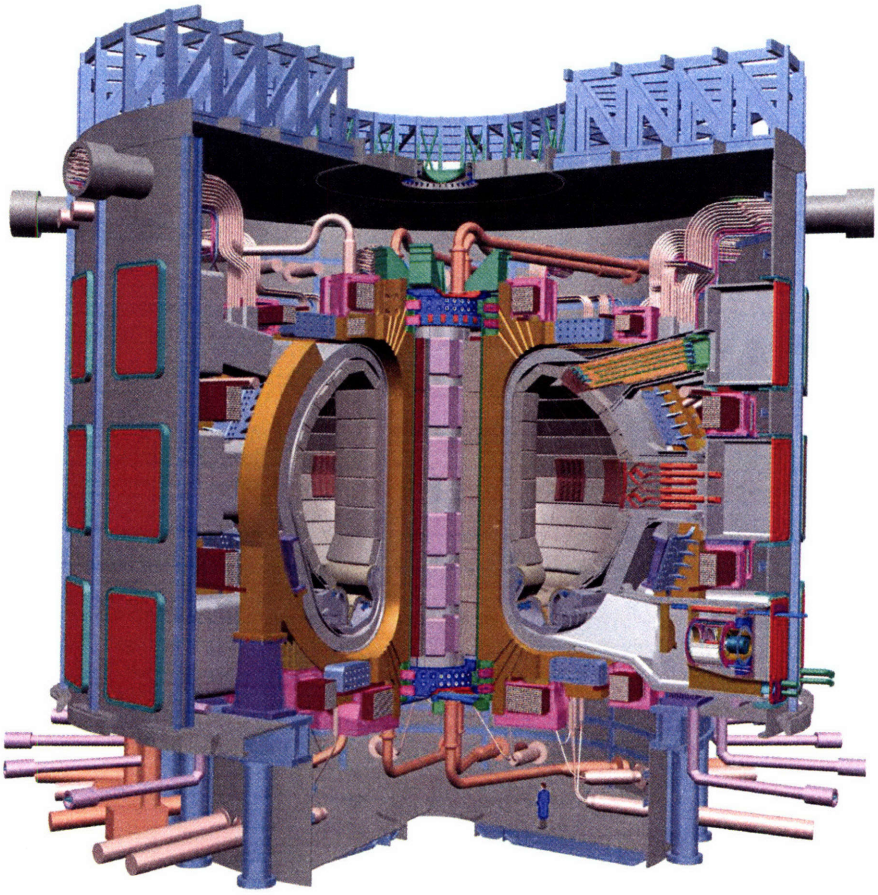

Figure 1-1: The International Thermonuclear Experimental Reactor. (From the ITER site[1])

1.1 Fusion Energy

Physically, the bases of any near-term fusion device are the following exothermic reactions:

$D + T \rightarrow He^4 + n + 17.6MeV$

$D + D \rightarrow He^3 + n + 3.27MeV$

$D + D \rightarrow T + H + 4.03MeV$

$D + He^3 \rightarrow He^4 + H + 18.3MeV$

The cross sections for these processes are shown in Figure 1-2. The two D-D reactions have essentially the same cross section. Because the D-T cross section is significantly higher than the D-D and D-He^3 reactions, it is considered the choice for first generation fusion reactors. Tritium is not naturally occurring, but can be bred using the D-T produced neutron via:

$Li^6 + n \rightarrow He^4 + T + 4.8MeV$

$Li^7 + n \rightarrow He^4 + T + n - 2.5MeV$

Conceptually, a D-T fusion reactor is thus simply a fusion reaction volume surrounded by a $\sim$1 m thick neutron blanket designed to moderate and absorb 14.1MeV neutrons. Additionally, depending on the reactor concept, the energy from the 3.5 MeV α particle is typically released with very short range radiation that heats the blanket's chamber facing wall (i.e. the first wall). The fusion power is then transferred out of the blanket through heat exchangers.

The Li^6 reaction has a much higher cross section than the Li^7 reaction at thermal energies. Typically, D-T neutrons are first moderated in the blanket module, than captured by Li^6 for tritium breeding. Different fast neutron multipliers can be inserted into the front of the blanket to ensure an adequate neutron supply for breeding.

Therefore, from an abstract and fuel cycle point of view, a fusion reactor is not difficult to fathom. The challenge, however, lies in the physics of initiating and sustaining the fusion reaction volume.

Because of Coulombic repulsion, the D-T, D-D, and D-He^3 fusion reactions only occur when the reactants have energies in the multi-keV range. This is clearly shown in Figure 1-2. At these energies the cross sections start to become significant because of tunneling through the Coulomb barrier. These required energies suggest that at least one of the reactants must be in the form of a plasma or beam. Thus, one idea that immediately comes to mind for a fusion reactor is to simply shoot a deuterium beam into a tritium or deuterium loaded target; however, further analysis shows this approach to be unworkable. As it turns out, the scattering cross section is always

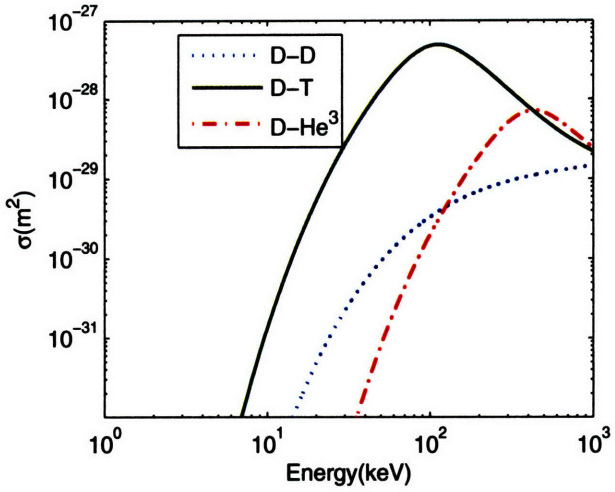

Figure 1-2: Cross sections for various fusion reactions. The D-D curve represents the sum of the two possible reactions.

much higher than the fusion cross section; most of the beam energy goes into heating of the target, and a net power output can not be achieved.

Hence, the key to a viable fusion reactor has always been the requirement of holding together a sufficiently dense neutral plasma long enough and at high enough temperatures for sufficient nuclear fusion reactions to occur. This is known as thermonuclear fusion. Simply, the ions must be physically and energetically confined through many scattering collisions so that they have a chance to fuse. Macroscopically, this requirement is known in the simplest form as the Lawson criterion[4], based on a simple steady-state power balance for the plasma:

$$n_1 n_2 \langle \sigma v \rangle f + P_{\text{in}} = \frac{3 n_e k_b T_e}{\tau_E} + P_{\text{loss}} \tag{1.1}$$

where n_1, n_2 are the densities of the fuel ions, multiplied by $1/2$ if n_1 and n_2 are the same species. $\langle \sigma v \rangle$ is the reactivity of the fuel ions averaged over the reactant velocity distributions, and can be approximated for the D-T reaction in the keV range as $< \sigma v >= 1.1 \times 10^{-24} T^2$ m^3/s, with T in keV, and f is the amount of fusion energy deposited into the plasma-typically 3.5 MeV per fusion reaction for D-T, since only the α particle is confined. P_{in} refers to any externally applied heating power per unit volume. The 14.1 MeV neutrons produced in D-T fusion escape the plasma readily but are absorbed in the tritium breeding blanket, as mentioned above. The first term on the right represents bulk plasma thermal losses, characterized by the

energy confinement time τ_E. An ideal equilibrated plasma with Z_{eff}=1 is assumed for simplicity. Additional losses such as bremsstrahlung and line radiation are represented by P_{loss}. These energy losses again heat the first wall of the surrounding structure. In order for a reactor to be viable, the gain of the plasma, Q, defined as $\frac{P_{\text{out}}}{P_{\text{in}}}$, must be much greater than one. When $Q \rightarrow \infty$, the plasma is ignited, and $P_{\text{in}} \rightarrow 0$. In this state, the fusion power deposited into the plasma is sufficient to balance losses; only the injection of fuel ions to maintain fuel density and the removal of cooled fusion products are required. Note that ignition is not required, nor desirable for a reactor; only high Q. Typically a Q of $\sim$ 30 is needed[5]. Ignition is not necessarily desirable because the power output of a reactor can be more easily controlled with a finite Q plasma. Rearranging equation 1.1 assuming that the bulk plasmas losses are greater than P_{loss}, and using the $\langle \sigma v \rangle$ approximation given above, a reactor relevant rating called the fusion triple product can be calculated. Simply, this is the plasma density, temperature, and confinement time multiplied together. For D-T ignition, in keV-s/m^3:

$$n_i \tau_E T \sim 5 \times 10^{21} \tag{1.2}$$

At the energies required for significant fuel ions to overcome their mutual Columbic repulsion and fuse, the containment of the plasma can not depend on regular material walls. Thus, one option for achieving the requirements outlined in equations 1.1 and 1.2 has been to take advantage of a plasma's inherent ability to respond to electromagnetic fields, and confine the plasma using magnetic fields. On a particle level, ions and electrons in the plasma gyrate around field lines and are confined because of the Lorentz force. This is known as magnetic confinement. To satisfy equation 1.2 using magnetic confinement, densities around $\sim 10^{20}$/m^3, temperatures of $\sim$ 10 keV, and a confinement time on the order of $\sim$ 1 s are needed. Another approach is inertial confinement[6], where plasma confinement is provided by the inertia of the system and hence very short. This approach requires lasers or other drivers to compress a small sphere of fuel to ultra high densities to make up for the short confinement time and essentially creates a small thermonuclear explosion.

ITER is based on a magnetic confinement concept called the tokamak. A schematic of a tokamak and its main features are shown on Figure 1-3. To date, the tokamak is the most successful concept for confining plasmas in a controlled manner at the keV energies necessary for thermonuclear fusion to occur. Figure 1-4 illustrates the fusion triple product progress in reaching the reactor regime by tokamaks. The tokamak is a doughnut shaped device with a dominant Tesla-size magnetic field going toroidally

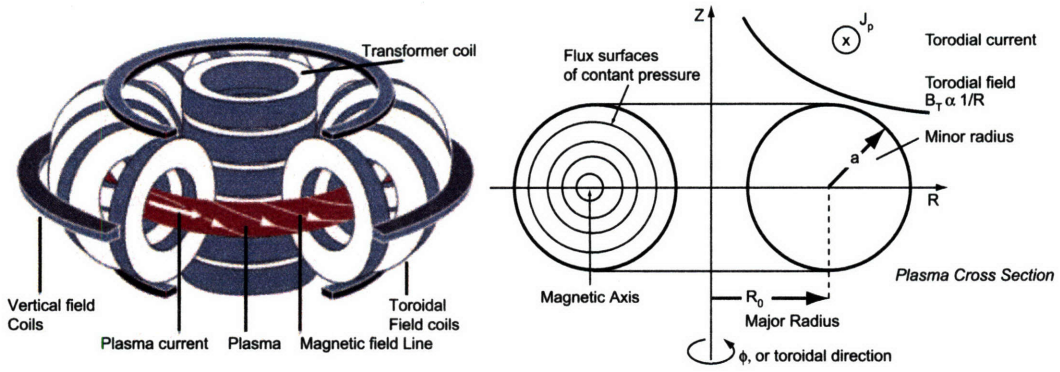

Figure 1-3: Tokamak overview. (Left graphic from Nuclear Fusion[7])

around the machine, and a weaker poloidal magnetic field sustained by a toroidal current in the plasma. These are denoted by B_T, B_p, and J_p respectively. Typically, the poloidal field is approximately an order of magnitude smaller than the toroidal field. An additional vertical field which results in an inward J_p x B_v force keeps the plasma from moving outward from the hoop force. Specifically, the dominant toroidal field provides stability, while the poloidal field gives equilibrium. Thus, the plasma pressure is roughly an order of magnitude lower than the total magnetic pressure, and the vacuum fields are not normally altered significantly by the plasma's diamagnetism.

The toroidal field in a tokamak is created by coils surrounding the torus and results in a vacuum field $B_T \propto 1/R$. The plasma current is induced either by transformer action, with the primary consisting of a solenoid going through the center of the torus and the plasma serving as the secondary, or via RF waves that interact with the plasma and accelerate electrons in a preferred direction. Overall, the toroidal and poloidal fields result in a helical magnetic field line structure around the torus. Without collisions, electrons and ions in theory would then gyrate endlessly around the torus, nearly following these field lines. In reality collisions and instabilities occur and result in the heat losses modeled in equation 1.1. Additionally, these helical fields, as they travel around the torus, form nested flux surfaces with constant plasma pressure.

Despite the excellent progress made by tokamaks, the detailed physics of magnetic confinement is far from resolved. Key issues such as transport, heating, and current drive are active areas of research. For example, the confinement time used in equation 1.1 for the design of ITER is based on an extrapolation of an empirical fit of all confinement time data available currently. Neoclassical theory predictions, based on classical plasma orbit collisions modified for tokamak geometry, are available but

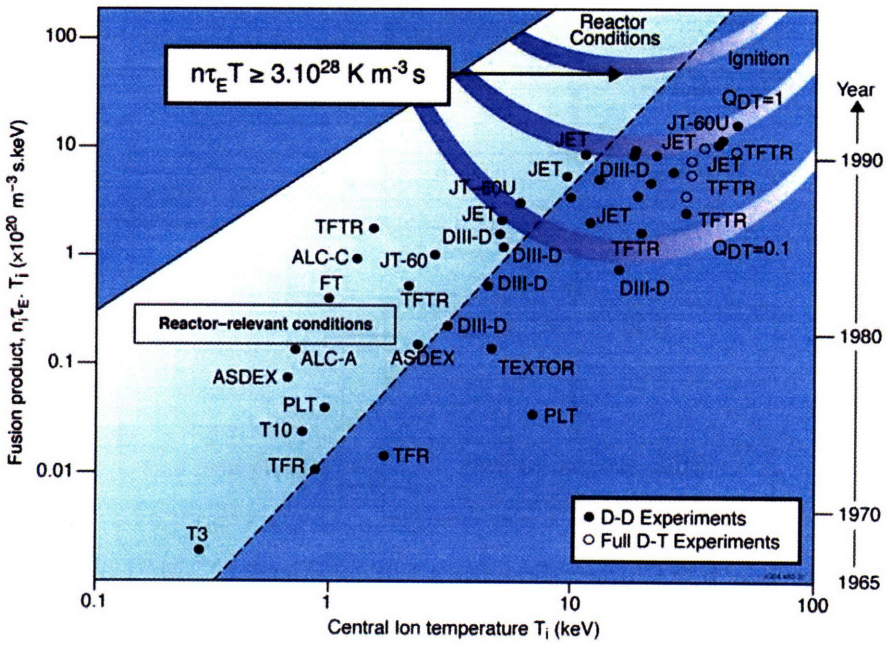

Figure 1-4: Compilation of tokamak $n\tau_E T$ results. The next generation tokamak experiment, ITER, is expected to reach Q=10. (From the JET site[8])

predict a confinement time normally higher than observed in experiment. Thus, important experiments and studies are ongoing at current fusion devices to prepare for both ITER operation and to understand further the physics of magnetic confinement.

1.2 Plasma Heating and Thesis Research

An interesting area of active research mentioned above is the use of RF waves to heat the plasma. In order to reach the hot temperatures required from equation 1.1, the plasmas in tokamaks are heated by various methods. The initial and primary manner is Ohmic heating, which is simply heating caused by the toroidal current and finite resistivity in the plasma. However, since the resistivity of the plasma scales as $T_e^{-\frac{3}{2}}$, ohmic heating must usually be supplemented by other forms of heating to reach large gain or ignition conditions. There are two auxiliary heating methods, the first via the injection of energetic neutrals which can penetrate the plasma and eventually give up their power to it through collisions. The second is via the injection of large amounts of power via electromagnetic waves using antennas. Various heating schemes involving waves are used. A scenario known as ICRF minority heating is very effective at coupling large amounts of power into the bulk plasma. Here, a minority

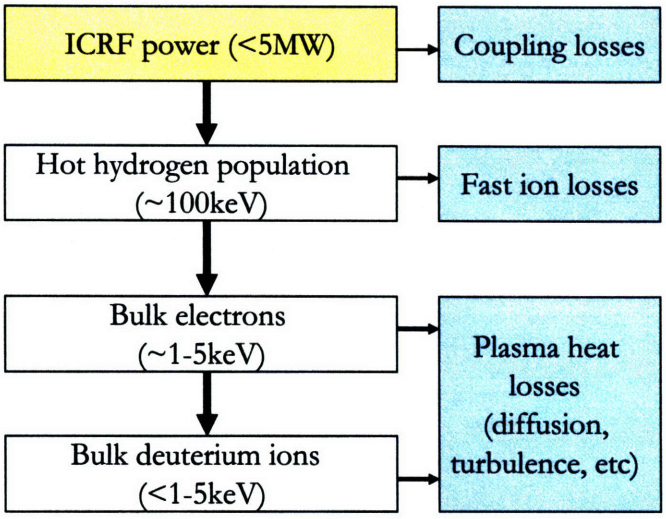

Figure 1-5: ICRF power flow for a typical Alcator C-Mod plasma.

species refers to a population that is $\sim<$ 10% of the bulk plasma. A plasma might consists of $\sim$ 95% deuterium, and $\sim$ 5% hydrogen for minority heating, for example. This scheme deposits the RF power into this minority population in the core of the plasma, and tends to create a minority distribution that is much more energetic than the bulk plasma. These accelerated minority ions are also typically anisotropic in phase space. This hot minority population slows down on the bulk plasma through collisions and serves as the RF power conduit for heating the rest of the plasma. The use of ICRF minority heating in present experiments allows current plasmas to reach high performance regimes, simulate the existence of a supra-thermal particle population similar to MeV level fusion products in full scale fusion reactors, and to study and understand the physics required for heating and maintaining reactor-size high Q plasmas. A simple power flow chart illustrating the ICRF minority heating scheme for Alcator C-Mod is shown in Figure 1-5.

This thesis aims to characterize and study the physics of the minority heating scheme via the diagnosis of this energetic particle distribution sustained in the plasma by ICRF heating. Previous work to characterize this mechanism on Alcator C-Mod involved studying bulk plasma parameters, such as stored energy, electron temperature, and neutron rates during RF injection[9]. These studies verified the general effectiveness of ICRF minority heating and the existence of an energetic minority population. However, none entailed the experimental diagnosis of the core minority population itself. Accurate diagnosis of this population is important for detailed understanding of the ICRF and energetic particle physics involved in Alcator C-Mod's unique op-

erating regime, and for comparisons with theory. Other tokamaks[10, 11, 12] have diagnosed these energetic populations directly but they do not operate with Alcator C-Mod's high densities or magnetic fields.

In general, the diagnosis of these minority energetic distributions in fusion plasmas is not trivial. Currently, there are three different approaches to making this measurement. The first two diagnostic methods rely on the the principle of charge-exchange (CX), where the minority hydrogen ion becomes neutral by taking an electron from a neutral or not fully ionized donor:

$$H^+ + A^{+b} \rightarrow H^0 + A^{+(b+1)} \tag{1.3}$$

In theory, the velocity of either participant is not affected by this reaction. The first approach using charge-exchange involves H_α spectroscopy; it typically measures Doppler shifts and broadening of the Lyman-alpha line of charge-exchanged energetic minority ions in order to infer an effective temperature of the minority species[13]. Usually a neutral beam is required to provide a significant source of neutrals to overcome the large plasma light background. The use of a neutral beam to provide electron donors is typically referred to as active CX. Passive CX refers to using only the plasma's background electron donors. The second minority ion diagnostic technique, used for this thesis research, directly measures the energetic neutral particles created through charge-exchange that escape from the plasma[14]. Both passive and active CX signals can be considered. This method typically requires bulky neutral particle analyzers and also requires several data extractions steps. The third, the least employed, is the detection of gamma rays from nuclear reactions between the fast distribution and bulk ions. The challenge with this method is the typically very large equipment, in terms of shielding, that is necessary. The absolute signal level can also be an issue[15].

The basis of this thesis involves both the design, construction, and implementation of a compact neutral particle analyzer (CNPA) array and the use of coupled Full-wave/Fokker-Planck(FW/FP) codes such as the AORSA/CQL3D[16, 17] or TORIC/FPPRF[18, 12] packages to study the temperature and RF power deposition of Alcator C-Mod's fast minority hydrogen ions in the 50-350keV range. FPPRF and CQL3D are Fokker-Planck solvers which are coupled to wave propagation codes and can simulate the minority distribution with full tokamak geometry considerations.

In terms of new results, the work in this thesis contributes to three areas: NPA development, experimental measurements of ICRF minority tails, and comparison of

these results with numerical simulations. Specifically in the first area, the CNPA involves several NPA innovations, most notable of which are fast digitization techniques to replace traditional real-time analysis systems. Experimentally, first time measurements of the core Alcator C-Mod minority proton distribution are presented and analyzed first using a relatively simple model. Temperatures of up to ~120 keV are measured. The model found that the minority proton temperatures are fitted well by a theoretical scaling calculated by Stix[19], and that these temperatures are peaked off-axis, even for an on-axis resonance chord. Comparisons with the FW/FP solvers are adequate and provide a potential explanation for the off-axis peaking result. In particular the comparison with the new AORSA/CQL3D code is good. Preliminary results with a full synthetic diagnostic based on the AORSA/CQL3D code also shows reasonable agreement. These analyses with the FW/FP solvers represent the first comparison between predictions of such detailed codes and experiment.

Before going into a detailed outline of the thesis, a brief introduction to the Alcator C-Mod tokamak, where the experimental work for this thesis was performed, is given below.

1.3 The Alcator C-Mod Tokamak

Presently, Alcator C-Mod is *the* high field diverted tokamak experiment in the world. It is a high field, high density, compact device. The primary auxiliary heating system is ICRF minority heating at 5.4 T for D(H), and 8 T for D(He^3). Thus, H and He^3 minority tails are routinely created in C-Mod plasmas except at the highest densities, where the collisionality of the plasma is very high. Figure 1-6 is a schematic of Alcator C-Mod and Table 1.1 lists it operating parameters. A new diagnostic neutral beam (DNB)[20], capable of producing up to 7 A of 50 keV hydrogen neutrals for 1.5 s, can be injected radially into the machine and permits active CX experiments. The FWHM of the beam is typically ~12 cm.

Currently, there are 3 sets of ICRF antennas in C-Mod. Two dipole antennas are located at D and E Port, each delivering up to 1.5 MW of power at 80 MHz. A 4-strap antenna with power up to 3 MW is stationed at J, typically operated at 78 MHz, with a tuneable range of 50-80 MHz. J antenna can also be run at different phasing, resulting in different $k_{\|}$. So far, these antennas have coupled up to 5-6 MW of power into Alcator C-Mod plasmas[2]; however, as shown later, when operating at the lower density range of Alcator C-Mod (lined-integrated densities of less than ~$10^{20}/m^3$), it only takes ~1 MW for significant ICRF tails to form. It is these lower densities

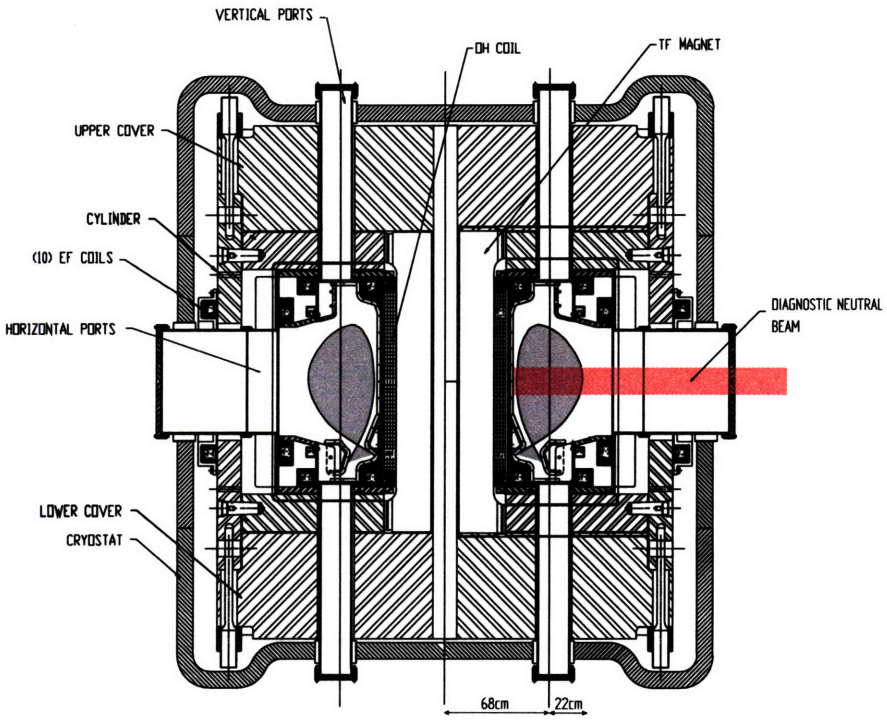

Figure 1-6: The Alcator C-Mod tokamak.

plasmas with moderate RF power that allow the use of neutral particle analyzers to diagnose the energetic minority tail. These plasmas form the basis of this thesis.

A brief description of some of the plasma diagnostics is now given. The emphasis is on measurements that are used or referred to extensively for this thesis. A complete overview of the ~25 diagnostic systems on Alcator C-Mod is available from Basse[21].

Density and Z_{eff}: the plasma electron density is primarily measured via three systems, the Thomson scattering system with core and edge channels, the visible bremsstrahlung diagnostic, and a two-color interferometer system. All three systems can provide spatial profiles at different time resolutions. Z_{eff} spatial profiles as a function of time are available by comparing the results between these diagnostics.

Temperature: the plasma electron temperature is measured by up to four different systems, depending on electron cyclotron emission cut-offs. These include the Thomson scattering system, and three different electron cyclotron emission diagnostics. The bulk ion temperature is estimated from neutron counters.

For analysis that require detailed spatial density, temperature, and Z_{eff} profiles, the results from the above systems are combined to give spatial profiles with time resolution of up to 60 Hz. Examples of these profiles used for this thesis are shown

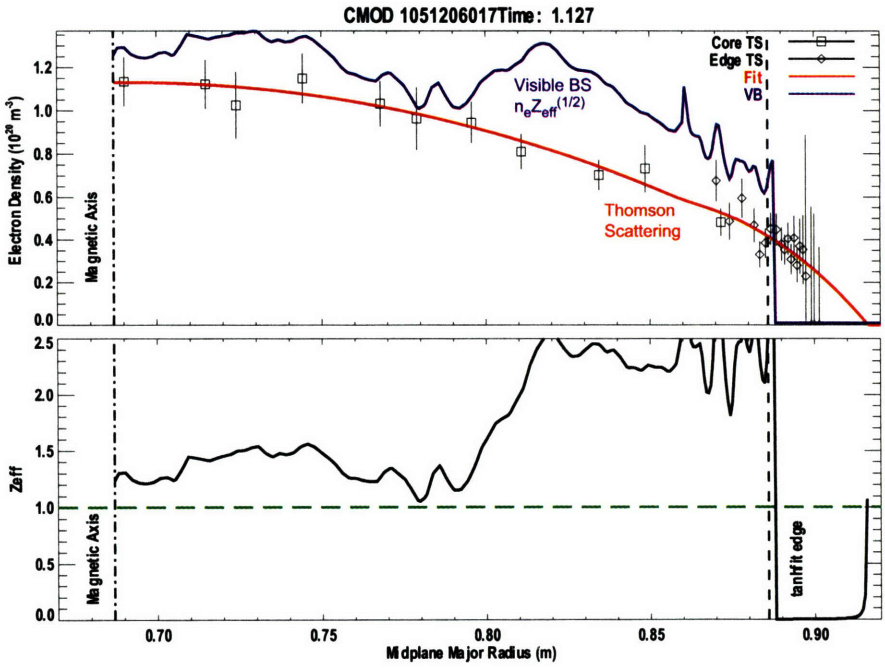

Figure 1-7: Density and Z_{eff} profiles from the Thomson scattering diagnostic and visible bremsstrahlung measurements. The calculated Z_{eff} is estimated to have errors up to 30%

Table 1.1: Alcator C-Mod machine parameters (modified from J.Liptac)

Parameter	Symbol	Range or Value
Toroidal Field	B_0	3.0-8.0 T
Plasma Current	I_p	0.4-2.0 MA
Major Radius	R_0	68 cm
Minor Radius	a	22 cm
Elongation	κ	0.9-1.8
Triangularity	δ	0.1-0.85
Plasma Volume		~ 1 m^3
ICRF Source Power		8 MW
LH Source Power		3-4 MW
Central Density	n_{e0}	5×10^{19}-2×10^{21} m^{-3}
Central Temperature	T_{e0}	0.5-5.0 keV
Max pulse length		5 s

in Figure 1-7, based on an IDL program by K. Zhurovich.

Impurity measurements: Alcator C-Mod has a large and flexible array of visible light charge-exchange recombination spectroscopy channels. They are dominantly concerned with edge phenomena, but several core channels can measure core boron impurity densities using the DNB during low density Alcator C-Mod shots. Measurements from these core channels play a role in interpreting the CNPA data set.

Edge gas pressure: several gauges with the ability to measure diagnostic port neutral gas pressures in the ~0.1 mtorr range with time resolutions better than 1 ms are available.

Magnetics: a large set of standard magnetic equilibrium diagnostics consisting of B_θ coils, flux loops, B_ϕ coils, and Rogowski coils are installed in Alcator C-Mod. Primarily, these measurements are used for reconstruction of the MHD equilibrium using the EFIT code and real-time control.

Soft x-rays: four soft x-ray (~2-10 keV) diode arrays consisting of a total of 152 channels provide extensive coverage of the plasma. Each diode provides a line averaged measurement of the soft x-ray emissivity.

H/D ratio: the hydrogen to deuterium ratio of a discharge is estimated by measuring the relative H and D Balmer line intensities from recycling edge neutrals. The H/D meter is a dedicated photodiode array used for this purpose.

1.4 Thesis Outline and Overview

The rest of the thesis is outlined as follows:

The physics behind ICRF heating and its applicability to C-Mod is quickly reviewed in Chapter 2. In addition, the FW/FP packages used in this thesis are discussed.

In Chapter 3 the diagnostic principles behind energetic neutral particle analysis and the CNPA diagnostic are examined.

Active and passive CNPA measurements from the 2005 Alcator C-mod campaign are presented in Chapter 4. A relatively simple model for interpreting CNPA data is given which includes the effects of impurity CX, beam profiles, and beam halo neutrals. This simple model permits approximate measurements of the minority proton temperature and its location, along with the RF power absorption.

Results from the model presented in Chapter 4 indicate phase space anisotropy of the fast proton distribution, minority proton temperatures that scale with the Stix parameter, and off-axis peaking of these protons. Comparisons of the flux surface averaged minority temperature with results from the FW/FP solvers are reasonable and provide a potential explanation for the observed peaking of the minority tail off-axis. In particular the comparison with the new AORSA/CQL3D code is good, while the TORIC5/FPPRF match is found to be relatively poor. An explanation is provided and discussed.

A general synthetic NPA diagnostic created for this thesis is reviewed in Chapter 5. The coupling of the synthetic diagnostic with the CQL3D code is discussed in the context of inferring spatial RF power deposition, minority distribution, and profiles from CNPA measurements. First results are shown and reasonable agreement is again found between the experiment and the AORSA/CQL3D simulations.

The thesis concludes with a short summary and suggestions for future work in Chapter 6. Possible future ICRF experiments involving the CNPA are discussed, and reasonable upgrades for the diagnostic are proposed.

Chapter 2

ICRF Minority Heating

2.1 Introduction

Alcator C-Mod relies on ICRF minority heating[19] as its main auxiliary plasma heating method. ICRF minority heating is a subset of RF heating methods that uses waves with frequencies comparable to the ion cyclotron frequency.

In order to heat a plasma to thermonuclear conditions using RF waves, the wave chosen out of the large number of possible waves must meet several requirements; the first is that the launched wave must be able to propagate to the region of desired absorption, typically the center of the plasma. Second, the wave must have a strong tendency to damp on the ions or electrons at that desired location. Collision-less deposition relies on either Landau damping for heating in $v_{\|}$, or first to higher cyclotron cyclotron absorption heating for heating in $v_{\perp}$. Specifically, harmonic heating refers to matching a wave's perpendicular electric field polarization to the gyro-motion of either the ions or electrons; thus, at the right frequency the ion or electron essentially feels a constant or stationary electric field which provides it with a constant acceleration. From an engineering point of view, sources must be available at the desired wave frequency and the launcher structure should not be too complicated. Realistically, the launcher should also be located on the low field side, or outboard side, of the tokamak where space is available. It is seen in this chapter that ICRF minority heating, used on Alcator C-Mod and other tokamaks, satisfies all of these conditions and therefore is one of the primarily schemes for heating fusion plasmas.

Specifically, ICRF minority heating relies on the compressional Alfvén, magnetosonic, or fast wave. This wave is launched at a frequency that propagates easily through the bulk plasma, but is damped strongly on a minority resonance via a first harmonic cyclotron interaction. Typically in Alcator C-Mod, this would be a bulk

deuterium plasma with a minority hydrogen fraction of ~5%. Thus, because the power is deposited mostly into this minority species, an energetic minority distribution, or tail, is created. This tail then slows down primarily on the bulk electrons and transfers the wave power to the bulk plasma, as charted in Figure 1-5. These bulk deuterium plasmas with small amounts of hydrogen are commonly labeled D(H).

This chapter serves as a brief review of the physics behind ICRF minority heating, and is broken into several sections. The first section reviews the cold plasma dispersion relationship and the associated electric field polarization of the waves described by it. Using these two relationships, the two waves that exist in the ion cyclotron regime, the fast and slow Alfvén waves, are identified and characterized in terms of propagation and electric field polarization. It is seen that for a plasma with only one ion species, neither wave satisfies both the propagation and damping criteria discussed above for first harmonic fundamental heating. However, when a minority species is added, both criteria are met when the fast wave is used to heat the minority species. A typical Alcator C-Mod D(H) discharge is used to illustrate the wave physics behind this heating scenario. With the heating scheme established, the last two sections briefly review the expected behavior of the minority species when accelerated by this non-isotropic RF drive in terms of the Fokker-Planck equation, and discuss the codes which can simulate this heating scheme in detail.

Several reviews are available for a more comprehensive look at these topics.[22, 3, 23, 24, 25].

This chapter thus establishes the physics and features of the distribution function that the CNPA measures.

2.2 Waves in the Ion Cyclotron Regime and the Cold Plasma Model

The relevant plasma waves in the ion cyclotron frequency regime used for ion heating in fusion plasmas can be easily derived by considering the wave dispersion tensor for a homogenous cold plasma in an uniform magnetic field[22]. This dispersion tensor stems from linearizing and coupling the ion and electron equations of motion along with Maxwell's equations. Here, the polarization notation used in Wesson's Tokamaks[3] is followed. Assuming a magnetic field aligned with the z-axis and $k_y = 0$, $\omega(\mathbf{k})$ and the polarization of each allowed mode can be determined using the following:

$$\begin{pmatrix} \epsilon_\perp - n_\parallel^2 & \epsilon_{xy} & n_\perp n_\parallel \\ -\epsilon_{xy} & \epsilon_\perp - n^2 & 0 \\ n_\parallel n_\perp & 0 & \epsilon_\parallel - n_\perp^2 \end{pmatrix} \cdot \begin{pmatrix} E_x \\ E_y \\ E_z \end{pmatrix} = 0 \tag{2.1}$$

with

$$\begin{aligned} \epsilon_\perp &= 1 - \sum_j \frac{\omega_{p,j}^2}{\omega^2 - \omega_{c,j}^2} \\ \epsilon_{xy} &= -i \sum_j \frac{\omega_{c,j}\omega_{p,j}^2}{\omega(\omega^2 - \omega_{c,j}^2)} \\ \epsilon_\parallel &= 1 - \sum_j \frac{\omega_{p,j}^2}{\omega^2} \\ \vec{n} &= \frac{\vec{k}c}{\omega} \end{aligned}$$

where ω_c is the cyclotron frequency and ω_p the plasma frequency. The sums are taken over each plasma species j, and the sign of the charge is included in the cyclotron frequency. $\vec{n}$ is the index of refraction. $n_\parallel$ is determined by the antenna via[25]:

$$k_\parallel = \frac{\vec{k} \cdot \vec{B}}{B} = \frac{1}{R}\left(N_\phi - \frac{m}{q}\right) = \frac{N_\phi}{R} - \frac{mB_\theta}{rB_z} \tag{2.2}$$

where q is the safety factor, N_ϕ the conserved toroidal mode number, m is the poloidal mode number, typically much less than N_ϕ. For the plasmas in this thesis, the ICRF power is delivered through either the D or E port dipole antennas. These dipoles operate with a $0{:}\pi$ phasing which results in a dominant vacuum N_ϕ of ± 10. $k_\parallel$ is then approximately equal to $\frac{10}{R}$, since the m/q term is small.

Before going further the electric field polarization must be defined. The co-ion ($E_x + iE_y = E_+$) to counter-ion ($E_x - iE_y = E_-$) rotation of the electric field can be determined from equation 2.1, giving:

$$\left|\frac{E_+}{E_-}\right| = \left|\frac{i\epsilon_{xy} + (\epsilon_\perp - n^2)}{i\epsilon_{xy} - (\epsilon_\perp - n^2)}\right| \tag{2.3}$$

This ratio indicates how much of the electric field is rotating in the same sense as the ions. Instinctively, a larger ratio would result in greater heating at the resonant cyclotron frequency.

Returning to the dispersion tensor, taking the determinant of the 3x3 matrix in

equation 2.1 gives[3]:

$$\epsilon_\perp n_\perp^4 - [(\epsilon_\perp - n^2)(\epsilon_\perp + \epsilon_\parallel) + \epsilon_{xy}^2]n_\perp^2 + \epsilon_\parallel[(\epsilon_\perp - n^2)^2 + \epsilon_{xy}^2] = 0 \tag{2.4}$$

For frequencies in the ICRF heating regime (~10-100Mhz) with $n_\perp \gg n_\parallel$, equation 2.4 produces two solutions. They are termed the 'slow' and 'fast' waves. In both of these cases, $\epsilon_\parallel$ is negative and much larger than $\epsilon_\perp$ and ϵ_{xy}. The slow wave can be derived by considering large n^2 (hence 'slow') and balancing the first two terms:

$$n_\perp^2 \approx \frac{\epsilon_\parallel(\epsilon_\perp - n_\parallel^2)}{\epsilon_\perp} \tag{2.5}$$

Due to the large and negative $\epsilon_\parallel$, $n_\perp^2$ is positive only for $0 < \epsilon_\perp < n_\parallel^2$, and therefore throughout most of the plasma the slow wave can not propagate. It therefore can not be used for ICRF heating with a perpendicular launch.

The fast wave, however, bears more fruit. It can be derived by considering the last two terms in equation 2.4 and again taking $\epsilon_\parallel$ to be large:

$$n_\perp^2 \approx \frac{\epsilon_{xy}^2 + (\epsilon_\perp - n_\parallel^2)^2}{(\epsilon_\perp - n_\parallel^2)} \tag{2.6}$$

The dispersion relationship contains two cut-offs and one resonance. The cut-offs are given by the zeros of the numerator, while the resonance is determined by the zero of the denominator. One of the cut-offs is associated with the finite $k_\parallel$ of the spectrum and results in a thin evanescent layer at the edge that the ICRF power must tunnel through. As it turns out, a finite $k_\parallel$ also results in Doppler broadening of the cyclotron resonance and is needed for effective heating. Hence this thin cut-off layer (~1 cm) is always present. For a purely deuterium plasma, the cut-off condition is $w_{p,d}^2 > 0.75c^2k_\parallel^2$ [3]. With a finite $k_\parallel$, the cyclotron resonance is shifted to $\omega = \omega_c + k_\parallel v_{\parallel,m}$, where $v_{\parallel,m}$ is the minority ion velocity parallel to the magnetic field. The other cut-off and its associated resonance is the ion-ion hybrid pair. This resonance and cut-off pair always occurs for finite minority density in the cold plasma model. With finite temperature, the pair only occur when a critical minority fraction, $f_c = n_m/n_b$ is reached. This critical value can be estimated when kinetic effects are included[3]:

$$f_c = \frac{2k_\parallel v_{\parallel,m}}{\omega}\frac{A_b}{A_m}\left[\frac{\alpha^2}{1-\alpha^2} + \frac{k_\parallel^2 c_A^2}{\omega^2}\right] \tag{2.7}$$

where the subscripts m and b indicate the minority and bulk species respectively.

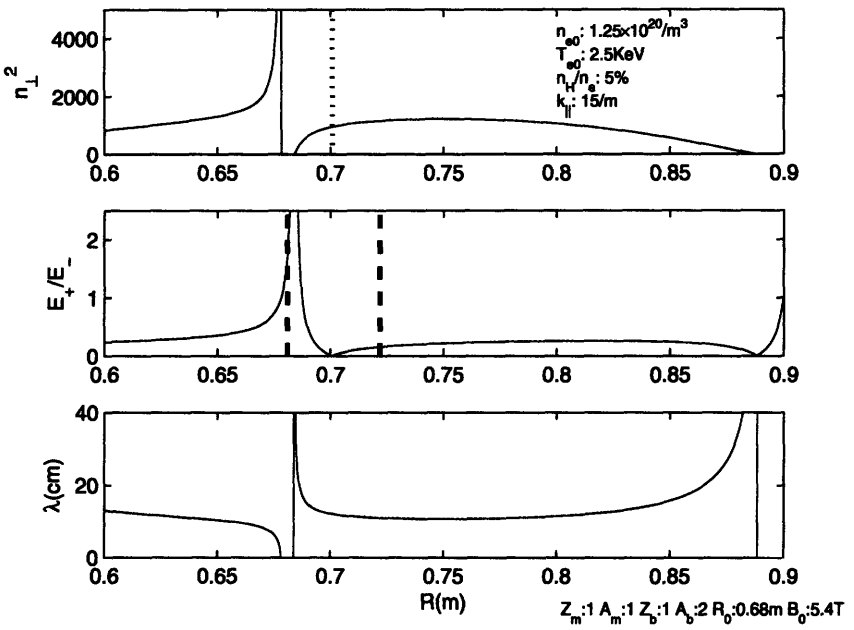

Figure 2-1: Fast wave $n_\perp^2$, E_+/E_-, and wavelength as a function of major radius for a low density, 5.4 T, 6% H minority Alcator C-Mod plasma using the cold plasma and WKBJ approximations. Parabolic density and temperature profiles are used, with the peak values indicated on the top plot. A constant $k_\parallel$ of 15/m is used. The dashed line on the top plot marks the major radius of the minority cyclotron resonance layer. In the middle plot, the region in between the dashed lines marks the Doppler broadened cyclotron resonance for a minority distribution with a parallel temperature of ~5 keV.

$v_{\parallel,m}$ here is an estimate of the averaged minority ion parallel velocity, c_A the Alfvén velocity of the bulk ions, A the atomic mass number, and $\alpha = Z_b A_m / Z_m A_b$. Almost all of the D(H) plasmas in this thesis are around or above this threshold.

It should be emphasized that this ion-ion hybrid resonance is not where minority heating occurs but where mode conversion heating can take place.

With the wave dispersion and polarization defined, different heating scenarios can now be examined. The minority heating scheme is motivated by the fact that the polarization of the fast wave is basically all in the counter-ion direction near the cyclotron resonance for the bulk species. This can be seen by solving equation 2.3 for a single ion species plasma with the fast wave $n_\perp$ and neglecting the small $n_\parallel$, giving:

$$\left|\frac{E_+}{E_-}\right| \approx \left|\frac{\omega - \omega_{c,b}}{\omega + \omega_{c,b}}\right| \tag{2.8}$$

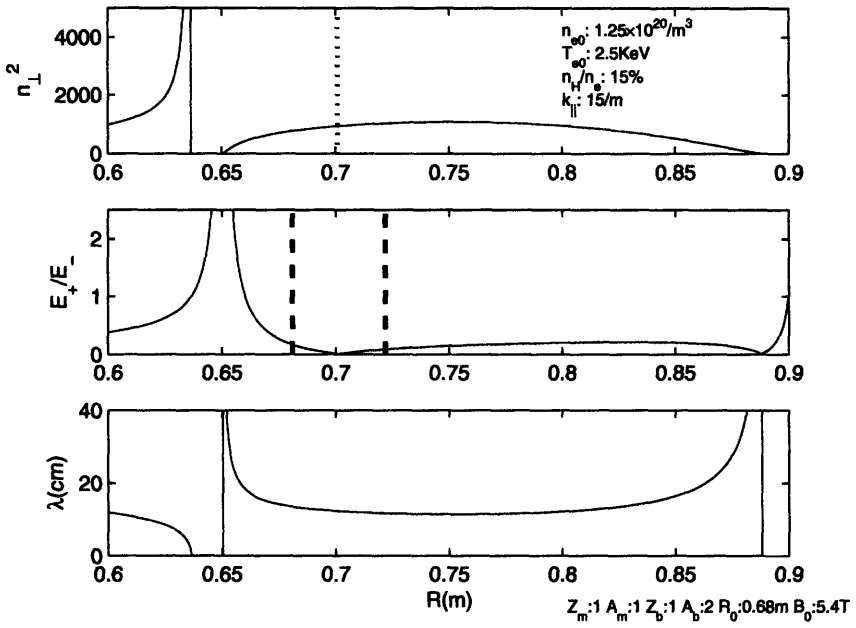

Figure 2-2: Fast wave $n_\perp^2$, E_+/E_-, and wavelength as a function of major radius for a low density, 5.4 T, 15% H minority Alcator C-Mod plasma using the cold plasma and WKBJ approximations. Parabolic density and temperature profiles are used, with the peak values indicated on the top plot. A constant $k_\parallel$ of 15/m is used. The dashed line on the top plot marks the major radius of the minority cyclotron resonance layer. In the middle plot, the region in between the dashed lines marks the Doppler broadened cyclotron resonance for a minority distribution with a parallel temperature of ~5 keV.

Clearly, at $\omega \sim \omega_{c,b}$, the desired polarization is zero. The problem can be solved if a minority species is added and used for heating, since now ω is shifted to the minority species. Because the polarization is still mainly determined by the bulk plasma species, it can be estimated by simply inserting the new minority cyclotron resonance frequency in equation 2.8. For a D(H) plasma, $\omega = 2\omega_{c,d}$, resulting in $E_+/E_- \sim 1/3$. As it turns out, this simple explanation is inadequate as the polarization even for the minority case is zero at the exact minority cyclotron resonance layer in the cold plasma approximation. The heating actually comes from the significant E_+ polarization around the exact minority cyclotron resonance when the minority density is low. Hence, some Doppler broadening is required. Figures 2-1 and 2-2 plot $n_\perp^2$, electric field polarization, and wavelength as a function of major radius using the WKBJ and cold plasma approximations for two different plasmas. The first figure shows a low minority fraction plasma which results in an ion-ion hybrid resonance close to the cyclotron resonance. The hybrid cut-off before that resonance has a very high E_+/E_- which efficiently heats Doppler shifted minority protons. The second figure shows a plasma with a high minority fraction which results in the ion-ion hybrid resonance and the associated cut-off being further inboard. The high polarization region is now further away from the cyclotron resonance and hence the heating is less efficient.

At a high enough minority density, most of the power makes it past the effective minority damping area. Some of this power tunnels through the ion-ion hybrid cut-off to mode convert into different waves at the ion-ion hybrid resonance layer that can heat either ions or electrons. During a single pass, the maximum amount of power incident on the cut-off that can be mode converted is 25%[3]. The rest is reflected at the cut-off back toward the low field side edge cut-off. Finally, these fast wave packets can again be reflected toward the high field side from either the edge cut-off or the vacuum vessel itself and can then reach the ion-ion hybrid resonance again. Hence, multiple passes of the wave must occur for effective mode conversion heating when the wave is launched from the low field side. In other words, the minority damping must be very weak for mode conversion heating to be dominant, since the wave effectively requires multiple passes through the minority cyclotron resonance layer before significant mode conversion can occur.

It should be noted that the WKBJ approximation used in the above examples is not really valid for low density ($n_{e0} \sim 10^{20}$) Alcator C-Mod plasmas, since the wavelengths are comparable to the size of the plasma. In the real experiment, this tends to produce poor ICRF wave focusing which results in significant wave power along the entire resonance layer ($R \sim 69$ cm, $Z \sim -20$ to 20 cm). Nevertheless,

the above cases are good qualitative examples of how the minority heating scheme works, and what happens when at high minority fraction that regime is no longer valid. Lastly, the inclusion of finite temperature effects in the dispersion relationship will also alter this picture quantitatively but not qualitatively.

For the plasmas in this thesis, n_H/n_e is typically $\sim$ 6% and the cyclotron resonance is typically at R=69 cm. Thus, the region of high E_+/E_- is encompassed by the Doppler shift of the minority ions even at thermal energies and hence mode conversion is expected to be small for these discharges. Mathematically, the fraction of input power damped on the minority species during a single-pass can be estimated from[24]:

$$P_{abs} = 1 - e^{-2\eta} \tag{2.9}$$

$$2\eta \approx \frac{\pi}{2}\frac{\omega_{p,b}}{c}\frac{n_m}{n_b}\frac{Z_m}{Z_b}R_0\left(\frac{\omega/\omega_{c,b}-1}{1+\sigma_l^2}\right) \tag{2.10}$$

$$\sigma_l^2 = \frac{\pi}{4}\left(\frac{n_m}{n_b}\frac{A_b}{A_m}\frac{Z_m^2}{Z_b^2}\right)^2\left(1-\frac{\omega_{c,b}^2}{\omega^2}\right)^2\left(\frac{\omega}{k_\parallel v_{\parallel,m}}\right)^2 \tag{2.11}$$

where again the subscripts b indicate the bulk or majority species, while m is for the minority species. n_m is the minority density, A_b the minority atomic number, Z_m the charge of the minority ion, c is the speed of light, R_0 the magnetic axis, and $v_{\parallel,m}$ is an estimate of the minority parallel velocity. All of these quantities are evaluated at the resonance. The low D(H) density plasmas in this thesis typically have $\omega_{p,d} \sim 10^{10}/s$ and minority parallel temperatures of $\sim$ 25 keV, giving $2\eta \sim 1$. This results in P_{abs} $\sim$60% for single-pass absorption. As it turns out, detailed simulations discussed later show $\sim$90% of the injected power being absorbed by the minority protons for the type of plasmas studied in this thesis. The experimental data available from the CNPA for these plasmas also concur with the conclusion that minority heating is the dominant absorption mechanism.

2.3 The Minority Distribution

With the minority heating scheme defined in the last section, the details of the minority species under this RF drive can now be described. The situation is complicated as the distribution can become non-Maxwellian and anisotropic. Here, the main physics are highlighted with particular emphasis on subjects that are needed for the later chapters. This review principally draws on Hammett's authoritative discussion of the topic[12].

Before going into the equations that describe minority heating, a qualitative pic-

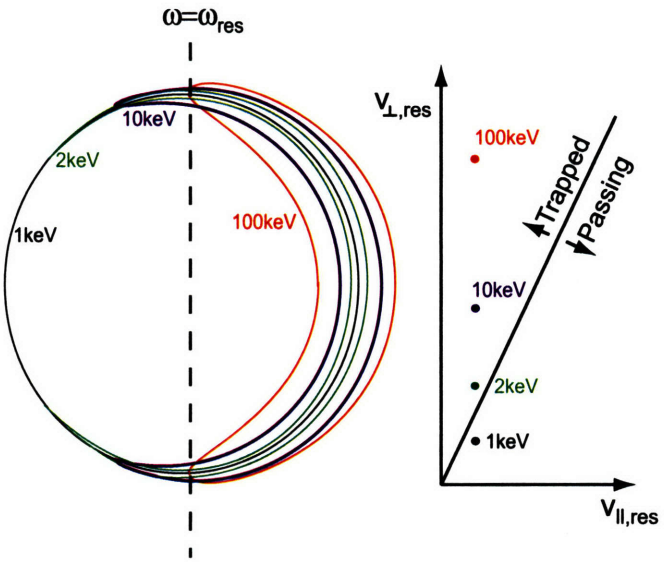

Figure 2-3: Minority ion orbits during successive passes through the heating resonance. For $k_{\|} \sim 0$, the particle is heated in $v_{\perp}$ only. Without collisions, the particle's banana tips eventually end up at the resonance layer. The plot on the right qualitatively illustrates the climb in $v_{\perp}$ and total energy during each pass. The velocities on the graph are evaluated at the major radius of the resonance. (Modified from Figure 1.7 of Hammett's thesis[12])

ture of the physics is given. Simply, when the resonance layer is tuned to a particular major radius of the plasma, minority ions are given a kick in perpendicular phase space every time they pass through that major radius. The key feature of minority ICRF heating in a tokamak is the fact that ICRF power heats the minority ions dominantly in the perpendicular direction. This results in trapping of the minority ions due to the $1/R$ dependence of the tokamak magnetic field and the adiabatic invariant $\mu = mv_\perp^2/2B$. This heating tends to trap the fast ions and drive their banana tips towards the heating resonance layer. Figure 2-3 illustrates this dynamic. Furthermore, the fast ions with banana tips near the resonance are actually preferentially heated because their $v_\parallel$ is small and thus they spend the longest amount of time around the resonance. Hence, if pitch angle scattering is small relative to this RF drive, the minority distribution is anisotropic, with significant density built up around the heating resonance. In fact, these fast ions with their banana tips at the resonance layer make up the hottest part of the minority distribution at a particular flux surface. Figure 2-4 shows such a distribution plotted in mid-plane velocity space for a specific flux surface. The energetic portions of the distribution are bunched up around the heating resonance layer; this feature is colloquially referred to as 'rabbit ears' and technically as resonance localization. As it turns out, for a wave with finite $k_\parallel$, the banana tips of the heated particles with Doppler-shifted resonances on either the inboard or outboard sides of the un-shifted resonance are still pushed towards the $k_\parallel = 0$ resonance layer. This is because the particles also gain a small increase in $v_\parallel$ for each heating pass through the shifted resonance for a wave with finite $k_\parallel$. Skipping ahead, these are the energetic minority ions mainly measured by the CNPA diagnostic described in the next chapter.

Specifically, these anisotropic features occur when the fast minority ions are primarily slowing down on the bulk electrons with small pitch angle scattering. The critical threshold energy between fast ion-ion and fast ion-electron slowing down is typically around ~20 keV for the low density plasmas in this thesis and given by[3]:

$$E_c = 14.8 T_e \left[\frac{A_m^{3/2}}{n_e} \sum_j n_j \frac{Z_j^2}{A_j} \right]^{2/3} \tag{2.12}$$

where the sum is taken over the bulk ions.

Mathematically, the time-evolution of the distribution can be described by the

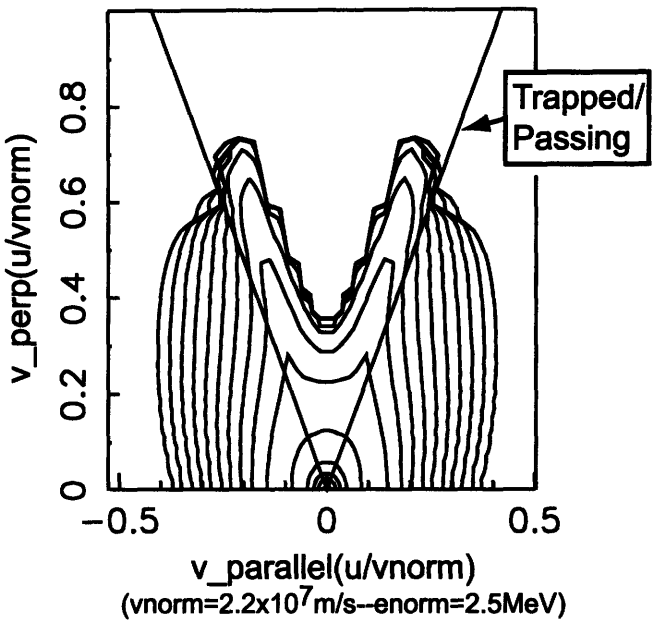

Figure 2-4: Contour plot of minority proton outboard mid-plane velocity at r/a=0.23 for a low density Alcator C-Mod shot from CQL3D simulations.

bounce-averaged Fokker-Planck equation with a quasilinear RF diffusion term:

$$\frac{\partial f}{\partial t} = \langle C(f) \rangle + \langle Q(f) \rangle \tag{2.13}$$

where $\langle C(f) \rangle$ is the bounce-averaged collision operator, and $\langle Q(f) \rangle$ the bounce-averaged quasilinear diffusion operator describing the ICRF forces on the minority distribution. The full 2-D bounce-averaged $\langle Q(f) \rangle$ is quite complicated. A simplified version assuming $k_{\|} = k_{\perp} = E_{-} = E_{\|} = 0$ is given by Hammett[12] which illuminates the physics involved:

$$\langle Q \rangle = \left[\left\{ \frac{H}{\tau_B} \frac{2\pi r B}{B_\theta |v_{\|}|} \right\} \frac{1}{v_\perp} \frac{\partial}{\partial v_\perp} \left(v_\perp^2 \frac{P_{\text{Stix}} R_0}{2mnR_{res}} \frac{1}{v_\perp} \frac{\partial f}{\partial v_\perp} \right) \right]_{res} \tag{2.14}$$

$$P_{\text{Stix}} = \left(n \frac{Zq|E_+|^2}{B} \frac{R}{r|sin\theta|} \right)_{res} \frac{R_{res}}{R_0} \tag{2.15}$$

where the subscript res indicates evaluation at the resonance layer, and the m minority subscript has been dropped for convenience. R_0 is the major radius of the magnetic axis, θ the poloidal angle of the minor radii r at the current flux surface that intersects the resonance layer at R_{res}. The mass of the minority ion is m. τ_B is the bounce time, or the time the fast ion takes to go between each banana tip. For

passing particles τ_B is the time the particle takes for one poloidal orbit. H is the Heaviside step function and is zero for particles that do not see the resonance layer. P_{stix} is Stix's original calculation for the flux surface averaged absorbed power assuming an isotropic minority distriubtion[19]. As Hammett states, 'The factor in braces weights Stix's $\overline{Q}$ by the fraction of time a particle spends in the resonance layer.' In other words, the effect of preferential heating of trapped particles with their banana tips near the resonance is clearly seen in this formulation of the quasilinear diffusion operator; specifically, $\langle Q \rangle$ is inversely proportional to $|v_{\|}|$ at the resonance. This actually results in a weak but integrable singularity at the resonance for particles with very small $v_{\|}$.

The evolution of the minority distribution can thus in turn affect the RF power absorption spatially, as minority ions that are trapped are preferentially heated. Hence, a consistent simulation of the minority heating scheme requires iteration between a wave solver and a Fokker-Planck solver to reach a good steady-state solution. Figure 2-5 illustrates this process schematically. Several codes are available for this calculation and discussed in the next section. Steady-state is expected in the $\sim$100-200 ms time range for the $\sim$100 keV effective minority temperatures reached in the low density Alcator C-Mod plasmas studied in this thesis.

Some analytical steady-state solutions for f are available[19, 23, 27]. The definitive work is Stix's solution for the minority distribution[19]. Stix assumed that the minority distribution is isotropic and derived an analytical solution which balances the collision and quasilinear RF operators. Neoclassical effects are not included. Although as stated earlier the minority distribution is anisotropic, it turns out the Stix distribution describes the energy dependence of the minority ions at a constant pitch angle adequately. This distribution is used later for fitting the CNPA data. The Stix

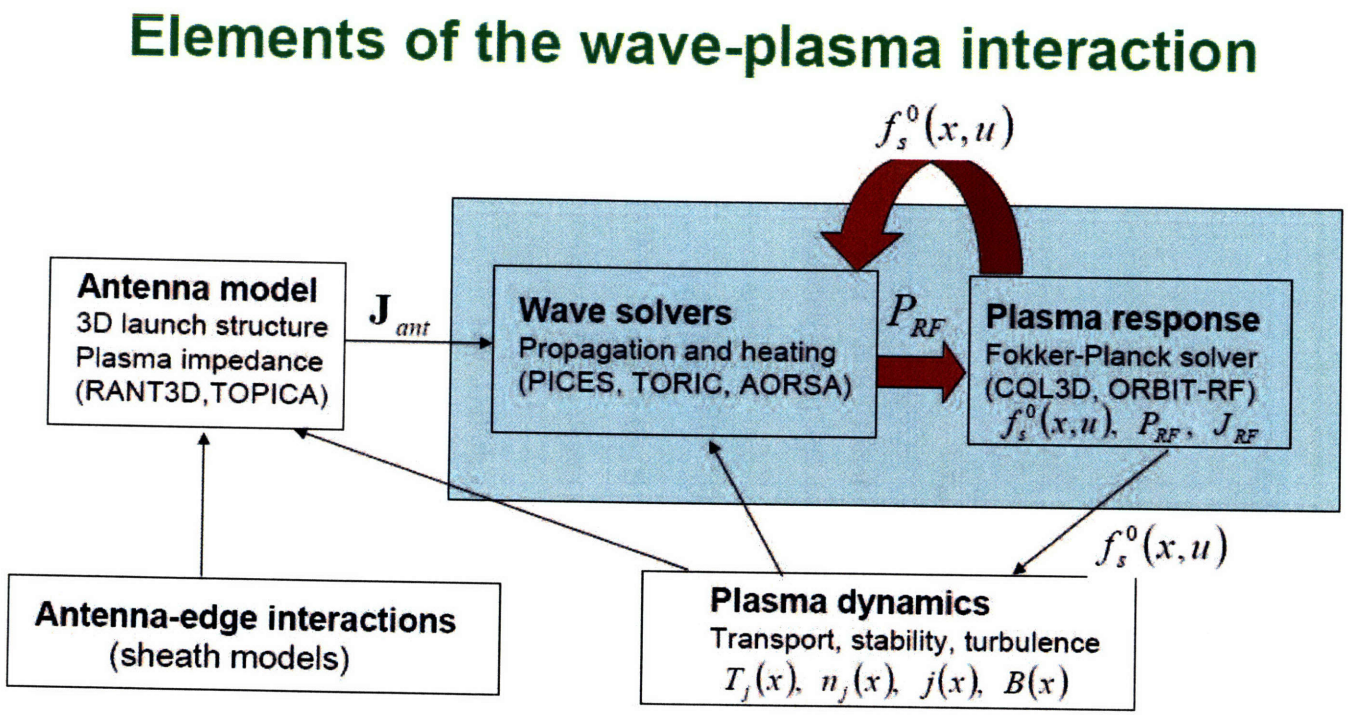

Figure 2-5: Top level description of the processes required for simulating wave-plasma interactions (Slide 4 from Jaeger[26] for the SciDac project).

solution is:

$$\ln f_{sx}(v) = -\frac{E}{T_e(1+\xi)}\left[1+\frac{R_b(T_e-T_b+\xi T_e)}{T_f(1+R_b+\xi)}K(E/E_b)\right] \tag{2.16}$$

$$\begin{aligned} \epsilon &= \frac{2}{3\sqrt{\pi}} \\ l_b &= (m_b/2T_b)^{1/2} \\ R_b &= Z_{eff} l_b/l_e \\ \xi &= \frac{\langle P_\perp \rangle t_s}{3nT_e} \end{aligned} \tag{2.17}$$

$$\begin{aligned} E_b(\xi) &= \frac{mT_b}{m_b}\left[\frac{1+R_b+\xi}{2\epsilon(1+\xi)}\right]^{2/3} \\ K(x) &= \frac{1}{x}\int_0^x \frac{du}{1+u^{3/2}} \end{aligned}$$

$\langle P_\perp \rangle$ is the absorbed RF power density and ξ is the Stix parameter. The free variable in the calculation is the absorbed power density. The Spitzer slowing down time is t_s and given by:

$$t_s = 1.98 \times 10^{19} \frac{AT_e^{3/2}}{Z^2 n_e \ln\Lambda} \tag{2.18}$$

where t_s is in seconds, n_e is in $1/m^3$, T_e in keV, and $\ln\Lambda \sim 16$.

At high energies the distribution reaches a Maxwellian with an effective temperature of:

$$T_{\text{lim}} \sim T_e(1+\xi)$$

Figure 2-6 gives examples of this distribution for different input power densities in a low density Alcator C-Mod plasma.

For any distribution, an effective temperature can be defined by taking an energy moment:

$$T_{\text{eff}} = \frac{2}{3}\langle E \rangle = \frac{\int \frac{1}{2} m v^2 f(\vec{v}) d\vec{v}}{\int f(\vec{v}) d\vec{v}}$$

For the isotropic Stix distribution, this becomes:

$$T_{\text{eff}} = \frac{2}{3}\langle E \rangle = \frac{\int_0^{v_{\text{lim}}} \frac{1}{2} m v^2 f_{sx}(v) 4\pi v^2 dv}{\int_0^{v_{\text{lim}}} f_{sx}(v) 4\pi v^2 dv} \tag{2.19}$$

where $v_{\text{lim}} = \sqrt{2E_{\text{lim}}/m}$ is the velocity of the particle with the largest confined orbit. This limit can lower the effective temperature noticeably. For example, a stable distribution with an infinite temperature is flat. However, if E_{lim} is 500 keV,

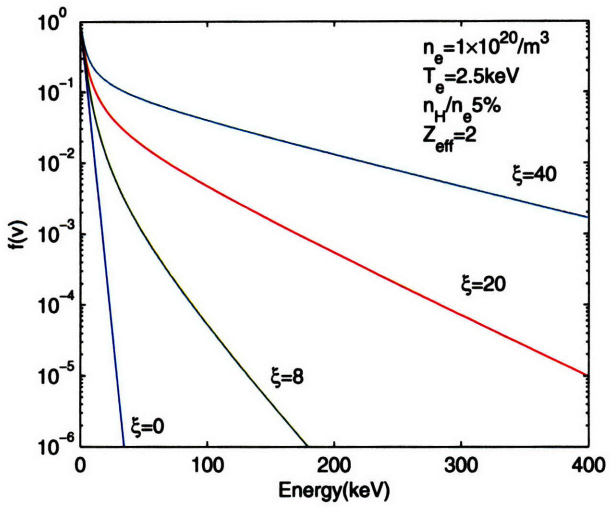

Figure 2-6: The Stix distribution using parameters typical of low density Alcator C-Mod plasmas. The Stix parameter, ξ, is varied with power densities from 0 to 5 W/cm^3. The distribution is Maxwellian when $\xi = 0$.

the average energy can only be $\sim$ 250 keV, even if the distribution has no slope. Typically this effect becomes important when $T_{\text{eff}} \sim E_{\text{lim}}/5$. For the 600 kA discharges in this thesis, the orbit induced energy limit at the core is in the $\sim$1 MeV level.

An analytical distribution that attempts to include the anisotropy of the minority ions is Hammett's model 2-D distribution based on Stix's results. Hammett[12] proposed that the anisotropy of the minority ions can be approximately accounted for in the Stix distribution by multiplying it with a pitch angle factor. The model in outboard mid-plane velocity coordinates, with $\mu = (v_\parallel/v)_{mid}$ is:

$$f_{sx2d}(E,\mu) = f_{sx}(E)K(E)\left[e^{-|\mu-\mu_*|/\sigma_\mu} + e^{-|\mu+\mu_*|/\sigma_\mu}\right] \tag{2.20}$$

$$\sigma_\mu = \left[\frac{Z_{eff}}{4A\left\langle Z_b^2/A_b\right\rangle\left(1+E^{3/2}/E_c^{3/2}\right)}\right]^{1/2} \tag{2.21}$$

where μ_* is the resonance layer in outboard mid-plane velocity coordinates, σ_μ the characteristic spread in pitch angle of the distribution due to fast ion-ion and fast ion-electron collisions, and $K(E)$ is a normalization constant such that:

$$f_{sx}(E) = \int_{-1}^{1} d\mu f_{sx2d}(E,\mu)$$

This outboard mid-plane 2-D distribution is used later to make estimates of average minority temperatures from anisotropic CNPA data. The flux surface averaged temperatures are determined from a distribution function using mid-plane coordinates via equation 51 from Catto[28]. These flux surface averaged temperatures are found to be very close or equivalent to the mid-plane pitch-angle averaged values. f_{sx2d} is normalized so that the mid-plane averaged power density and effective temperature are the input power density and effective temperature of f_{sx} in equation 2.20. It should be emphasized that this distribution is only a model and has not been derived from equation 2.13.

Before leaving this section, it should be specifically stated that these distributions do not include finite orbit or neoclassical diffusion effects. One way the finite orbit effects could affect the Stix distribution is through t_s. For example, an energetic and trapped minority ion in the core experiences a shorter slowing down time than the t_s calculated from the plasma parameters on its flux surface because part of its orbit encompasses a much colder part of the plasma due to large banana widths. In terms of diffusion effects, the dominant one in the core is typically sawteeth[11, 29]. There are also several neoclassical mechanisms, but they are usually small[12]. These diffusion effects all tend to move the fast ions spatially outward from the center of the plasma. In essence, when the above distributions are used to fit experimental data from a specified flux surface, the fit attempts to account for these finite orbit and neoclassical diffusion effects through varying the input power density. For synthetic diagnostic comparisons, these effects have to be included in the simulation if they are important, since by definition there are no free parameters.

For the plasmas in this thesis, the sawteeth are intentionally made smaller by running 600 kA discharges instead of the typical 800 kA. In fact, active CX CNPA count rates show little correlation with sawteeth for these discharges. Hence, sawteeth induced diffusion should be small. As for finite orbit size, the RF power is kept low for the shots in this thesis in order to keep the peak fast ion temperature below $\sim$ 100 keV in order to minimize orbit effects. As discussed later, reasonable agreement between the experimental data and detailed synthetic diagnostic is found without explicitly including these effects. However, their inclusion would improve the comparison since the synthetic minority spectra are spatially closer to $r/a \sim 0$ than the experimental data.

2.4 Coupled Wave and Fokker-Planck Solvers

In this thesis, the experimentally based minority proton temperatures and distributions are compared with several leading numerical packages with coupled wave and Fokker-Planck solvers. This includes the TRANSP based TORIC5/FPPRF code, GENRAY/CQL3D, and AORSA/CQL3D. In this section, a quick description of each of these packages is given with the appropriate references. None of these codes are complete and show why ICRF simulation is still an active area of research.

The TORIC5/FPPRF code is based on coupling Brambilla's full wave solver[18] with Hammett's bounce-averaged Fokker-Planck solver[12]. FPPRF is a 2-D bounce-averaged Fokker-Planck solver utilizing the physics discussed in the last section for ICRF heating. As for the wave solver, the TORIC5 code is fully 2-D and can account for arbitrary plasma equilibria. A symmetric N_ϕ spectrum with the dominant mode number is typically used. The main assumption made in the code is $k_\perp \rho < 1$ for the hot dielectric tensor[22]. This amounts to assuming that finite Larmor radius, or FLR, effects are small. Non-thermal species are modeled using equivalent bi-Maxwellian distributions, specifically $T_\perp$ and $T_\parallel$. This means that during each iteration between TORIC5 and FPPRF, the simulated 2-D distribution from FPPRF is averaged to calculate an equivalent $T_\perp$ and $T_\parallel$. In other words, the details of the minority distribution, including the trapping effects and density build-up around the heating resonance are lost. This thesis argues that this incomplete coupling and use of bi-Maxwellian distributions is the main reason for the observed discrepancies between the experimental data and the TORIC5/FPPRF simulation results documented in Chapter 4.

In contrast to TORIC, AORSA[16] is a 2-D full wave solver that makes no approximation to the hot dielectric tensor and can handle arbitrary distributions for the non-thermal species. The disadvantage to such a complete approach is the large computation resources required. This wave solver was recently coupled to the CQL3D[17] code which contains the same physics as FPPRF for ICRF heating. In general, CQL3D is a more versatile code in that it is also used for other wave-plasma interactions such as lower hybrid or electron cyclotron heating. The iteration process in AORSA/CQL3D retains the full 2-D distribution from CQL3D and thus accounts for the the effects missing in the TORIC5/FPPRF code. A complication with this new package is that the coupling code can only handle one N_ϕ at a time. Because the launched fast wave spectrum for heating is symmetric in N_ϕ, the launched power in the simulation should be distributed evenly between positive and negative N_ϕ, as done in TORIC5/FPPRF.

At the moment this is approximately simulated in AORSA/CQL3D by averaging the end results of the positive and negative N_ϕ cases. Detailed analysis using these preliminary AORSA/CQL3D results with a new synthetic diagnostic written as part of this thesis shows reasonable agreement with the experimental data. This is given in Chapter 5.

Lastly, results from the GENRAY/CQL3D package are also used in this thesis work. GENRAY[30] is a general purpose ray-tracing code. For the work here, the wave solver uses the cold plasma approximation for propagation. Finite temperature effects similar to equation 2.9 are used to calculate the absorption. Numerous rays are used in order to simulate the finite poloidal extent of the antenna and the symmetric N_ϕ spectrum. As discussed, the WKBJ approximation used in ray-tracing is not valid for the low density plasmas studied here and the GENRAY/CQL3D results are used in the synthetic diagnostic to show this. These calculations are also in Chapter 5.

For this thesis, neoclassical diffusion and finite orbit size effects are again not implemented in the Fokker-Planck solutions discussed above.

2.5 Conclusion

In this chapter, the theory for ICRF minority heating is reviewed in the context of the experimental and numerical work done for this thesis. First, the physics behind the minority heating scheme is studied using the cold plasma dispersion relationship. Efficient absorption of the fast wave is shown and discussed. Second, the details of the minority distribution under this RF drive is considered with the Fokker-Planck equation. Analytical steady-state solutions of this minority distribution are given. It is demonstrated that the details of this distribution are important in the absorption process. Hence, iteration between a wave and Fokker-Plank solver is required for detailed simulations of minority heating. Several leading simulation packages with coupled wave and Fokker-Planck solvers used in this thesis are reviewed.

Chapter 3

The Compact Neutral Particle Analyzer

3.1 Introduction

In this chapter, a detailed description of the new multi-channel Alcator C-Mod Compact Neutral Particle Analyzer is given. This new diagnostic is a major part of this thesis work and involved several innovations, such as post-shot pulse height analysis (PHA), compared with standard direct-sight neutral particle analyzers. These innovations were required for successful operation of the diagnostic in Alcator C-Mod's challenging plasma environment. PHA here refers to detector systems that determine the energy of each particle that interacts with the detector.

The rest of this chapter is broken into several sections. First, the design principles behind the CNPA are discussed and followed by a review of traditional PHA systems. Second, the CNPA setup and unique engineering features are described. Lastly, calibration results, plasma background measurements, and sample CX data are given.

3.2 Design Criteria and Operating Principles

Employing neutral particle analysis on Alcator C-Mod to measure the energetic minority tails as described in Chapters 1 and 2 involves challenges such as limited diagnostic port space, high plasma densities ($n_{e0} \sim 10^{20}/\mathrm{m}^3$), and low signal-to-noise. The desire for multiple viewing chords with limited space prohibits the use of traditional E$\|$B neutral particle analyzers with stripping cells and steering electromagnetic

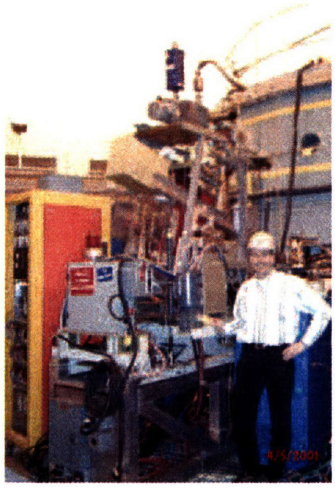

Figure 3-1: A E||B neutral particle analyzer previously installed on Alcator C-Mod.

fields. One of these large analyzers is shown in Figure 3-1. This difficulty compelled a unique compact multi-channel Si diode PHA solution with a direct view of the plasma and operated in post-shot PHA mode using fast digitization techniques. This setup has the advantages of extreme compactness, lower equipment costs, and relative simplicity compared with traditional mass spectroscopy methods. For the 2005 and 2006 Alcator C-Mod campaigns, this four-channel compact neutral particle analyzer was implemented and operated in both active and passive NPA mode. Similar diode-based direct-sight NPA setups have been successfully employed on other fusion devices[31]; but none with Alcator C-Mod's high plasma densities and relatively weak neutral beam, and then only with real-time PHA. Instead of traditional real-time PHA, the CNPA digitizes and stores the detector shaping amplifier voltage for post-shot software analysis[32]. This arrangement eliminates baseline shifts that can be significant during plasma events like sawtooth crashes, and allows for potential extraction of pile-up pulses. There are, however, some trade-offs in employing a Si diode system versus a normal neutral particle analyzer. First, without a steering electromagnetic field, the ability to diagnose different types of nuclei is lost. For Alcator C-Mod, this is not an issue since only energetic protons are created in ICRF heated D(H) plasmas, and the CNPA measures particles with energies greater than ~50 keV ($\gg T_{bulk}$ ~1-5 keV) only. Second, the direct-view diode system is susceptible to plasma soft x-ray and bulk deuterium CX noise, potentially more sensitive to cell EMF pickup, and has a lower counting capability than an E||B analyzer. The lowered counting capability comes from the fact that there are many more detectors on an E||B analyzer and they

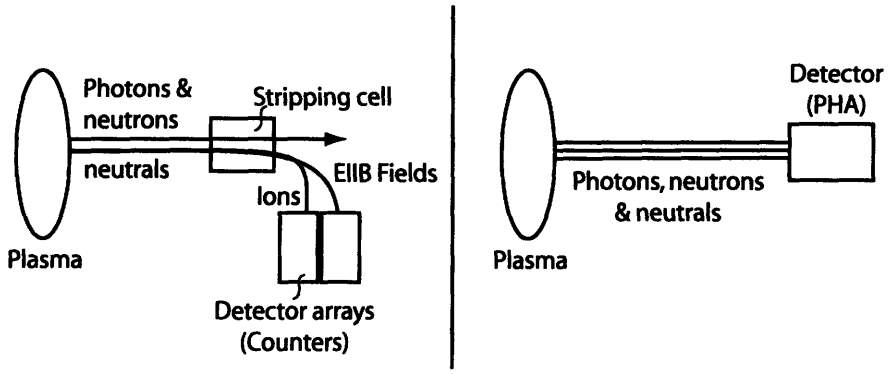

Figure 3-2: A schematic comparison of a traditional mass spectroscopy based neutral particle analyzer and a PHA based system with a direct view of the plasma.

do not need to be operated in PHA mode. These constraints impose some limits on the operation of the CNPA and are illustrated graphically in Figure 3-2.

Before fully describing the CNPA diagnostic, a review of PHA radiation detection systems is given below.

The CNPA system is based on using fast reversed biased silicon diodes as detectors for energetic hydrogen neutrals. These types of detectors, when operated in pulse-height analysis mode, permit detection and energy analysis of particles striking the detector. An extensive survey of these Si based systems is available from Knoll[33]. Here, a quick review of the principles and characteristics involved is given. For the purposes here, the energetic neutrals are essentially instantly ionized when they strike the detector or any other solid surface.

A typical Si diode based PHA system consists of a reversed biased silicon diode detector, a preamplifier, a shaping amplifier, and a pulse-height analyzer. Figure 3-3 illustrates this setup schematically. First an ion or photon hits the silicon detector and induces some current in system. This current comes from electron-hole pairs created in the diode at a rate of 1 hole/pair per $\sim$3.5 eV deposited by the energetic particle. For a strongly biased, thin, and undamaged diode, these hole-pairs traverse the entire detector in the nanosecond time range with basically no recombination. As for the electron hole-pair creation, ions have well defined ranges in materials and hence give up all of their energy to the detector as long as the diode is thick enough. Ions dominantly slow down through coulomb collisions with the electrons in the material. X-rays and gammas, on the other hand, do not have sharply defined ranges since their interaction mean free paths are large. Hence, only a certain fraction of the incident photons give up energy to the diode. The energy of the photon can also be deposited

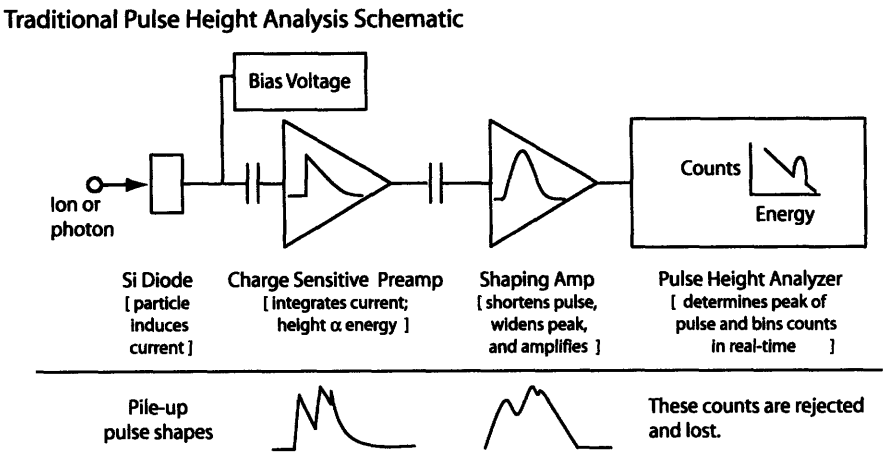

Figure 3-3: Top: A typical Si diode based particle detection pulse height analysis system. The characteristic shapes of the output voltage pulses for the preamplifier and amplifier are shown. Bottom: Preamplifier and amplifier voltage pulses during pile-up, caused by multiple incident particles during an effective collection time.

into the detector via different reactions, such as Compton scattering or photoelectric absorption. For this thesis, the energy required to create an electron-hole pair is essentially independent of the type of particle that deposited it. This is not the case for heavy ions, however.

Once the electron-hole pairs are created, this current is collected by the charge-sensitive preamplifier. The output of this preamplifier consists of a sharp voltage peak whose height is proportional to the energy deposited in the diode by the incident particle. This peak decays via a long exponential decline with fall-times greater than tens of μs. The fall-time is typically much longer than the transit time of hole-pairs in the diode to ensure complete charge collection. This pulse is then fed into a shaping amplifier, which reshapes the pulse into a Gaussian-like peak with a pulse width in the μs range. The peak is thus amplified and widened so that the pulse height analyzer can determine the height of the pulse and bin it into the appropriate channel. This spectrum of counts vs. bins, with the proper calibration, represent the desired counts vs. energy result.

Several complications can occur with this typical approach to radiation detection. First, as illustrated in the bottom graph of Figure 3-3, pile-up of voltage pulses can occur when the incident flux of particles is too large. Most PHA system can remove this pile-up, but the counts are effectively lost. The state-of-the art real-time detector systems are hence limited to a count rate of ~200k/s. Another problem is that electronic pickup in the system can result in spurious counts in the spectra.

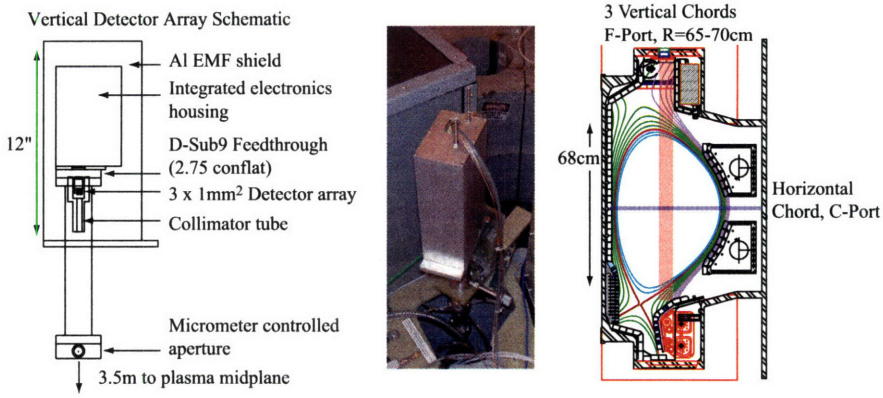

Figure 3-4: Schematic of the three channel vertical detector array and the system sightlines in the plasma. The horizontal detector is mounted on a SMA feedthrough and uses a traditional NIM preamp with shaping amplifier setup. Its distance to the plasma axis is ~2 m.

This can not be easily diagnosed from the pulse-height analyzer. Related to this issue is that the baseline could potentially shift during operation, which would result in incorrect spectra. Lastly, the pulse height analyzer discriminator threshold and binning widths must be set before the experiment, since the raw shaping amplifier voltage is not saved.

All of these problems can play a role if a typical direct-sight real-time PHA system is used on Alcator C-Mod. The CNPA, described in the next section, resolves most of these issues via fast digitization of the shaping amplifier voltage and post-shot pulse height analysis.

3.3 Description of the CNPA

The CNPA consists of three vertical and one horizontal sightlines, as illustrated in Figure 3-4. The horizontal channel is auxiliary and only available during periods when the Alcator C-Mod lower hybrid antenna is not installed. The sightlines of the diagnostic are arranged such that the three vertical chords view the phase space of the neutral distribution that is predicted to be most energetic, while the remaining horizontal channel sees neutrals that should be slower. The details of these sightlines and their detector systems are considered below.

The vertical viewing chords use a three channel, 3 x 1 mm^2 IRD AXUV-3ELA detector array with a nominal 1500 Å thick Al foil for shielding visible light, while the horizontal channel utilizes an IRD AXUVHS5 SMA mount detector with a nominal

1000 Å Al foil. The actual foil thicknesses are inferred using an alpha source and the SRIM code[34]. The foils are found to be 1550 Å and 1250 Å thick respectively. Hydrogen neutrals traversing the foil are assumed to be instantly ionized. The detectors are rated as 25 μm and 35 μm thick, have dead-layers less than 70 Å, and are chosen to minimize response to the plasma neutron and gamma background. In addition to light shielding, the protective foils shelter the diodes from CX neutral particles originating from the bulk plasma deuterium ions. The SRIM code predicts that the 1550 Å Al foil with an oxide layer is equivalent to a stopping power of ~14-21 keV for 50-350 keV hydrogen neutrals, and ~12-17 keV for a 1250 Å Al foil. Here, an effective attenuation of 20 and 17 keV is taken; the small error at higher energies is basically negligible. Consequently, the primary source of non-neutral noise for the diagnostic is the significant background plasma soft x-rays (~1-10 keV) that are not blocked. This noise limits the resolution of the CNPA and typically the maximum permissible neutral count rate. This issue is analyzed in detail in the next section. A variable knife-edge aperture determines the étendue of the vertical detectors; see Figure 3-4. Normally, the vertical channels are operated with an étendue of $\sim 6 \times 10^{-12}$ m^2-str. The vertical channels cover R from ~65 to 70 cm, depending on the aperture setting. Here they are referred to as Ch1 to 3, with Ch1 being the innermost channel, and Ch3 the outermost. Typically, each diode in the array has a viewing cone width of ~2 cm at the mid-plane and hence there is some overlap between the three channels. The horizontal channel, or Ch4, employs a permanent 6.3 cm long passivated stainless tube and pinhole (~0.25 mm D) for collimation. Its viewing cone width is ~3 cm on-axis with an étendue similar to the vertical channels. Figure 3-5 illustrates the horizontal channel setup.

Currently, the vertical channels view the radial injected DNB perpendicularly, while the horizontal channel is only available for passive CX experiments. With the DNB, there is some spatial localization of the CX signal for the vertical channels. All four channels essentially see particles with local $v_\parallel/v \leq \sim 5 \times 10^{-3}$. Thus, the vertical channels are geared toward observing particles with large $v_\perp$ at their banana tips. Again, the horizontal channel is designed to view a portion of the minority proton phase space that is weaker. This is discussed further with Fokker-Planck simulations.

Based on RF/Fokker-Planck solvers like GENRAY/CQL3D[17] and FPPRF[12], energetic minority distributions in low density Alcator C-Mod plasmas are expected to be noticeably anisotropic in phase space, as discussed in Chapter 2. Figure 3-6 reviews the CQL3D simulation of a limited L-mode low density Alcator C-Mod shot which clearly illustrates the anisotropy of the fast proton distribution at the

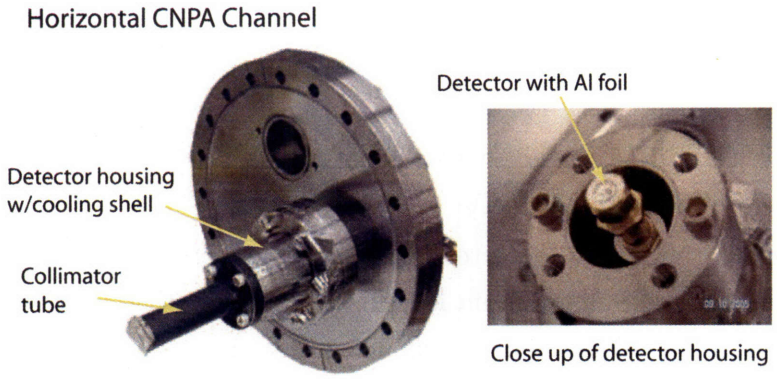

Figure 3-5: The CNPA horizontal channel. The detector consists of a re-entrant housing with an isolated SMA feedthrough. Coolant can be pumped through the housing from the air side for low-temperature operation.

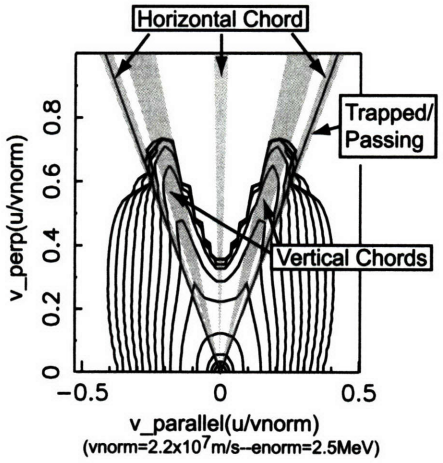

Figure 3-6: Contour plot of minority hydrogen outboard mid-plane velocity at r/a=0.23 for a low density Alcator C-Mod shot from CQL3D simulations. The regions of the distribution viewed by the CNPA are qualitatively highlighted. The trapped/passing boundary is also indicated.

outer mid-plane. The parts of the distribution viewed by the vertical and horizontal detectors are highlighted, and show that the vertical channels should view the most energetic portions of the hydrogen distribution. These energetic 'rabbit ears' in the outer mid-plane velocity distribution are a result of fast ion resonance localization, again characterized by energetic minority ions with banana tips near the resonant major radius. The vertical channels are thus designed to measure these minority ions at their turning point or banana tips, where the local $v_{\|}$ is ~ 0.

Electronically, the vertical detectors are connected directly to the integrated electronics housing via a D-Sub9 vacuum feedthrough. The vertical channel array comes as an 8-pin DIP and is mounted on a Teflon socket with ~2.5 cm long, 30 gauge copper wire connections to the feedthrough. The integrated electronics housing contains three sets of AC-coupled Cremat CR-110 preamplifiers with 140 μs fall-time connected to fixed gain Gaussian shaping amplifiers with a 1 μs pulse width, and mounted on a primary motherboard. The amplifiers are developed in-house for the Alcator C-Mod HXR diagnostic[35]. Each set of preamplifiers and amplifiers is shielded from each other via an internal Al shield in the housing. This significantly reduces cross-talk between the channels to approximately 8%. The amplifier voltage outputs are then digitized at 10 MHz by a D-tacq Dt216 CPCI digitizer via 18m of RG316 cables with SMA connectors. The electronic housing is an iridized Al enclosure and contains conducting gaskets for RF shielding; this box is placed within an additional Al RF shield that also covers the detectors. This Al shield eliminates EMF noise and pickup from the EF coils and DNB due to typical machine operation. The operating range of the vertical channels is ~50-350 keV, limited by the shaping amplifier electronic rail, the attenuation of the Al foil, and the baseline noise caused by the soft x-ray flux. Figure 3-7 shows further details of the vertical channels electronics.

The horizontal channel uses a more typical NIM setup, with the detector AC coupled to an Ortec 142 preamp via a 7.6 cm long RG316 SMA cable. The Ortec preamp has a fall-time of 44 μs. The use of preamps with fast fall times for the CNPA is critical as slower fall-times allow the non-neutral signal to saturate the preamplifier quickly. A ~1 m long RG316 cable connects the preamp to an Ortec 572 shaping amplifier usually operated with a shaping time of 0.25 μs and a 100x gain, giving a base width of ~1.2 μs for each pulse. The amplifier voltage output is again digitized by a D-tacq Dt216 CPCI digitizer operated at 10 MHz and connected with 6 m of RG316 cable. Noise and pickup due to EMF are less of an issue for the horizontal channel because of its location. The electronics limit the horizontal channel to ~4 MeV for PHA for the above settings but because the amplifier parameters

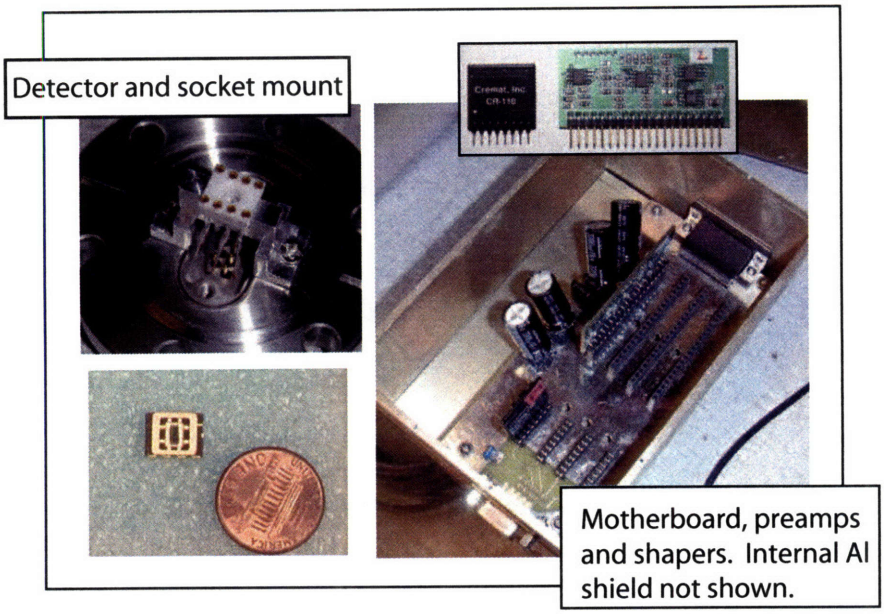

Figure 3-7: Left: The three channel vertical detector and feedthrough socket. Right: Interior of the integrated electronics housing for the vertical channels

are easily changeable, different energy ranges can be chosen depending on expected plasma conditions.

The D-tacq Dt216 digitizer is the basis of the post-shot PHA system. Enough memory is available on the digitizer for an entire Alcator C-Mod shot, typically around 2 s. These data, usually ~30-40 Mb, are then processed after the shot to extract pulse-height information. The removal of real-time processing constraints allows for sophisticated PHA software routines, such as fitting of pile-up pulses. In addition, the full voltage data are instrumental in discerning various electronic pickups, plasma induced noise, and preamplifier saturation for the CNPA. Currently, the CNPA is run at maximum count rates of <100k/s, which results in little pileup; hence the PHA routine employed does not perform Gaussian fits of each pulse. However, the routine does account for baseline shifts and rejects the small amount of pileup that is present.

3.4 Calibration and PHA routine

The CNPA is calibrated with a combination of sources and the motherboard's built-in test circuit. The vertical channels with fixed gains are calibrated with an Am241 59.5 keV gamma source, a 60-140 keV deuterium ion beam operated by the PSFC HEDP group, and the Alcator C-Mod DNB at 33-46 keV during beam-into-gas ex-

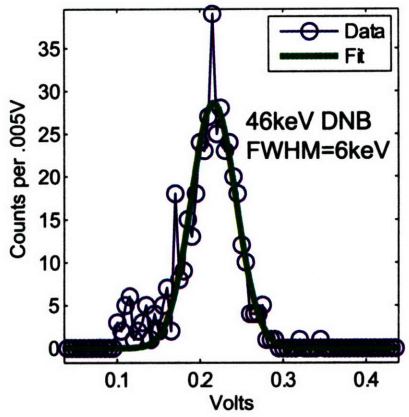

Figure 3-8: Pulse-height spectrum from the vertical array for a beam-into-gas calibration with the DNB at 46 keV. The 46 keV DNB neutrals are slowed to ~24 keV by the CNPA protective foil. The FWHM of the DNB fit is 6 keV and involves a convolution of the energy spread from the detector, the DNB, and the straggling through the Al foil.

periments. The Rutherford backscattered flux from a thin gold foil is used with the deuterium beam to minimize potentially damaging fluxes to the detectors. The protective foil was not installed for the deuterium ion beam calibration. Complete documentation of these calibration experiments are in Appendix A. The beam-into-gas DNB data were taken with the protective Al foil in place; DNB neutrals at 33-46 keV are thus slowed to ~13-24 keV before they hit the detector. Additionally, the DNB calibration points are scaled by ~5%, based on known decreased detector efficiencies at these lower energies[36].

Figures 3-8 and 3-9 show some of the calibration results for Ch3 of the vertical array using the above sources. The voltage to keV response for the channel is $V(E) = 0.011E - 0.043$. All three channels have slopes within ~5% of each other. In general the linear calibration fits are excellent. The total error in the calibration is estimated to be ~8%.

The voltage to keV fits for Ch1-3 without the CNPA 1550 Å Al protective foil are:

$$V(E)_1 = 0.0117E - 0.0485 \tag{3.1}$$

$$V(E)_2 = 0.0114E - 0.0412 \tag{3.2}$$

$$V(E)_3 = 0.0111E - 0.0429 \tag{3.3}$$

The horizontal CNPA channel is also calibrated with multiple sources; the Am241

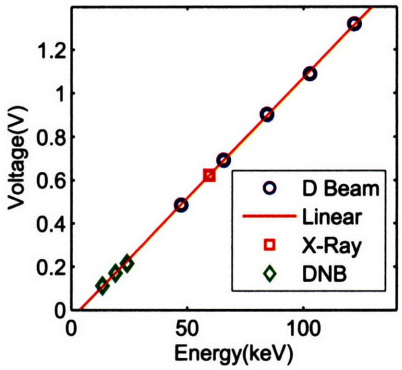

Figure 3-9: Summary of the calibration data for Ch3 of the CNPA

gamma and alpha source, the preamplifier's test circuit, and the DNB at 46 keV. The ability to switch the voltage gain on the Ortec 572 shaping amplifier permits the use of the alpha source at 5.5 MeV without an attenuator. The horizontal channel voltage to keV calibration gives V(E)=0.0026E +/-8% for the settings described in the previous section.

The PHA routine used for both calibration and plasma operation involves the following steps: (1) determine an average baseline by smoothing the raw voltage baseline data over a specific period, typically 0.1ms (2) subtract the voltage data with this smoothed baseline (3) find voltage peaks above a specified threshold (4) reject pile-up by considering the length of time between adjacent voltage peaks (5) find the peak of each pulse and store this value along with the time of the pulse. No fitting is used to determine the peak so there is a small tendency to underestimate the real peak value if the digitization rate is low compared with the pulse width. Figure 3-10 illustrates graphically some of these steps during a large sawtooth crash and clearly shows the importance of an accurate baseline determination. The figure shows voltage data from the horizontal channel equipped with the Ortec 572 module which uses an automatic baseline restoration circuit. Plainly, a traditional PHA approach would have missed counts with this skewed baseline since the voltage threshold discriminator is constant, causing a false correlation with sawtooth crashes. The baseline shifts in the vertical channels are significantly smaller. In general, it is likely that these shifts are related to the AC coupling time constants between each stage of the electronics and the sudden large rise in the detector baseline current due to the sawtooth crash.

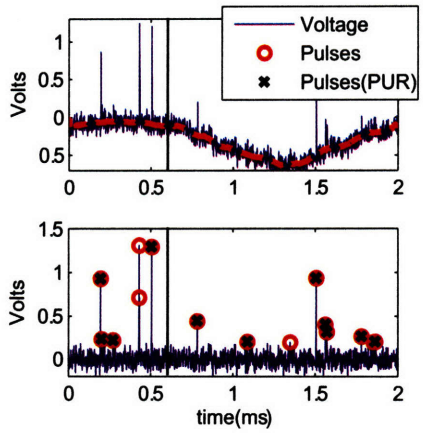

Figure 3-10: PHA during a large sawtooth crash from shot 1050818008. The time axis in the plot is shifted for convenience. The first panel shows the shaping amplifier voltage from the horizontal channel during the crash, which occurs at t ~0.6 ms (vertical solid line). The soft x-ray flux from the central vertical chord goes from 90 to 60 kW/m^2 during this period. The baseline shift is caused by the sudden burst of x-rays and light of a large crash. The dash line is the baseline used by the post-shot PHA routine to correct for this large shift. The second panel shows the corrected voltage data with counts above 0.2 V marked by the PHA routine. Pulses(PUR) indicates counts that pass the pile-up check.

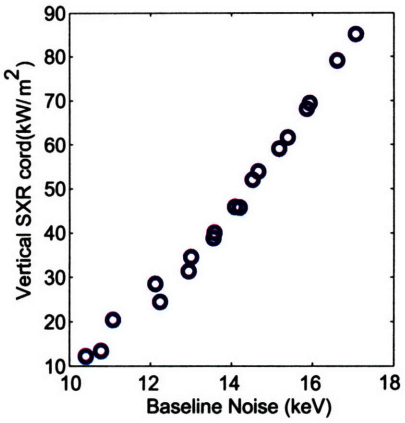

Figure 3-11: Typical baseline standard deviation as a function of soft x-ray flux for the vertical channels. The data shown is taken from the ramp-up phase of two low density L-mode discharges (1050818008 and 1050818011) before the application of RF.

3.5 Response to Plasma Background

The detectors are verified to have almost no response to the neutron and gamma background, allowing for operation in passive mode without background subtraction. The maximum neutron rate on C-Mod is typically $\sim 10^{14}$/s, resulting in only $\sim$10 counts above 50 keV for the CNPA during a shot. The most significant non-neutral noise induced by the plasma is via soft x-rays, which results in increasing fluctuations on the baseline and limits the energy resolution of the detected neutral particles. These x-rays have energies of $\sim$1-10 keV, pass through the Al foil easily, and have mean free paths much less than the detector active thickness. The x-rays also have the adverse effect of raising the energy threshold of detectable neutrals. Figure 3-11 is a plot of the baseline noise level as a function of soft x-ray emittance for a low density (n_{e0} $\sim 10^{20}/\mathrm{m}^3$), limited, L-mode shots that have a passive >70 keV neutral count rate of $\sim$10k/s. Lower single null(LSN) shots typically have smaller soft x-ray emittance and thus permit higher count rates with the same resolution. This count rate/resolution trade-off can make it difficult to study transient fast ion events, such as fast ion diffusion from sawteeth. With low density plasmas, the DNB can increase the neutral signal by approximately an order of magnitude. These signal-to-noise issues with the CNPA are probably unique to Alcator C-Mod, as other devices typically operate at much lower densities and employ strong heating neutral beams. Both of these differences can increase the fast neutral signal-to-noise dramatically.

3.6 Experimental Data

To give an example of spectra taken by the CNPA, a basic low density, LSN, 5.4 T, 600 kA, 0.6 MW, ~7% minority ICRF D(H) Alcator C-Mod shot, 1051206002, is now examined. Both passive and active CX data are available for this discharge as the DNB fired from t=1 to 1.15 s at full power. The relevant plasma parameters along with the count rates for the CNPA are shown in Figure 3-12. The raw spectra using the PHA routine described above are illustrated in Figure 3-13.

Analysis and modeling for this data is fully discussed in the next Chapter; the raw data are shown here to provide a sample of what the CNPA detects.

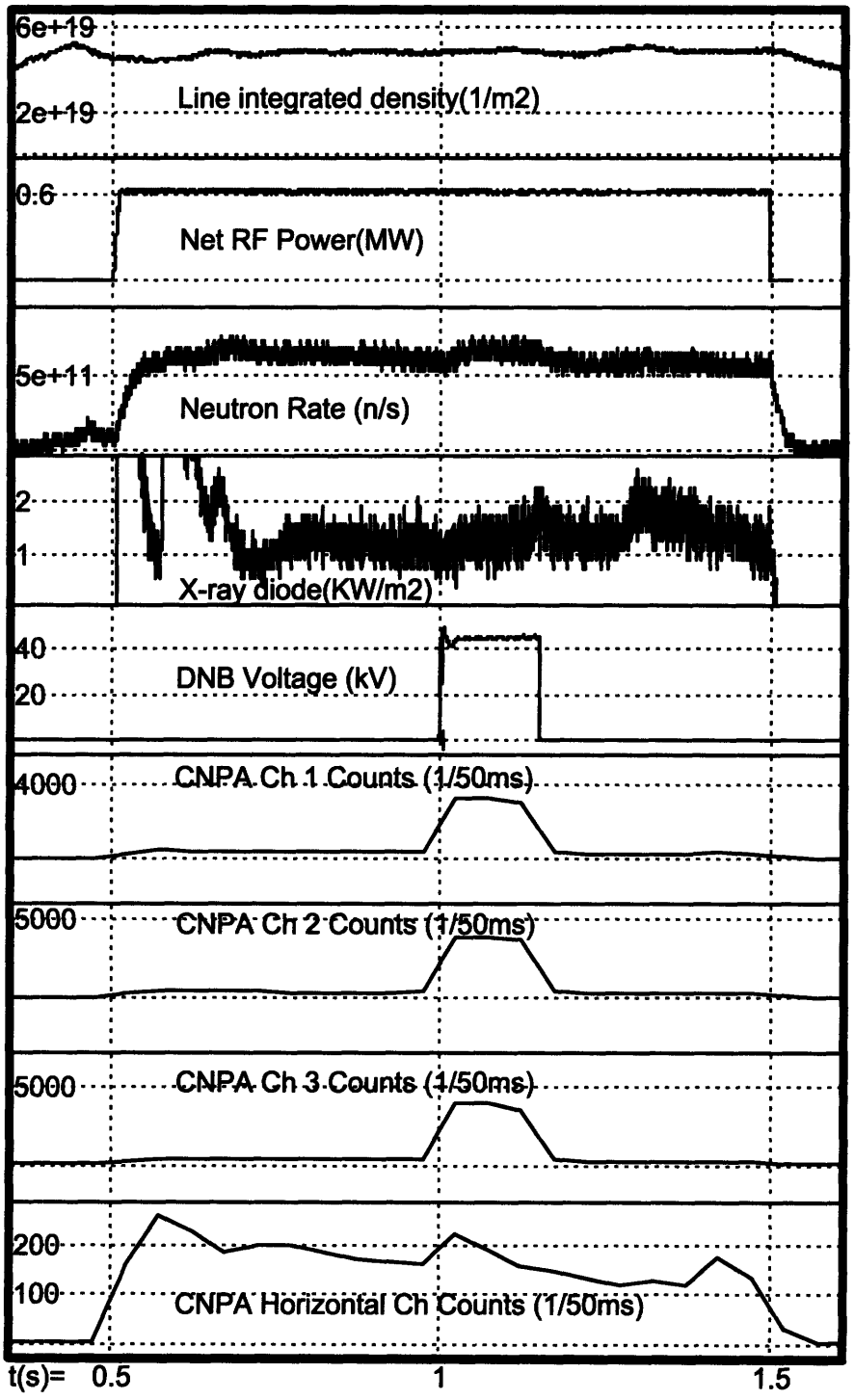

Figure 3-12: Plasma parameters and CNPA count rates for shot 1051206002. The DNB fires from t=1-1.15 s. A large increase in count rate occurs for the channels viewing the beam. Fast particles are only detected when the RF is on.

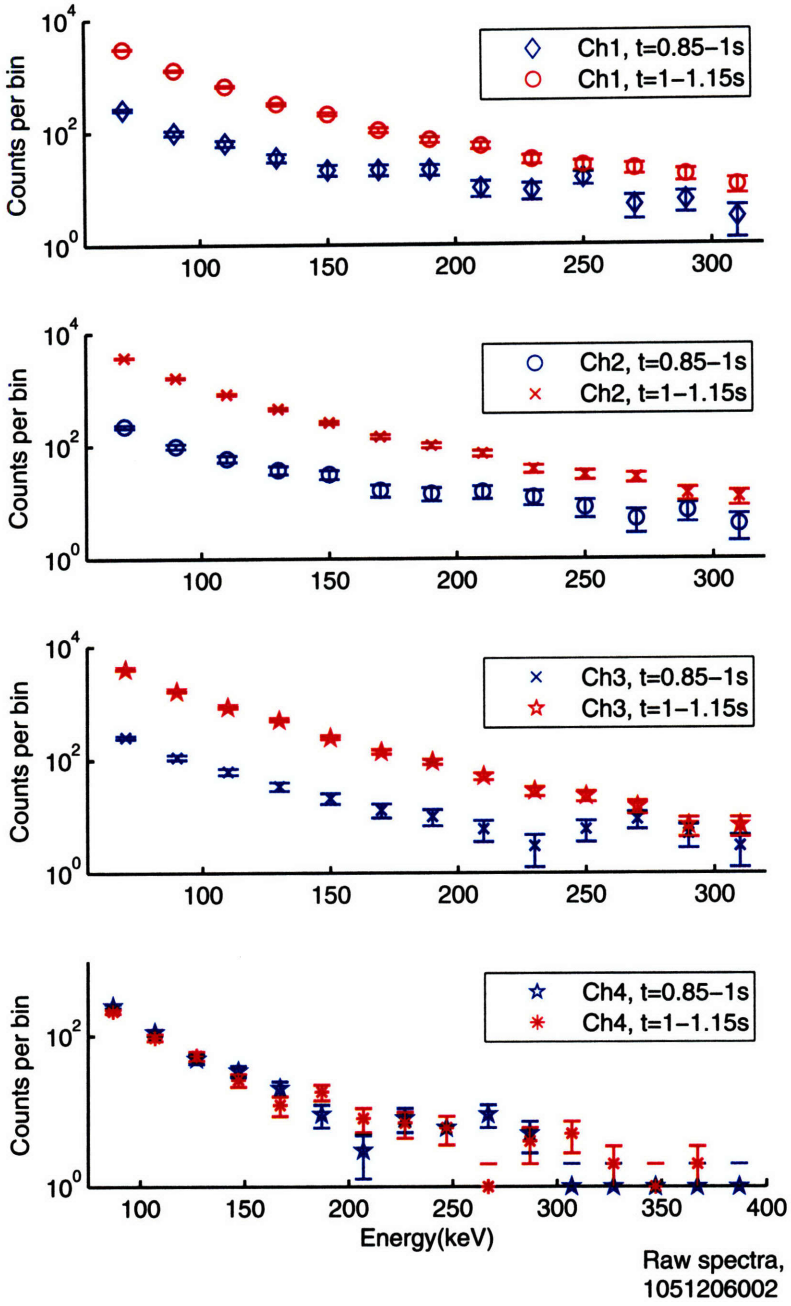

Figure 3-13: CNPA Ch1-4 spectra from t=0.85-1 s and t=1.0-1.15 s. The passive and active CX spectra from Ch1-3 are different and easily distinguished from each other.

Chapter 4

Analysis with Simple Model

4.1 Introduction

In this chapter, a relatively simple model for interpreting the CNPA active and passive CX data illustrated in the last chapter is discussed. By making some simplifying assumptions and modeling all the major neutralization electron donors, the peak fast proton temperatures at different pitch angles and their effective spatial location are inferred. Flux-surface averaged temperatures are also estimated using Hammett's 2-D analytic minority ion model distribution. Lastly, for specific scenarios, the CNPA can provide an estimate of the boron impurity density.

In theory, detailed minority proton temperature and RF power deposition profiles can be inferred via a full synthetic diagnostic implemented in a coupled RF/Fokker-Planck solver package. The next chapter documents a synthetic diagnostic implemented for the CQL3D[17] code as part of this thesis. However, because of the computationally expensive nature of such a simulated diagnostic, the simple model is more convenient for scaling studies where many shots have to be studied with different model input parameters.

Using this model, the peak proton temperature data are analyzed and found to scale approximately with a scaling based on the Stix parameter. Additionally, contrary to what is typically assumed for Alcator C-Mod discharges with heating resonance on-axis, the peak proton temperatures for all the analyzed cases are found to occur off-axis. Here, off-axis refers to flux surfaces greater than $r/a = 0$. This conclusion is independently verified by estimates of the $r/a \sim 0$ fast proton temperature inferred from a sawteeth reheat analysis. This off-axis effect is a significant physics result of the thesis. A possible explanation is provided via a comparison of simulation results between the TRANSP[37] based TORIC5/FPPRF[18, 12] and

AORSA[16]/CQL3D Full wave/Fokker-Planck (FW/FP) codes. This explanation is further bolstered by the synthetic diagnostic results in the next chapter. To note, the scaling data with fast protons are first time results for Alcator C-Mod. These FW/FP analyses represent the first comparison between predictions of such detailed codes and extensive minority ion experimental measurements.

The rest of this chapter is outlined as follows. First, the simple model or technique used by JET, JT-60U, and TFTR NPA is reviewed and extended for Alcator C-Mod plasmas. A significant aside is taken to cover the impurity, background neutral, diagnostic neutral beam, and halo models required for implementing this modified technique. Following this, the modified model is applied to sample low density LSN Alcator C-Mod plasmas. Afterwards, the scaling study is performed. The results from the model for shots with good CNPA active and passive CX data are shown. Also discussed are the inferred spatial location of the peak proton temperature. The sawteeth reheat analysis results are given which independently support the off-axis heating conclusions of the scaling study. Lastly, the FW/FP simulation results are displayed to provide an explanation for this off-axis heating discovery.

4.2 Description of the Simple Model

The number of particles with energies between E and $E + dE$ striking one of the CNPA detectors per second is[38]:

$$F(E)dE = v_0^2 dv_0 A\Omega \int_{-a}^{a} P(x, \vec{v_0}) \left[\sum_s f_p(x, \vec{v_0}) \sigma_{s,cx}(v_{s,rel}) v_{s,rel} n_s(x) \right] dx \qquad (4.1)$$

where the sum is taken over contributions from different electron donor species s. a and $-a$ are the limits of the sightline, v is the minority proton velocity, $f_p(\vec{v}, x)$ the minority proton distribution, $\sigma_{s,cx}$ the CX cross section based on the relative velocity of the minority ion and donor species, $P(x, v)$ the penetrability of the minority neutral hydrogen after CX out of the plasma, $A\Omega$ is the étendue, and $n_s(x)$ represents the density of the electron donor. Typically this donor is a neutral beam hydrogen or residue deuterium neutral, but at proton energies greater than ~100 keV CX with background hydrogen-like (HL) impurities can be important[39]; some of these HL impurity CX cross sections are plotted in Figure 4-1 [40]. A delta function in velocity, $\delta(\vec{v} - \vec{V_s})$, is assumed for the donor species. The pitch angle taken in f_p and $v_{s,rel}$ is determined by the geometry of the sightline, since an NPA by definition can only

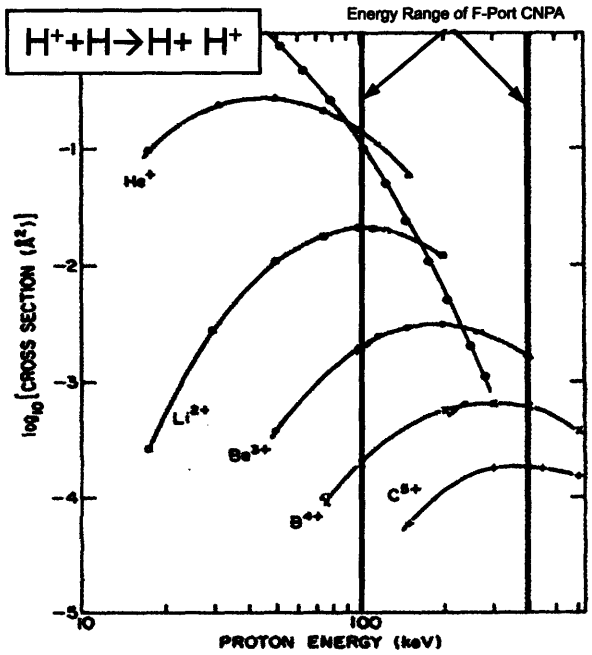

Figure 4-1: $H^+ + A^{Z+} \rightarrow H^0 + A^{(Z-1)+}$ cross sections for various typical light impurities in Tokamak plasmas. The hydrogen-hydrogen charge-exchange cross section is also shown for comparison, along with the CNPA F-Port top array energy limit. This plot is modified from Figure 1 of Winter's paper[40].

detect particles with velocities nearly aligned with its viewing chord. One rigorous method to interpret CNPA data is to implement a synthetic diagnostic based on equation 4.1 in CQL3D, similar to the method used by Hammett for passive CX analysis on PLT[12]. Because the DNB has a finite diameter (FWHM ~12 cm) with spatial and phase space profiles, spatial localization of the CNPA signal using active analysis is incomplete. Using a synthetic diagnostic technique allows the spatial RF power deposition and temperature profiles to be inferred from the line-integrated active or passive CNPA measurements. Even for a well-localized beam, detailed power and temperature profiles require a synthetic diagnostic for active neutral particle analysis. This work is documented in the next chapter.

The synthetic diagnostic approach is useful but very time intensive. A much faster technique is used by several authors to infer an effective or peak minority distribution from high-energy NPA spectra on large machines like TFTR, JT-60, and JET during on-axis ICRF heating[41, 42, 39]. These machines all operate(d) with vertical viewing NPAs and sightlines that are either on or very close to the heating

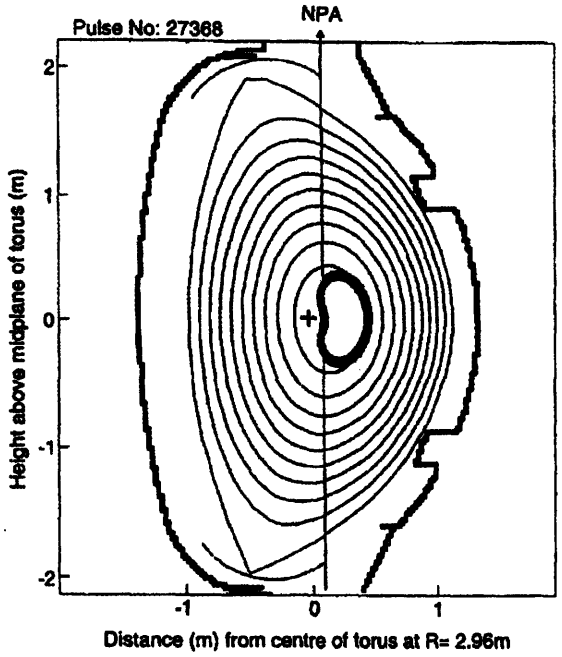

FIG. 4. Poloidal cross-section of the JET torus showing the magnetic configuration of the plasma. The heavy line is the poloidal projection of the orbit of an 0.5 MeV proton with $v_Z/v = 2 \times 10^2$, with the tip of its banana orbit located on the NPA line of sight and vertically inside the ICRF power deposition region.

Figure 4-2: Figure 4 from Korotkov[39] showing the JET vertical NPA sightline and the orbit of a 500 keV proton detectable by the JET NPA. v_Z in the figure caption refers to $v_\perp$.

resonance layer similar to Ch1-3 of the CNPA. Mid-plane based NPA results similar to Ch4 of the CNPA are also available from TFTR[11]. Theoretically the vertical NPAs with sightlines on or near the resonance measure the hottest pitch angle, as discussed in Chapter 2. Figure 4-2 illustrates the setup for the JET experiment. After reviewing the model and discussing its assumptions, this simple method is modified and applied to low density Alcator C-Mod plasmas. The simple model assumes that the bulk of the hot minority proton tail is localized spatially near the center of the plasma, with a spatial width smaller than the characteristic scale length of the bulk plasma parameters, and that the electron donors are known. Additionally, impurity equilibrium models that account for beam-created HL impurity electron donors are needed if impurity CX is important in the NPA energy range, since these beam-created impurity populations can not be subtracted out of the background.

Mathematically, for a detector with a radial sightline crossing the center of the plasma, these assumptions result in a sightline averaged minority proton distribution given by:

$$f_{a,p}(v) \sim \frac{F(E)}{\sum_s n_s \sigma_{s,cx}(E_{s,rel}) E_{s,rel}^{1/2} E^{1/2} P(E)} \tag{4.2}$$

Where $P(E)$ is now the penetrability of minority hydrogen neutrals from the center of the plasma, $E_{s,rel}$ the relative collision energy between the minority proton and electron donor species s, and E the energy of the minority proton. Concerning off-axis channels, derived distributions from these sightlines not crossing the center of the plasma are weighted by different minor radii. In ICRF experiments in TFTR and JET, the distribution at high energies was described by a simple exponential, $\exp(-E/T_p)$, where T_p is an estimate of the minority temperature; it is an approximate peak minority temperature in the sightline if the fitted portion of the NPA spectra is greater than T_p, since the counts in those parts of the spectra are dominated by the hottest piece of the viewing chord. In this thesis, the denominator of this equation is referred to as the CX factor.

Simplification occurs when a single hydrogen-like impurity is the dominant electron provider[42, 41, 11]; for these cases the beam therefore serves only to create more of the dominant HL impurity for charge-exchange and no beam or impurity density information is needed. For the case of multiple neutralization impurity species, the beam penetration and profiles have to be modeled accurately enough to infer the relative densities of the different electron donors. In most cases, however, only the central impurity densities are modeled because of the localized fast ion tail assumption[39, 42].

In fact, the high energy NPAs on TFTR, JT-60, and JET all operate(d) in the $\geq$300 keV energy regimes where direct CX from hydrogen or deuterium beam components and background neutrals are negligible. The localized minority tail assumption can also be good since even a ~500 keV hydrogen ion in these large machines is localized to the core, as shown by Figure 4-2. This simple model with impurity CX allows reliable measurements of the fast proton tail on these machines. However, because the neutralization source varies slowly across the plasma, this model as implemented on these large machines cannot verify that the fast ion tail is not at r/a=0 unless it is drastically off-axis[11]. Figure 4-3 illustrates this dynamic.

Applying this JET model on Alcator C-Mod is more complicated, as both direct beam and HL boron or helium CX are important because the CNPA operates in the 50-350 keV range. Cutting off the spectra below 300 keV is not acceptable because the fast protons above 300keV are not necessarily representative of the core minority

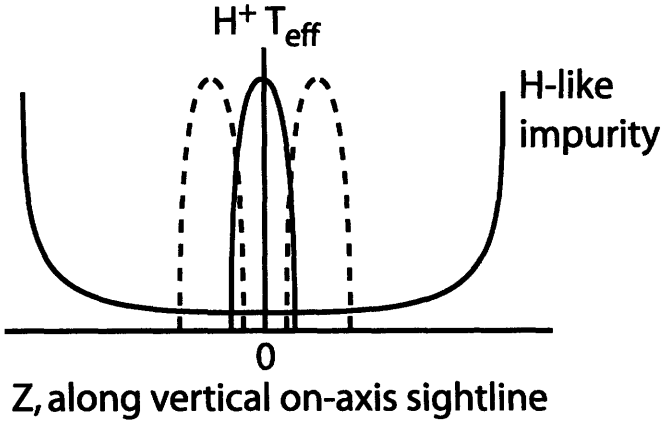

Figure 4-3: Graphical illustration of the assumptions used in the JET, JT-60U, and TFTR simple NPA model. The solid line represents the assumed fast ion temperature profile. However, because of the relative constant neutralization profile and small attenuation of the energetic neutral signal, the model is not able to differentiate between the dash and solid fast ion profiles. The dashed profiles are symmetric because they are on the same flux surface.

tail, since they have very large banana orbits. Additionally the count rate at these high energies is relatively low for the CNPA. Hence, the beam components, beam halo, and beam induced HL impurity all have to be modeled. Additionally, because of the small size of Alcator C-Mod, spatial details of the neutrals have to be accounted for. Fortuitously, modeling these processes properly results in an additional output from the simple model, specifically the approximate location of the peak proton tail. Lastly, the width of the fast ion profile can be large relative to the scale lengths of the plasma, further complicating the interpretation. Figure 4-4 schematically shows this on a poloidal cross-section of a typical LSN discharge. Because of the above differences, equation 4.2 is modified for the CNPA data. Specifically, $f_{a,p}(v)$ and n_s are now allowed to spatially vary. For simplicity, $P(E)$ is still calculated assuming the fast proton source at $Z = 0$; this is approximately correct since even if the fast protons are located away from the center the profile is symmetric about $Z = 0$. As discussed, the fast ion profiles in Alcator C-Mod can have spatial widths wider than the characteristic scale lengths of the neutral source and sometimes the bulk plasma parameters. This sort of detail can really only be accounted for with a detailed synthetic diagnostic. In order to make progress with the simple model, it is assumed that the fast proton source is peaked at a specific flux surface, and that all the CNPA data are from that location. With that assumption, by modeling the active and

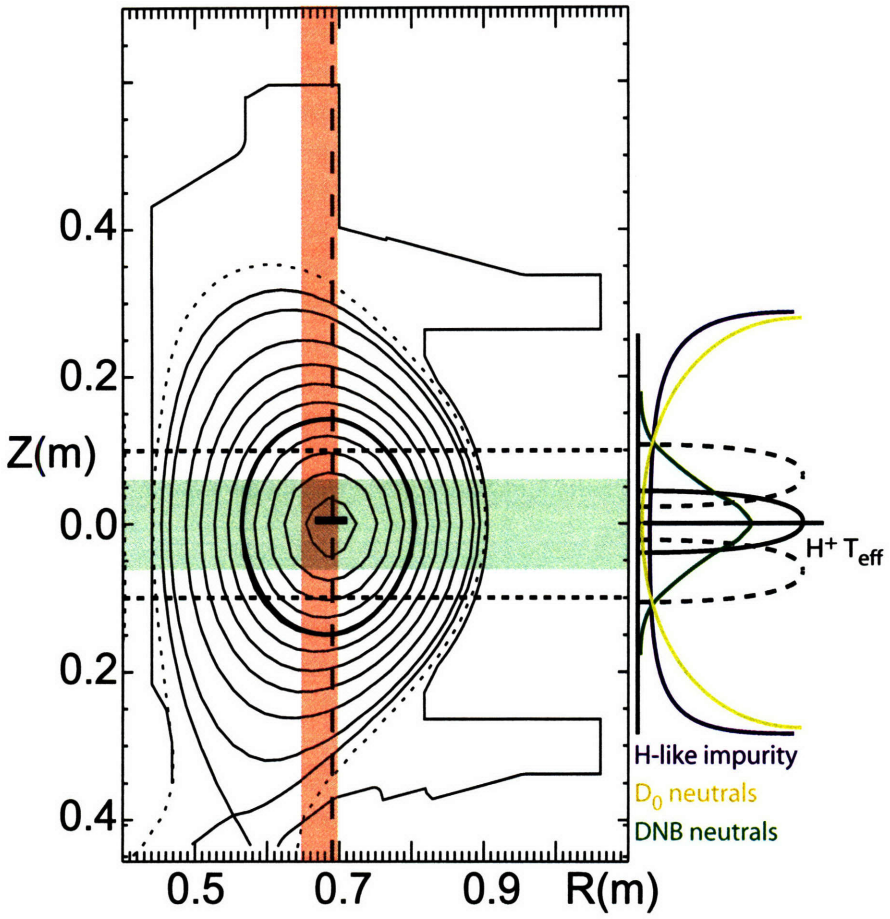

Figure 4-4: LSN Alcator C-Mod discharge with ICRF, CNPA, and DNB overlays. The red vertical highlight indicates the CNPA vertical sightlines. The brown vertical dash line corresponds to the ICRF resonance layer of a typical 5.4 T D(H) shot, with the small horizontal black line in the middle indicating the approximate width of the Doppler-broaden ICRF resonance for a hydrogen ion with $v_{\|}$ ~20 keV. The green horizontal highlight shows the region up to the FWHM of the DNB, with the dashed horizontal black lines representing the 95% mark. The thickened flux surface marks the r/a~0.4 point. On the right is the plot of the different neutralization sources and a fast ion profile along the vertical sightlines. In the 50-350 keV range, direct CX from DNB components and halos, background thermal neutrals, and hydrogen-like impurity are all significant. Spatially, the donor profiles are not approximately constant as for the larger machines. Hence, the location of the fast ion peak can be inferred if the profiles are modeled properly.

passive CX sources properly and comparing the count rates between the two cases, an estimate of the location of the peak proton temperature can be made. This Z location is denoted Z_p. As for the proton temperature, it will be shown that the minority proton temperatures inferred from active CX are not very sensitive to the assumed source location because halos and third component neutrals dominate the fast proton neutralization in the lower density Alcator C-Mod plasmas studied for this thesis. To note, this assumption and the model break down for very hot tails when the CNPA spectra is no longer dominated by the peak temperature in the sightline, unless the fast proton spatial profile is approximately a broad step function (i.e. composed of one effective temperature). This upper peak temperature bound is estimated to be around 120-130 keV due to various factors best discussed with the sample shot analyses later in the chapter. Lastly, it should be stated that care must be taken when using sightline data that does not cross all the concerned flux surfaces, such as the off-axis data from Ch1.

Now, examining the Maxwellian fit used by JET, TFTR, and JT-60U to fit their NPA data, several modifications are possible. First, this simple exponential fit can actually provide an estimate of the power deposition density through the Stix parameter. As discussed in chapter 2, the Stix distribution reaches an effective temperature of $T_{\rm lim} = (1+\frac{P_{rf}\tau_s}{3n_m T_e})T_e = (1+\xi)T_e$ at large energies, where P_{rf} is the minority absorbed RF power density, τ_s is the proton slowing down time, and n_m the minority density. Going one step further, the distribution can be fitted with the entire Stix distribution which results in an effective temperature $T_{\rm eff} = \frac{2}{3}\langle E\rangle$ and P_{rf}, the power density. For $\langle E\rangle$, the distribution is integrated up to the energy of the proton with the largest confined orbit; the effect of this limit is not felt until $T_{\rm eff}{\sim}E_{\rm lim}/5$. A complication is that $E_{\rm lim}$ depends on the originating flux surface. For the plasmas in this thesis, the limit is estimated to be greater than 1 MeV for protons at $\sim r = 0$. To be clear, these $T_{\rm eff}$ and P_{rf} values from each channel are again not the flux surface averaged values but represent specific pitch angles from those originating flux surfaces.

Minority distributions from the CNPA vertical and horizontal channels calculated from this minimal model can reveal some details on how resonantly localized and anisotropic the protons are. One simple comparison is to review the on-resonance vertical data (Ch3) with the horizontal channel measurements (Ch4). If the distributions are completely isotropic, the calculated distributions from those channels should be the same since the measurements are weighted by approximately the same flux surfaces. The off-resonance vertical channels are more difficult to interpret since they involve a move off either the plasma axis and/or the resonance layer. These off-

resonance channels theoretically see no signal without collisions and Doppler broadening of the resonance since all the minority ions would otherwise have their banana tips right on the resonance layer. The effects of the broadening and collisions are indicated by the broadness of the 'rabbit ears' and the degree of anisotropy in Figure 3-6. The Doppler broadened resonance is typically several centimeters as indicated in Figure 4-4, and spans the sightlines of the vertical channels for a typical Alcator C-Mod discharge. Assuming that the average temperature over the flux surfaces covered by the three vertical channels are roughly the same, the temperatures inferred from the off-resonance vertical channels using the simple model then is a measure of the effective resonance layer width. Finally, assuming the signal is coming from dominantly one flux surface, an estimate of that flux surface's average T_{eff}, denoted T_{fa}, can be made by using Hammett's 2-D model distribution based on the Stix distribution.

Overall, this modified simple model using the above approximations allows rapid estimates of minority proton temperatures and provides some information about their phase-space anisotropy.

With the general analysis scheme defined, the next section delves into the specifics of the impurity, beam, and neutral models needed to apply it.

4.3 Beam, Neutral, and Impurity Models

In order to apply the simple model on Alcator C-Mod discharges during active and passive CX, a beam and neutral penetration, halo, and impurity density models are needed. They are outlined in the following pages.

Before diving into the details, it will be convenient to make clear the different coordinate systems that are used. Specifically, in addition to the tradition tokamak R-Z toroidal geometry, a beam coordinate system and a field-line system are needed. See Figure 4-5.

4.3.1 Neutral Density and Penetration

For the neutral density, the FRANTIC[43] code in TRANSP is used for passive CX. The code provides flux surface averaged neutral density as a function of minor radius. Figure 4-6 shows one of these profiles for shot 1051206002. The FRANTIC profiles and absolute densities for discharges similar to some of the shots in this thesis have been verified by Rice[44]. During active CX, the beam penetration, beam mix, and source currents are needed to determine the beam neutral density as a function of

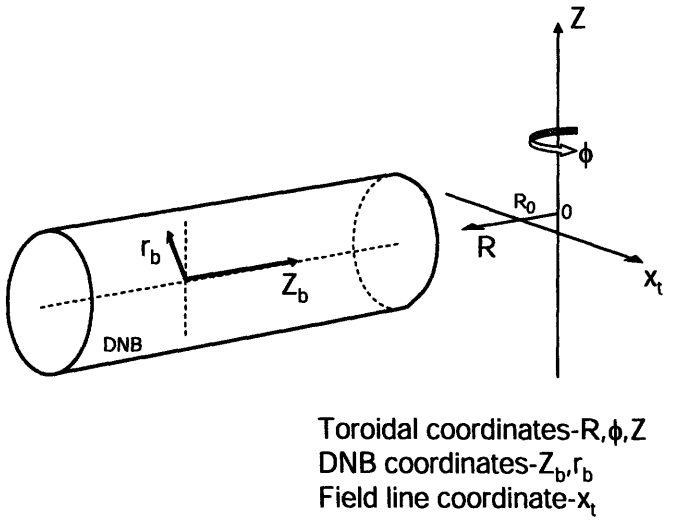

Figure 4-5: Different coordinate systems employed for beam and impurity density calculations. The 'field line' coordinate is essentially the toroidal axis.

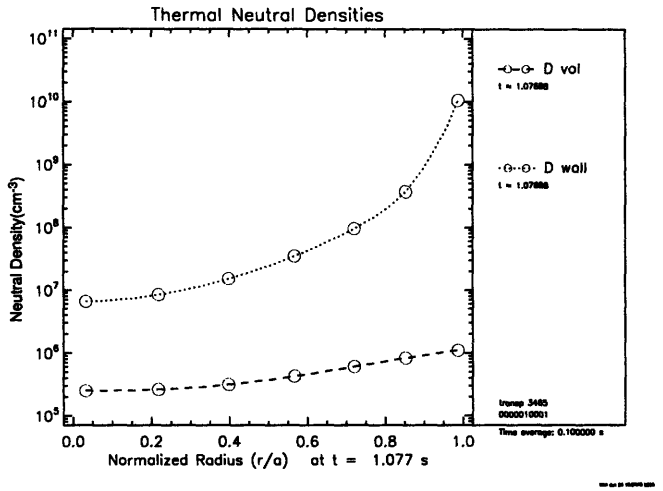

Figure 4-6: FRANTIC 1-D neutral calculation from TRANSP for 1051206002 at t~1-1.15 s. The top curve represents D neutrals from the edge, while the bottom curve gives the local recombination density. The wall source is typically ~2 orders of magnitude higher.

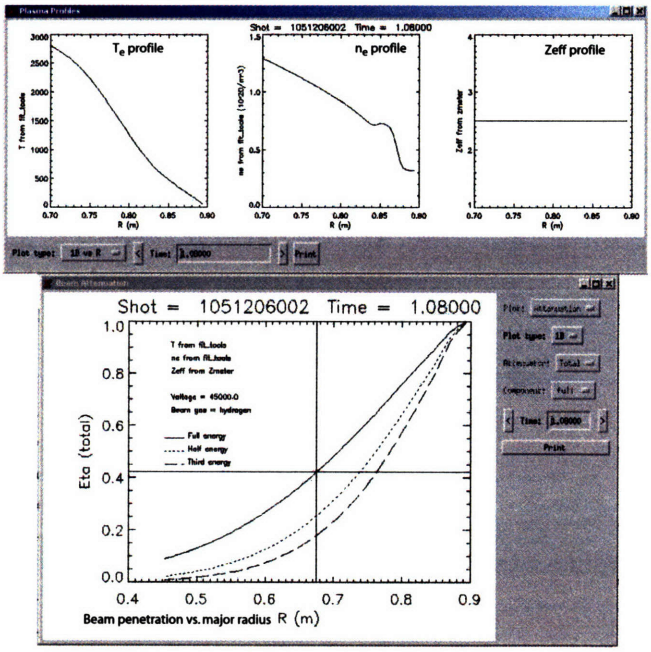

Figure 4-7: Beam penetration results for shot 1051206002 at t=1.08 s from Eisner, Bravenec, and Rowan's IDL program. Janev's neutral stopping cross-sections are used[45].

major radius. The methodology is outlined below. The fast neutral penetration out of the plasma is related to the beam penetration and also discussed.

Both the beam and fast neutral penetration are modeled using Janev's neutral penetration cross-sections[45]. For the beam penetration, an IDL GUI by E. Eisner, R. Bravenec, and W. Rowan is used with fitted density and temperature profiles from Zhurovich's fitting programs. Figure 4-7 gives a sample output from this IDL program for shot 1051206002. For the plasmas in this thesis, the edge neutral pressure is sufficiently low ($\leq$0.02 mtorr) that attenuation of the beam in the F-Port duct should be less than 10% for all components and is hence ignored. In equation form the penetration is:

$$P_b(R,E) = \exp\left(-\int_{R_0+a}^{R} n_e \sigma_s(R,E) dR\right) \tag{4.3}$$

where σ_s is the Janev neutral stopping cross-section as a function of major radius and beam energy. The integral is taken from the edge of the plasma on the mid-plane to the desired major radius.

The initial neutral beam current, $I_n(k)$ is calculated from outputs of R. Granetz's

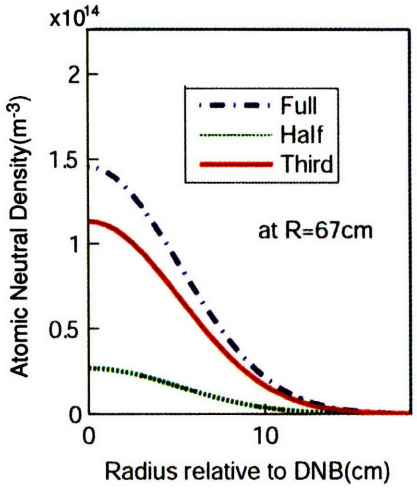

Figure 4-8: Beam profiles at R=67 cm for shot 1051206002. The horizontal axis is r_b

IDL DNB analysis program which determines the source currents via a visible spectrometer observing the neutralization CX for each shot. Mathematically:

$$I_n(k) = I_s I_f(k) H(k) N_f(k) \tag{4.4}$$

where I_s is the total source current in amps, I_f the fraction of the total source current for full, half, and third components, H is the number of H neutrals for each component, namely 1, 2, and 3.4, and N_f is the steady-state neutralization fraction for each beam component. k is clearly an index for the full, half, and third energy components of the beam.

As for the beam spatial profiles, measurements on the inner wall during no plasma shots indicate that the FWHM of the beam is ~12 cm, leading to profiles as shown in Figure 4-8 at R=67 cm. These beam parameters at R=67 cm are used for all the vertical channels' calculations and represent some averaged penetration from R=65-70 cm. Janev's cross sections are separately employed for the calculation of $P(E)$. Figure 4-9 illustrates the neutral penetration from the center of the plasma as a function of energy for the vertical and horizontal channels during the flattop of shot 1051206002. For the CNPA signal, attenuation due to residue neutral pressure is included since the detectors are as far as ~3 m away from the plasma edge. This is typically a 10-15% effect at 50 keV for the plasmas in this thesis. Averaged Thomson

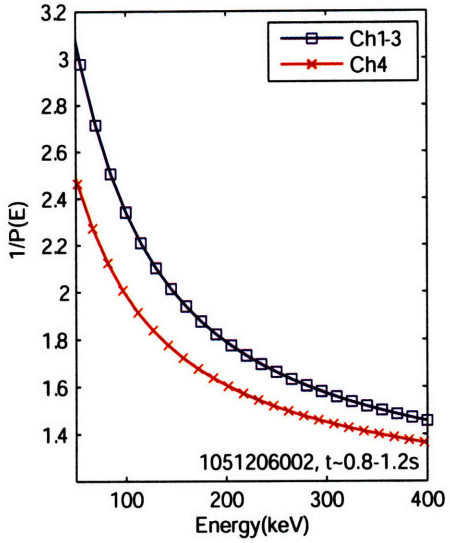

Figure 4-9: Inverse neutral penetration from the center of the plasmas to Ch1-4 for shot 1051206002 during plasma flattop. The attenuation for Ch4 is smaller since there is less plasma to travel through on the mid-plane, and also because the port length is shorter.

scattering based plasma parameters are used for the calculation, giving:

$$P(E) = \exp(-\overline{n_e}\sigma_s(\overline{n_e}, \overline{T_e}, \overline{Z_{\text{eff}}}, E)\Delta X_p - n_n\sigma_{ii}(E)\Delta X_d) \tag{4.5}$$

where ΔX_p is the distance from the center to the edge of the plasma and ΔX_d is the distance from the edge of the plasma to the detector itself where attenuation due to residue neutral gas can occur. n_n is the neutral gas density in the duct and determined from the E-top and G-side neutral pressure gauges. The dominant attenuation process outside of the plasma is neutral impact ionization, given by σ_{ii}.

For the vertical sightlines, the attenuation is assumed to be the same for all three channels. Detailed analysis shows that using averaged plasma parameters for the penetration calculation and neglecting bulk plasma profile details result in negligible errors for the minority distributions in this thesis. The error bars induced on T_{eff} from errors in the penetration profile are estimated to be less than 5%. This analysis can be found in Appendix B.

4.3.2 Halo Model

With the beam source defined, the halo profile and density at R=67 cm can be determined. Halo neutrals stem from neutralization of bulk deuterium ions due to CX with the beam. Once created, these halo neutrals can CX again with another bulk ion and hence they participle in pseudo-random walk diffusion from the originating beam source. A relatively simple 1-D model in cylindrical coordinates is implemented with the different beam components as sources for this problem. Defining the cylindrical coordinate's Z-axis along the beam (i.e. Z_b), the halo density as a function of r_b is then determined using averaged core (r/a=0 to 0.5) plasma parameters. The steady-state rate balance is:

$$D_{n_0}\frac{\partial}{r_b\partial r_b}(r_b\frac{\partial n_0}{\partial r_b}) = n_0\beta - \sum_{k=1}^{3}\alpha_k(r_b) \tag{4.6}$$

where $\alpha_k(r_b) = n_i n_{b,k}(r_b)\langle\sigma v\rangle_{cx,k}$, with n_i corresponding to the given D ion density, $n_{b,k}(r_b)$ the density of the k^{th} component of the DNB, and $\langle\sigma v\rangle_{cx,k}$ the CX rate. $\beta = n_e\langle\sigma v\rangle_{ei}$ is the electron impact ionization rate per D neutral. The leftmost term corresponds to D halo neutral losses from transport, modeled through a diffusion coefficient based on CX of these D neutrals with bulk plasma ions. The diffusion coefficient is $D_{n_0} = k_b T_i/m_d\nu_{cx}$. ν_{cx} here is estimated by $n_i\sigma_{cx}(v_{D,mp})v_{D,mp}$, where $v_{D,mp}$ is the most probable speed of the bulk D ions based on their temperature. This number typically is slightly lower than the true average rate in the ~1-2 keV range. Recombination and D ion impact ionization are negligible compared with the birth and loss rates considered above. Deuterium halo neutral losses through impurity ionization collisions or impurity CX are not included in this simple halo analysis but they should be at best a ~10% effect. Lastly, at densities around $10^{20}/\mathrm{m}^3$, less than ~1% of the DNB is in the n_p=2 state and hence excited DNB neutrals should not significantly affected the rate balance[38]. At most the total beam-bulk plasma CX reactivity would increase by ~5%. These two small neglected effects might also somewhat counterbalance each other. Lastly, the steady-state assumption is good since equilibrium is expected in the less than ~1 ms time frame.

The r_b in this cylindrical coordinate translated back to the tokamak and field-line geometry correspond to both Z and x_t, where x_t is approximately the central field line. This means that for the active and passive CX comparison, the beam and halo parameters for a particular Z corresponds directly to r_b in the model. Equation 4.6 is solved with modified bessel functions. This model gives a characteristic halo profile shown in Figure 4-10 for shot 1051206002. The exact details of the model,

including the full derivation and sensitivity to input plasma parameters, can be found in Appendix C.

These halo density estimates are reviewed with TRANSP based calculations and found to be comparable. The TRANSP based simulations are based on using the FRANTIC code with source terms determined from a 3-D Monte-Carlo beam model. Because of its nature, the TRANSP output is flux averaged and inappropriate for direct application here.

4.3.3 Hydrogen-like Impurity Model

With all the neutral sources calculated, the density and profiles of the relevant HL impurities can be estimated. For the concerned energy range, the two pertinent impurities are helium and boron. Although helium is not normally found in D(H) Alcator C-Mod discharges, it can be puffed in for various diagnostic purposes. This is done for some of the discharges studied in this thesis. As for boron, it is typically the dominant low Z impurity in Alcator C-Mod plasmas[46, 47, 48] and can affect the CNPA data in the energy range >200 keV. For both of these impurities, their effect in the dominator of equation 4.2 can be quite different between active and passive CX.

For passive CX, the core HL density for a specific impurity is approximately determined by the steady-state rate balance:

$$n_{imp,HL}\left(n_e\left\langle\sigma v\right\rangle_e + n_p\left\langle\sigma v\right\rangle_{cx}\right) = n_{imp}\left(n_e\left\langle\sigma v\right\rangle_R + n_{0,D}\left\langle\sigma v\right\rangle_{cx}\right) \tag{4.7}$$

where $n_{imp,HL}$ is the density of hydrogen-like impurity, n_{imp} the density of the fully stripped impurity, n_p the density of fast minority protons, and $n_{0,D}$ the background D neutral density. The rate brackets on the left are destructive and represent electron impact ionization and CX with the fast ions. The electron impact ionization term is dominant but CX with the fast ions can be significant for HL helium in the T_p ~50-100 keV range of concern. Luckily, this term is typically just ~10-15% of the total and the input fast proton temperature for the CX rate can be just estimated apriori without affecting the total destruction term significantly. If this is not the case, some iteration of the model would be required since $n_{imp,HL}$ is part of the formula for getting the fast ion temperature. On the right are the birth terms for the HL impurity ions and are composed of recombination and CX from background D neutrals. In most cases, recombination dominates. For the analysis here, averaged core plasma parameters(r/a=0-0.5) are again used for the inputs. Excited states are

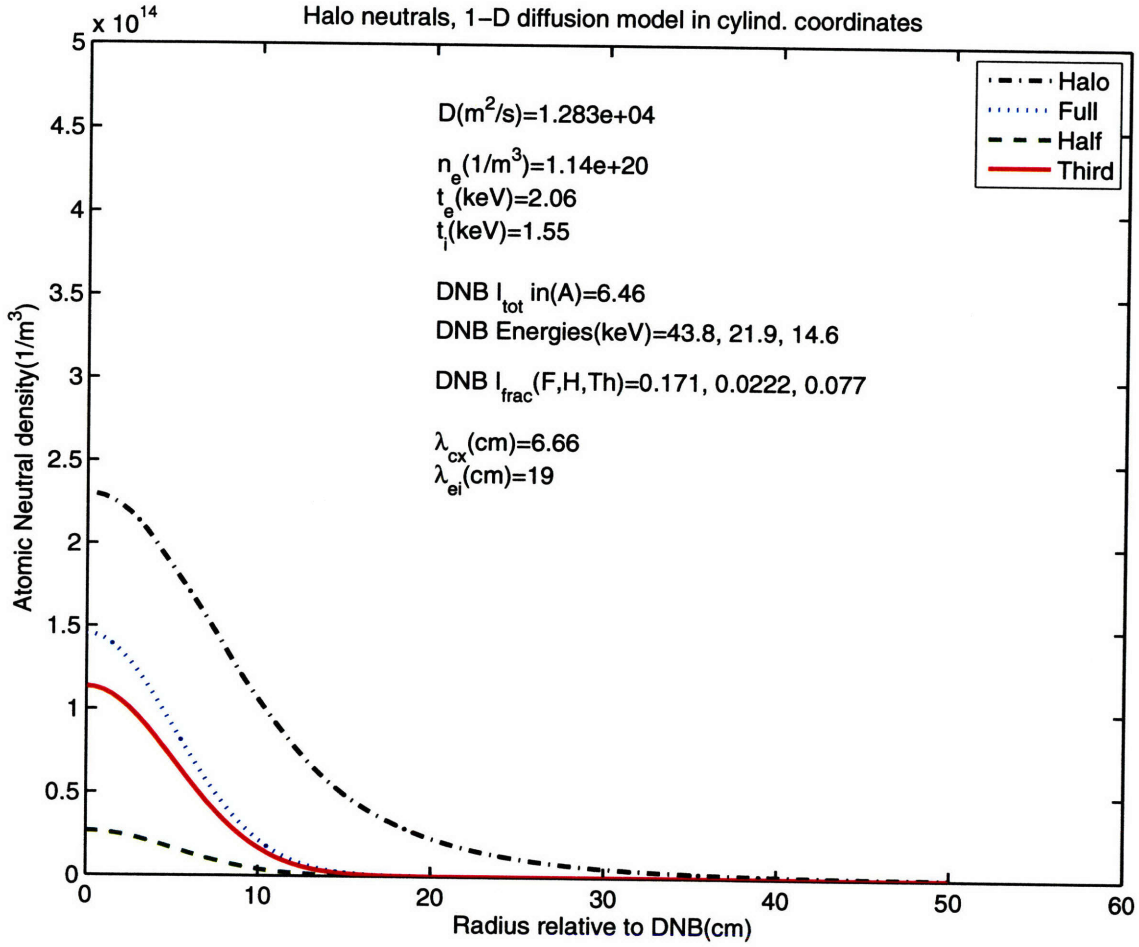

Figure 4-10: Halo and beam density profiles for 1051206002 at t=1-1.15 s. The bulk D ion temperature is estimated from the neutron data.

again neglected. Lastly, equilibrium is expected in the ~1 ms time frame.

Before moving on to the impurity model for active CX, an aside is needed to discuss the experimental data used for the n_{imp} inputs in equation 4.7.

Pertaining to the fully stripped helium density, no direct spectroscopic measurement of it is available for the core. However, a line-integrated measurement of the He-II line is available via a diode mounted on the Alcator C-Mod McPherson XUV diagnostic[49]. On another note, for D(He^3) plasmas, the helium density can be and is typically estimated by RF break-in-slope analysis[50]. By combining these two data, a new method of estimating the core helium density is implemented for this thesis. Namely, the diode is calibrated with the RF break-in-slope helium density estimates; a CX dominated scaling is found to reconcile the data in the calibration. Full details of this work can be found in Appendix D. For the purposes here, this diode can provide rough estimates of n_{He}/n_e for equation 4.7 during LSN and USN discharges.

Various methods are available to estimate the boron density. An edge technique involving D gas puffing and the CHROMEX diagnostic found levels typically in the ~1% range, and higher levels after boronization [46, 47]. In theory, the CXRS diagnostic with active CX can give an accurate boron density in the center of the plasma. For the shots in this thesis, these data are available. However, because the CXRS system is not and will not be absolutely calibrated within the foreseeable future, the absolute densities are not derivable. In other words the étendue is unknown. Attempts to calibrate the system with the visible bremsstrahlung background in the spectra are inconclusive since the boron densities estimated from an étendue calculated based on this background give n_B/n_e=0.01-0.1%, which are probably too low to be correct. Fortuitously, as shown in the next several sections, the effective temperatures derived from the active CX CNPA data are not very sensitive to the boron density, even though the shape of the inferred minority distribution at energies greater than 200 keV is. Skipping ahead a bit, for some scenarios, the CNPA can actually serve as a boron impurity density diagnostic. Typically for the discharges discussed later, the boron densities with decent fits are around 1.5-2%. Because the core Mo density is calculated for some of these shots using the XUV diagnostic, some collaborative evidence is available to indirectly support this percentage since the core Z_{eff} data are also available.

To note, the relative concentrations of the boron and helium densities for the discharges in this thesis can be estimated from the available spectroscopic data even if the étendue for these spectroscopic systems are not available.

With the input question settled, the active CX impurity model for the core is now given. The impurity creation process during active CX is more complicated than in the passive case because the source terms from the beam are not axi-symmetric. Specifically, most of the HL impurity ions during active CX originate from the beam. Neglecting radial transport, these HL impurity ions are free to stream along their field-lines until destroyed either by electron impact ionization or CX. The simplest case occurs when the HL impurity ions' mean-free path is greater than $\sim 2\pi R_0$, or the length of the central field line for one toroidal transit. Then, the effect of an toroidally asymmetric birth term is smeared out and the core active CX induced impurity density balance is approximately:

$$n_{imp,HL}\left(n_e\left\langle\sigma v\right\rangle_e + n_p\left\langle\sigma v\right\rangle_{cx}\right)\Delta V_{tor} = n_{imp}\sum_{k=1}^{4} n_{b,k}\left\langle\sigma v\right\rangle_{cx,k}\Delta V_{beam} \tag{4.8}$$

where now the birth terms on the right are from the beam. The '4th' component represents some average of the halo neutrals. ΔV_{tor} refers to the flux tube volume at the core of the plasma, and ΔV_{beam} refers to the intersection volume between the DNB and that flux volume. If the passive data is not background subtracted out, the recombination and D neutral CX terms should be added to the right hand side.

As it turns out, the boron impurity typically does satisfy the $\sim 2\pi R_0$ requirement, but helium does not. In the end, a much more detailed semi-analytic model is used for this thesis work. A new 1-D field line model with boundary conditions that account for ion recirculation is applied. In particular, the analytic solution for a thin HL impurity strip source with recirculation is derived and used to numerically integrate the Gaussian beam source profiles from the previous section. The very thin 1-D strip source with recirculating boundary conditions shown in Figure 4-11 has the following impurity density solution:

$$\begin{aligned} n_{imp,HL} &= \frac{a\alpha}{v}\left[\frac{2}{1-\gamma}\cosh\left(\frac{\beta}{v}(x_t-b)\right) - e^{\frac{\beta}{v}(|x_t-b|)}\right] \\ \alpha(x_t,k) &= n_{imp}\sum_{k=1}^{4} n_{b,k}\left\langle\sigma v\right\rangle_{cx,k} \\ \beta &= n_e\left\langle\sigma v\right\rangle_e \\ \gamma &= e^{\frac{\beta 2\pi R_0}{v}} \end{aligned} \tag{4.9}$$

where a and b are as shown in the figure, and v is the thermal velocity of the HL impurity, approximately equal to $v_{D,mp}/\sqrt{m_{imp}/m_D}$. The formula is constructed out

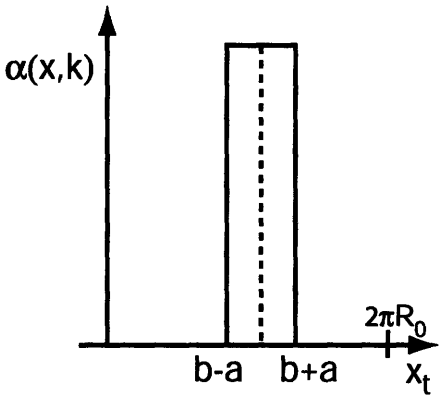

Figure 4-11: The 1-D strip source with solution given by equation 4.9.

of the solution for a thin 1-D strip source with no recirculation, specifically $n_{imp,HL} = \frac{1}{2} n_{imp,HL}(x_t = 0) e^{-\beta |x_t|/v}$. This stems from the solution of $\partial n / \partial x = -n\beta/v$.

The final results of the active CX impurity model are illustrated in Figures 4-12 and 4-13 for both boron and helium impurities in shot 1051206002 assuming averaged core plasma parameters. The boron figure clearly shows a very flat profile along the field-line and validates the simple estimate from equation 4.8. On the other hand, the helium figure demonstrates the need for the more detailed 1-D field-line model.

Examining the active impurity model in terms of its role for interpreting CNPA data, the HL impurity density used in equation 4.2 is the $x_t = 0$ value in Figures 4-12 and 4-13. This is approximately correct given averaged core plasma parameters inputs, as long as the fast ions are not dramatically far away from $Z = 0$.

4.4 Sample shots: 1051206002 and 1051206005

In the last several sections, the electron donor terms as a function of Z for shot 1051206002 were determined for illustrative purposes. In essence the densities in the denominator of equation 4.2, or the CX factors, has been calculated for a set of input parameters. Now, this section shows in detail how the rest of the model calculates effective temperatures for each channel, and infer the approximate Z_p(or r/a, when re-mapped) of the peak minority temperature. The sensitivity of the temperatures and hence the method to different input parameters are also tested.

The key to a good temperature and Z_p analysis from this model is the insensitivity of the inferred fast ion temperature from active CX when helium is not present. This results from the fact that for low density Alcator C-Mod plasmas, the dominant

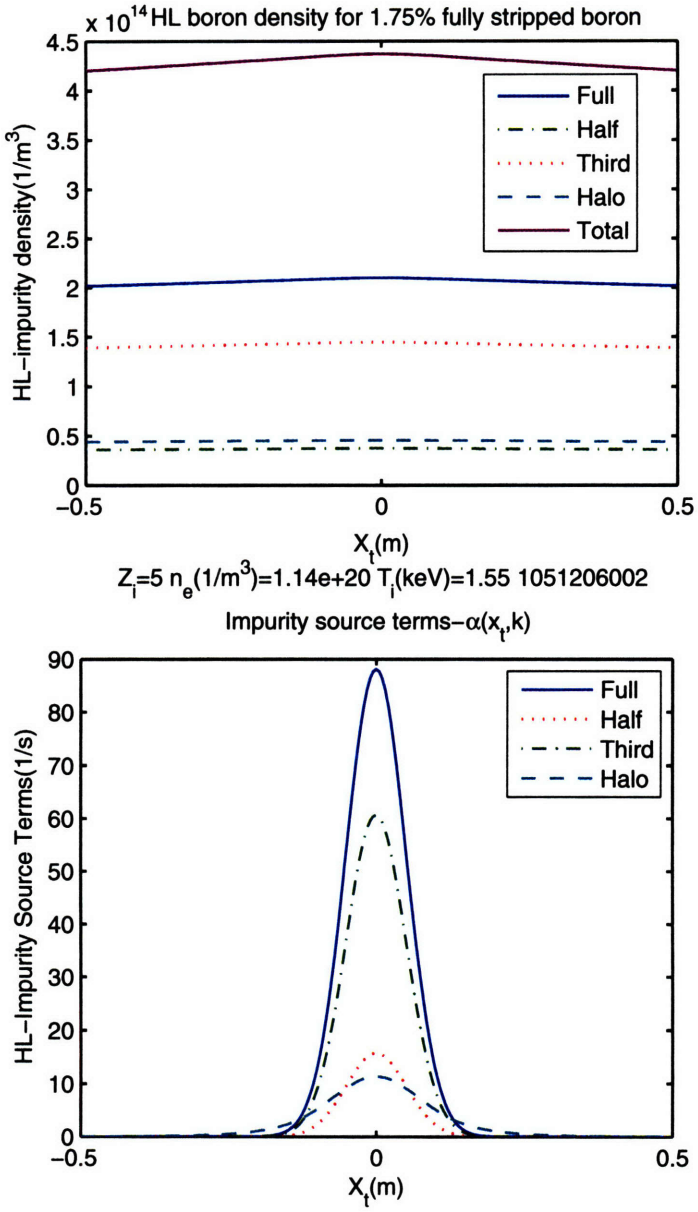

Figure 4-12: Top: 1-D field-line profiles of the HL boron density for shot 1051206002 assuming a 1.75% n_e fully stripped boron density. The density is essentially axi-symmetric. The contribution from each beam component is shown, along with the total. Bottom: The beam and halo HL boron impurity source terms.

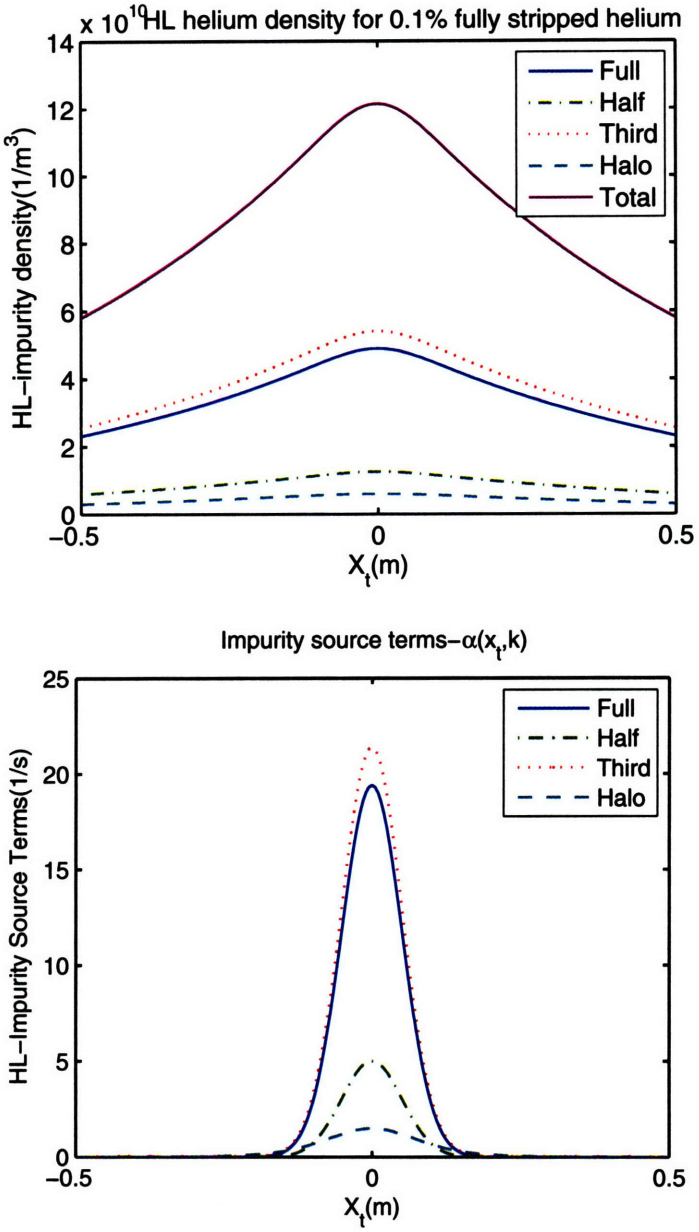

Figure 4-13: Top: 1-D field-line profiles of the HL helium density for shot 1051206002 assuming a 0.1% n_e fully stripped helium density; the 0.1% assumption is for illustrative purposes only, since no helium puffing is used for this shot. The profiles are not axi-symmetric. The contribution from each beam component is shown, along with the total. Bottom: The beam and halo HL helium impurity source terms.

neutralization below 200 keV comes from halos and the third energy component of the DNB. This means that for the range of Z (0-10 cm) where the fast ions are expected to be, the active CX factor does not change significantly. Additionally, since the number of counts in each energy bin decreases relatively fast with increasing energy, any weighted temperature fit of the inferred minority distribution is dominated by CX below ~200 keV. Hence, the temperature fit itself is not sensitive to the boron dominant CX region of ~ 250 keV and therefore the exact boron density. As stated above, for some scenarios, it is possible to infer a boron concentration from these temperature fits and use the CNPA as a core boron diagnostic, assuming the model distribution used to fit the data is approximately correct. This is also the reason for the earlier stated limit of $T_p \sim 120 - 130$ keV for the model's ability to find the peak fast ion temperature. On the other hand, during passive CX, the boron becomes significant at a much lower temperature, typically around ~ 150 keV. Thus, passive only analysis can be very difficult, as accurate boron and background thermal neutral densities are needed.

When significant helium is present, it can be an important electron provider during active CX. However, unlike the boron, it does not seem to affect passive CX until a very large amount is present. Fortunately, a measurement of this impurity is available via the calibrated HeII diode mentioned above.

The optimum model result occurs when for a given set of known input parameters the passive and active CX analysis match in terms of both temperature and predicted count rates.

To illustrate these points, a sample case, shot 1051206002, is first examined. As a reminder, the bulk plasma parameters and raw CNPA data for this shot can be found in Figures 3-12 and 3-13. This shot is assumed to have no helium in it, since no puffing occurred in the shots before it and the baseline on the HeII diode is close to another shot with similar plasma parameters that occurred right after machine startup. Shot 1051206002 is representative of the typical discharge in this thesis; it does not reach the 'perfect' analysis discussed in the last paragraph but is still viable.

From the raw data shown in Figure 3-13, assuming a 1.75% boron impurity, Z_p=7 cm, D neutral density of $\sim 1.3 \times 10^{13}/\mathrm{m}^3$, and using the profiles derived in the previous sections, the analysis results are summarized in Figures 4-14 and 4-15.

First, Figure 4-14 plots the different CX factors of equation 4.2 for active and passive CX. The halo and third component of the beam dominates the active CX factor until about 200 keV, when HL boron CX starts to become important. For the passive CX factor, the boron clearly becomes important much earlier, around

120 keV. The count rates for active and passive CX are also compared and matches the model prediction well for Z_p=7 cm. For the work in this thesis, the aim is to chose a Z_p that makes a match for Ch2, the mid-channel of the vertical array. This results in approximate matches for Ch1 and Ch3.

Next, Figure 4-15 shows the minority distributions and assorted temperature fits from these CX factors. The data from two different time periods are shown. The first, t1, corresponds to t=1-1.15 s in the shot when the DNB fired. The second, t2, corresponds to counts from t=0.8-1 s and t=1.15-1.2 s, representing the passive data that bracket the beam period. For Ch4, the data is all passive and the two spectra are just passive CX based distributions from the mentioned time ranges. The first two temperatures listed in the legend for each channel are for t1. The top one is a simple weighted exponential fit of the t1 distributions, followed by a weighted Stix distribution fit and the RF power density associated with that fit. The last fit is an un-weighted Stix distribution fit of the passive, or t2 spectra. These fits are not weighted because the passive data tends to have some oscillations in them, making automated weighted fits very unreliable. For example, a weighted fit of the passive spectra for Ch2 results in a temperature that is unrealistically high, since the fit is heavily affected by the 100-150 keV points where a negative distribution slope occurs. Concerning Ch4, only the t2 data is used for the later scaling analysis because the t1 data has potential contributions from HL impurities streaming from the beam volume that is not accounted for in the passive analysis. As expected, the Ch4 temperature is lower than the vertical channels. This validates that indeed the distribution is anisotropic and that the peak temperatures are at the resonant pitch angles of Ch2 and Ch3.

With the results shown for 1051206002, it is now appropriate to discuss how the two model input parameters are determined. Specifically the boron input and the Z_p location are relatively unconstrained by other plasma measurements and must be inferred through the CNPA data itself.

For the boron, the XUV analysis shows that Mo makes up about 0.2 of $Z_{\text{eff}} - 1$ in these types of LSN shots. The core (r/a=0-0.5) Z_{eff} for this shot is estimated to be ~1.5-1.75; the average Z_{eff} from the Z-meter is 2.5. This leaves ample room for a $\sim$ 1% boron impurity, which would contribute ~0.2 also to $Z_{\text{eff}} - 1$. However, as hinted at before, even if this rough estimate is not available, it can be inferred from the CNPA data. In particular, Figure 4-16 shows the 1051206002 analysis with boron set to 0.1%. The active CX data and their associated weighted fits are hardly affected; however, the inferred passive spectra and their temperature fits are

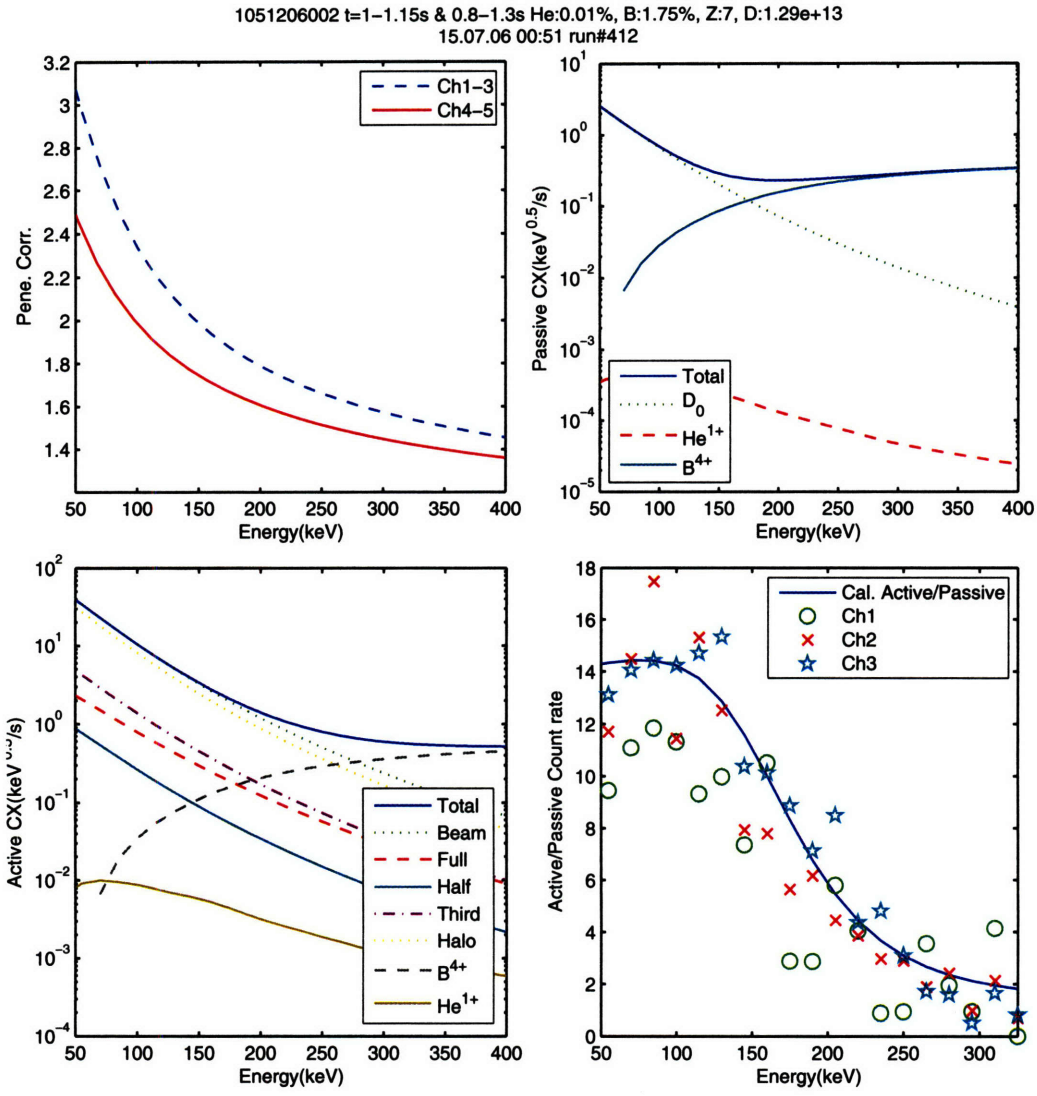

Figure 4-14: Summary of charge-exchange parameters for the base 1051206002 analysis. Top left: 1/P(E). Top right and bottom left: Passive and active CX factors. These are the denominators from equation 4.2. The beam, specifically the halo and third component, is clearly dominating the CX during active CX. Bottom right: The active/passive count rate ratio for Ch1-3. The model calculation is the total CX factors from the active and passive CX plots divided by each other.

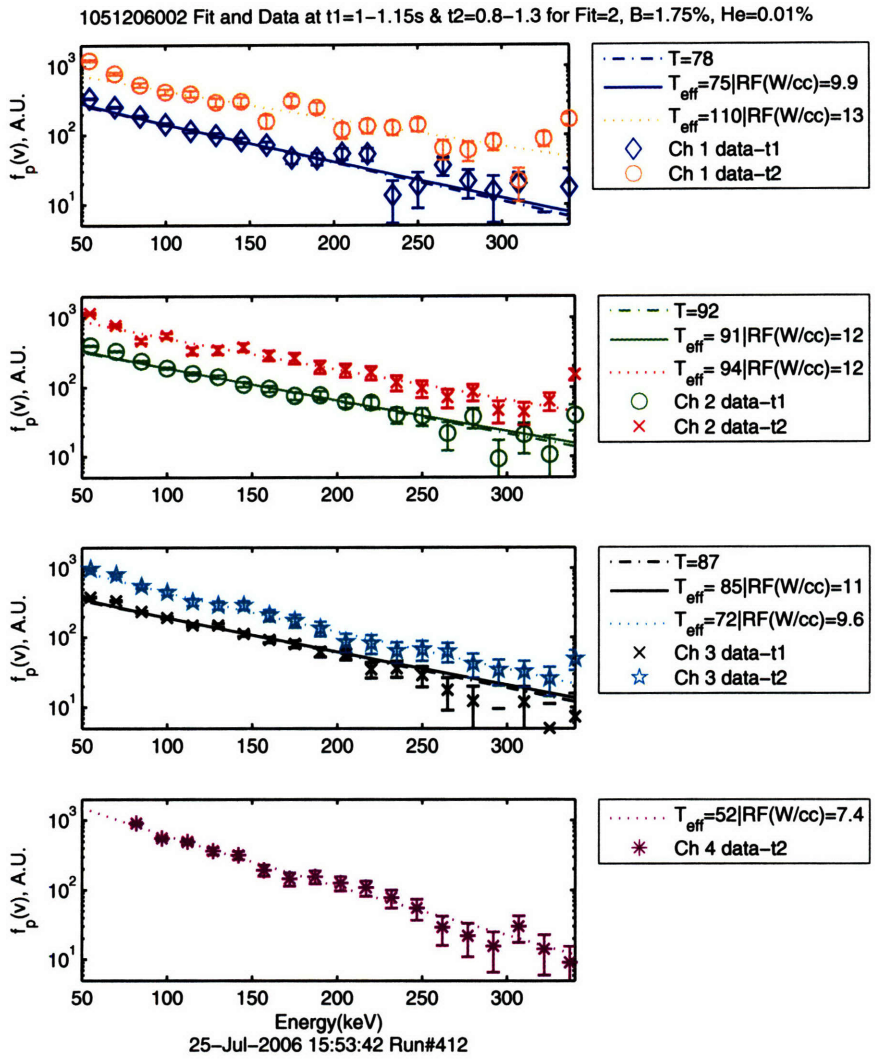

Figure 4-15: Passive and active CX inferred minority distributions, $f_p(v)$, and temperature fits for the default 1051206002 analysis. The error bars include counting statistics only. t1=1-1.15 s corresponds to the active data, and t2 represents the passive data taken between t=0.8-1.0 s and 1.15-1.3 s. The Ch4 data is passive only for each time period. For each channel, the weighted temperature fits for the t1 data using both a simple exponential and a Stix distribution fit from 100-320 keV. These are the first two temperatures on each legend. The RF power for the Stix distribution fit is also listed. The third temperature in the legend is a non-weighted Stix distribution fit for the t2 (i.e. passive CX for Ch1-3) data. The data in the last bin, 340 keV, is not used because that energy bin tends to have abnormally high counts because of the voltage rail on the amplifiers.

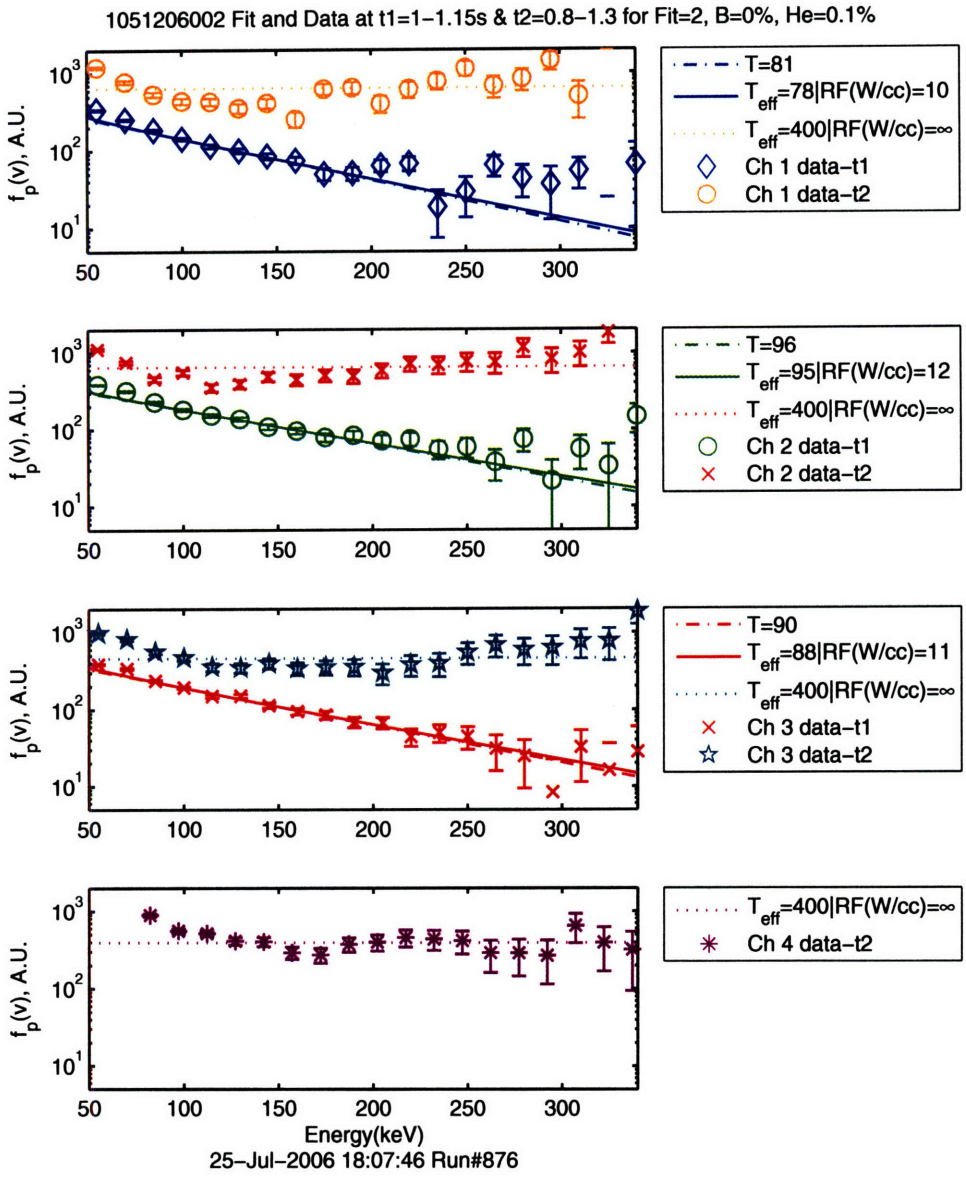

Figure 4-16: Passive and active CX inferred minority spectra and temperature fits for shot 1051206002 assuming a 0.1% boron density. Compared with Figure 4-15, the active CX data and temperature fits are not very much affected by using a lower boron density. However, the passive CX inferred distributions are drastically different and unrealistic. The T_{eff} is limited to 400 keV because a confined orbit limit of 1 MeV is imposed.

completely wrong, revealing the passive analysis' sensitivity to the exact HL boron densities. On closer examination, the minority distributions from the active CX data in the range >200 keV are affected by this decrease in boron. Specifically, there is a rise in the inferred distribution since the assumed active CX factor at these higher energies is now lower than before (remember that the raw data is divided by this factor to get the minority distribution). However, again, the weighted temperature fits are not affected by this because the number of counts and therefore statistical weighting are always dominated by the lower beam-CX only energy bins. Hence, assuming that the model distributions used to fit the data is correct, a boron density can be estimated from the CNPA data by using a boron input in the model that both reconcile the passive CX deduced temperatures to the active derived ones and forces the high energy portion of the active CX distribution closer to the temperature fits. Typically the effort is concentrated on reconciling the data sets from Ch2 and Ch3, since these channels are either on or closest to the plasma and resonance axis, where the model is overall more valid. Also, as can be seen for the data in Ch1, significant regions of 'negative' temperatures can arise at high energies even for the active CX data with reasonable boron densities in the model. These anomalies off-axis are probably due to orbit effects. Again, if only temperature data is needed from Ch1-3, the boron does not matter until so much is in the plasma that even the normally beam dominated CX regions of the spectra are affected by it. For temperature data from the passive CX only Ch4, the boron density used in the model is important, and the error bars on this measurement should reflect this. To conclude, a 1.75% boron impurity is used for this shot given all these considerations. Error bars for the active CX fitted temperatures are estimated by varying the input parameters within a reasonable range and examining the resultant fits. For this discharge, the approximate error for Ch1 based on this method is +10/-5 keV, ±5 keV for Ch2 and Ch3, and the Ch4 T_{eff} is estimated to have errors of ±10 keV. It should be noted that these are only estimates and that the real error could be larger, as this is not a fully formal approach. For example, the goodness of the fits for each variation in input parameter is not compared directly and only the differences in temperature are reviewed.

Now, returning to the second input parameter, Z_p, Figures 4-17 and 4-18 shows what happens if the signal is assumed to come from Z=0, or r/a=0 instead of Z_p=7 cm. The D neutral background is now lowered to $\sim 6 \times 10^{12}/\text{m}^3$ according to Figure 4-6, while the effective beam neutral densities increases according to Figure 4-10. The active CX temperatures again are not much affected because the active

CX is still dominated by the third component of the beam and the beam halos. On the other hand, the passive CX temperatures are affected because with the lowered D neutral density, boron CX becomes important even earlier in the passive CX factor. The key point though is that now the count rates between the active and passive CX data do not match at all. If the signal is really dominantly at near r/a=0, the count rates during active CX should be much higher at the beam dominated CX energies for the on-axis Ch2 and Ch3. Generally, the active-to-passive CX ratio increases rapidly with decreasing Z, since the beam based neutral densities increases with decreasing Z while the background thermal neutral density decreases with decreasing Z.

Experimentally, if the CNPA sightlines are missing the center of the DNB in the toroidal direction, the active CX signal can be less than expected. Also, if the beam neutralizer is less efficient than assumed, the signal would also be lower. However, the tilt in the CNPA sightlines are estimated to be less than 1.5 cm at the mid-plane based on tilt measurements of the diagnostic, and there is no evidence that the beam neutralizer does not reach steady-state. Additionally, estimates show that the neutral current would have to be halved before a Z_p=0 input in the analysis would work. Hence the inferred off-axis location of ~7 cm for the fast ions is good. Given the above points, the error in this measurement is probably $\sim \pm 2$ cm. More supporting evidence for this off-axis location consists of r/a=0 fast ion temperature estimates from sawteeth reheat analysis and the ASORA/CQL3D FW/FP solver simulations discussed in the next several sections.

Before moving on to the next topic, a sample shot with a helium puff is discussed. The goal of the helium puff is to illustrate the effect of a known impurity on the CX factors when used on a known or repeated shot. Figures 4-19 and 4-20 show the analysis for shot 1051206005. This shot is similar to shot 1051206002 except helium is puffed in at t=0.3 s; the HeII diode measures ~1% He during the plasma flattop. The line-integrated density is slightly lower, going from $4.8 \times 10^{19}/\mathrm{m}^2$ to $4.4 \times 10^{19}/\mathrm{m}^2$. The H/D ratio is also slightly lower, from ~8% to ~7%. A Z_p ~8 cm is found from the count rates comparison. It should be noted that the plasmas with He puffs tend to have slightly larger Z_p, and this could be due to a higher passive CX rate than calculated, since neutral helium penetration and CX is not accounted for in the model. The passive and active CX temperatures match better compared with the 1051206002 case; the passive CX temperatures are higher though. However, it is found that an assumed 0.75% He brings the Channel 3 temperatures closer, since the effect of helium on the active CX spectra is to lower the temperature fits. Given the inexactness of the HeII diode measurement, 0.75% He is also a reasonable assumption.

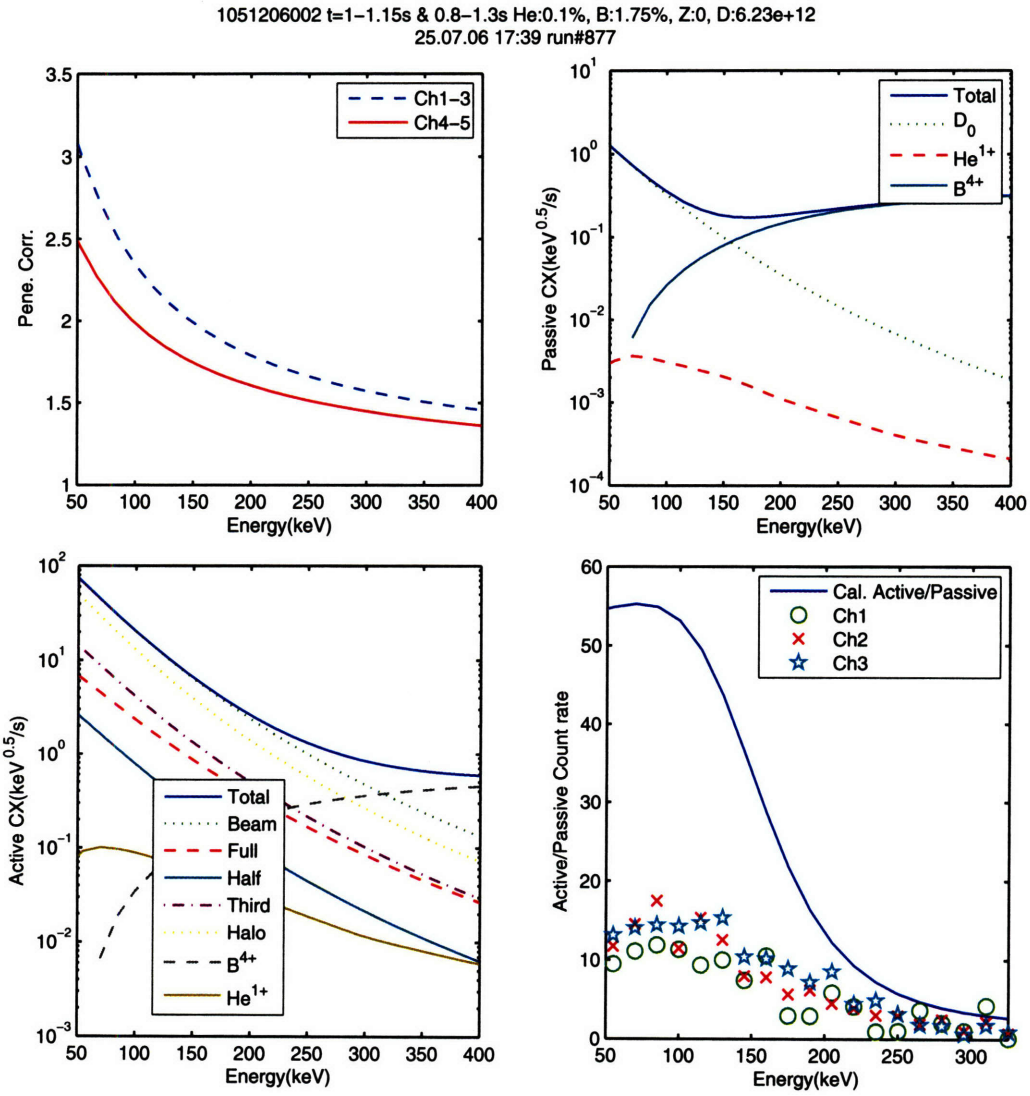

Figure 4-17: Summary of charge-exchange parameters for 1051206002 analysis assuming Z_p=0, or r/a=0. Clearly, the active-to-passive count rate mis-match shows the poor choice of Z_p.

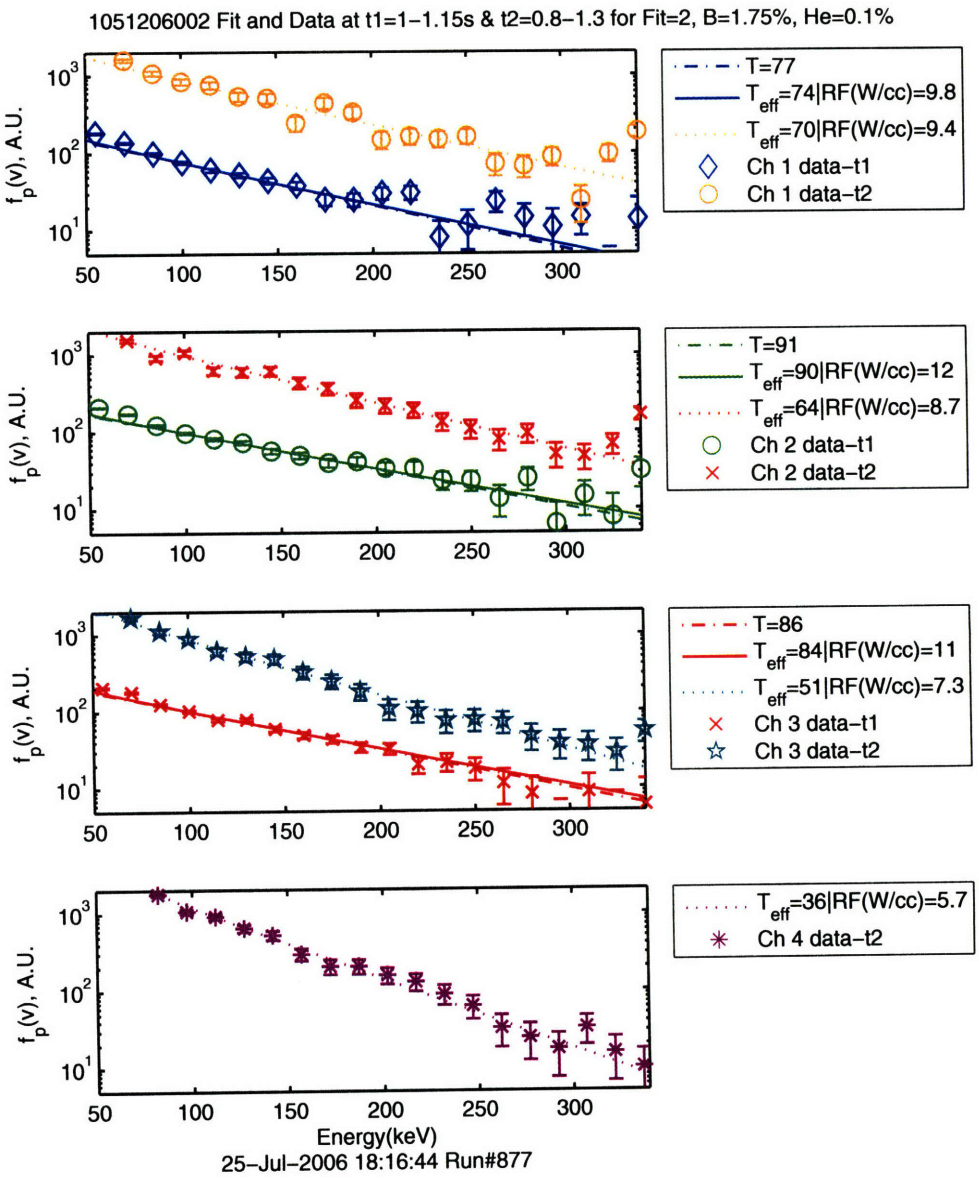

Figure 4-18: Passive and Active CX inferred minority distribution, $f_p(v)$, and temperature fits for 1051206002 analysis assuming Z_p=0, or r/a=0. The active CX temperatures are not affected by the change in Z, but the passive CX temperatures are because of the decrease in assumed D neutral density.

Hence, the error bars for the active CX temperatures are larger for plasmas with He, either puffed in or from the wall.

Lastly, with the inferred temperatures above, the flux surface averaged temperature for the Z_p flux surface can be estimated. This is done by fitting the temperatures to the Hammett 2-D model distribution. As discussed in Chapter 2, this model gives a fast minority ion distribution as a function of $v_\parallel/v$ at the mid-plane and E for an input mid-plane averaged RF absorbed power density and bulk plasma parameters. By finding the effective temperature for each mid-plane pitch angle and re-mapping the results back to the major radius using $v_{\parallel,\mathrm{mid}}/v = \sqrt{(1 - R_{\mathrm{tip}}/R_{\mathrm{mid}})}$, where R_{tip} is the R of the detector and $R_{\mathrm{mid}} \sim Z_p$, the fitted CNPA temperatures can be compared with the model for different input power densities. The flux surface averaged T_{eff}, denoted T_{fa}, can then be found by using the resultant mid-plane distribution with equation 51 from Catto[28]. These flux surface averaged temperatures are found to be very close or equivalent to the mid-plane pitch-angle averaged values. Figure 4-21 illustrates this process and the results for shot 1051206002. A T_{fa} of 65±10 keV is estimated for the Z_p ~7 cm flux surface, or r/a ~0.3. Note that this method should only be used a guide, since as Hammett states, this distribution is only a model and has not been specifically derived from the Quasi-linear RF Fokker-Planck equation. However, these estimates can be helpful for comparisons with codes that only output flux surface averaged temperature and power densities, such as TRANSP.

Summarizing, the modified simple model can provide useful fast proton temperature, RF power density, and some fast proton spatial information for low density Alcator C-Mod discharges when good DNB data is available. The model works well when the relevant impurities can be estimated or inferred through the CNPA data itself, and best when they are at a low absolute level. The model should start to break down when the fast ions are too energetic and when the fast ion profile is spatially wide. These characteristics invalidate the assumption that most of the signal is coming from a specific flux surface and that peak temperatures are measured. Again, when the distribution is too energetic, the energy space where the temperature fits are performed are no long near or greater than the real temperature; the distribution in this energy space is hence no longer dominated by the peak fast proton temperature. However, if the fast proton temperature profile is more like a step function spatially, then this is less of a concern. In any case only a detailed synthetic diagnostic can account for theses types of differences.

With the CNPA analysis method defined, the next section reviews how the r/a=0 fast proton temperature is estimated using a dW/dt sawteeth analysis. This permits

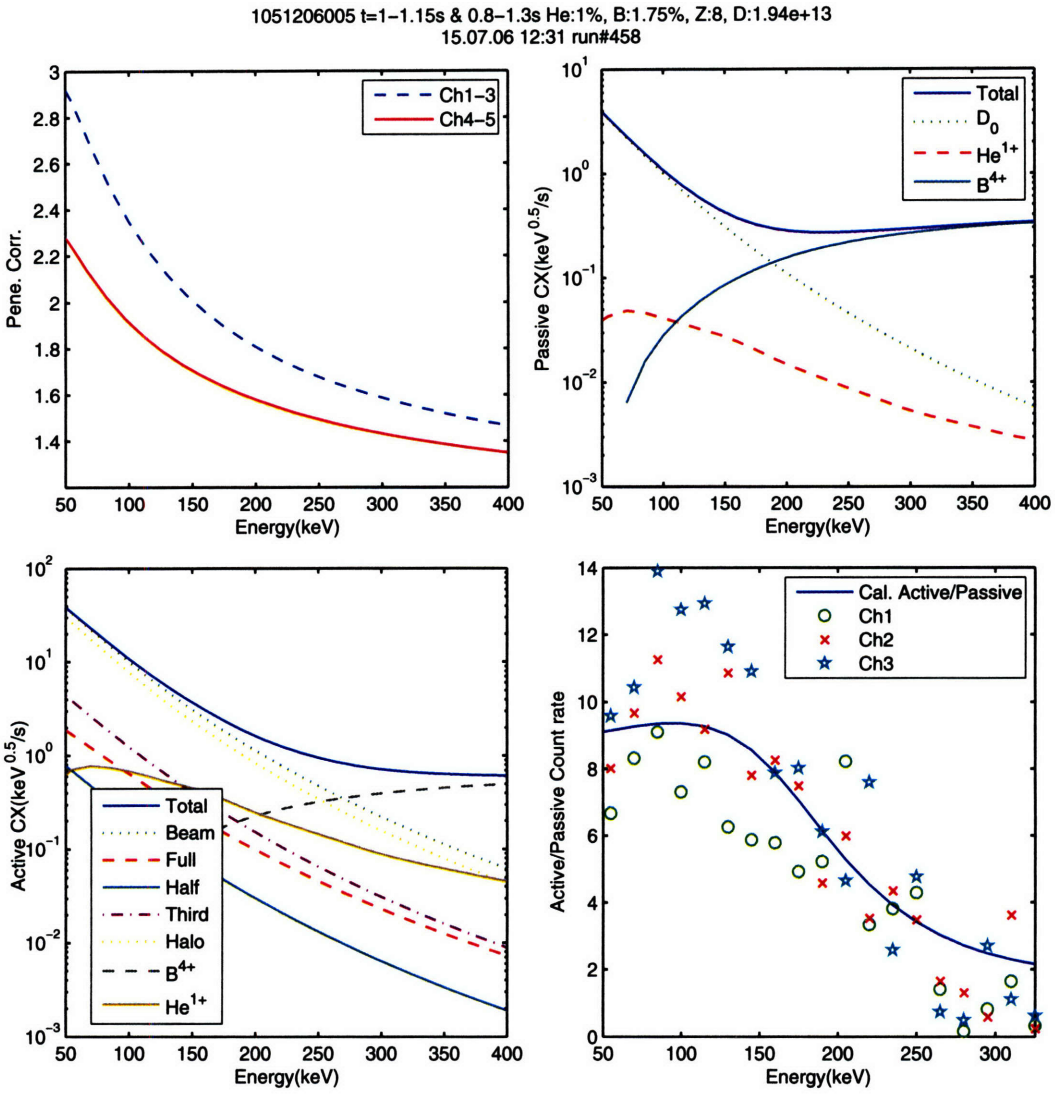

Figure 4-19: Summary of charge-exchange parameters for 1051206005 analysis assuming Z_p=8 cm, 1.75% boron, and 1% helium.

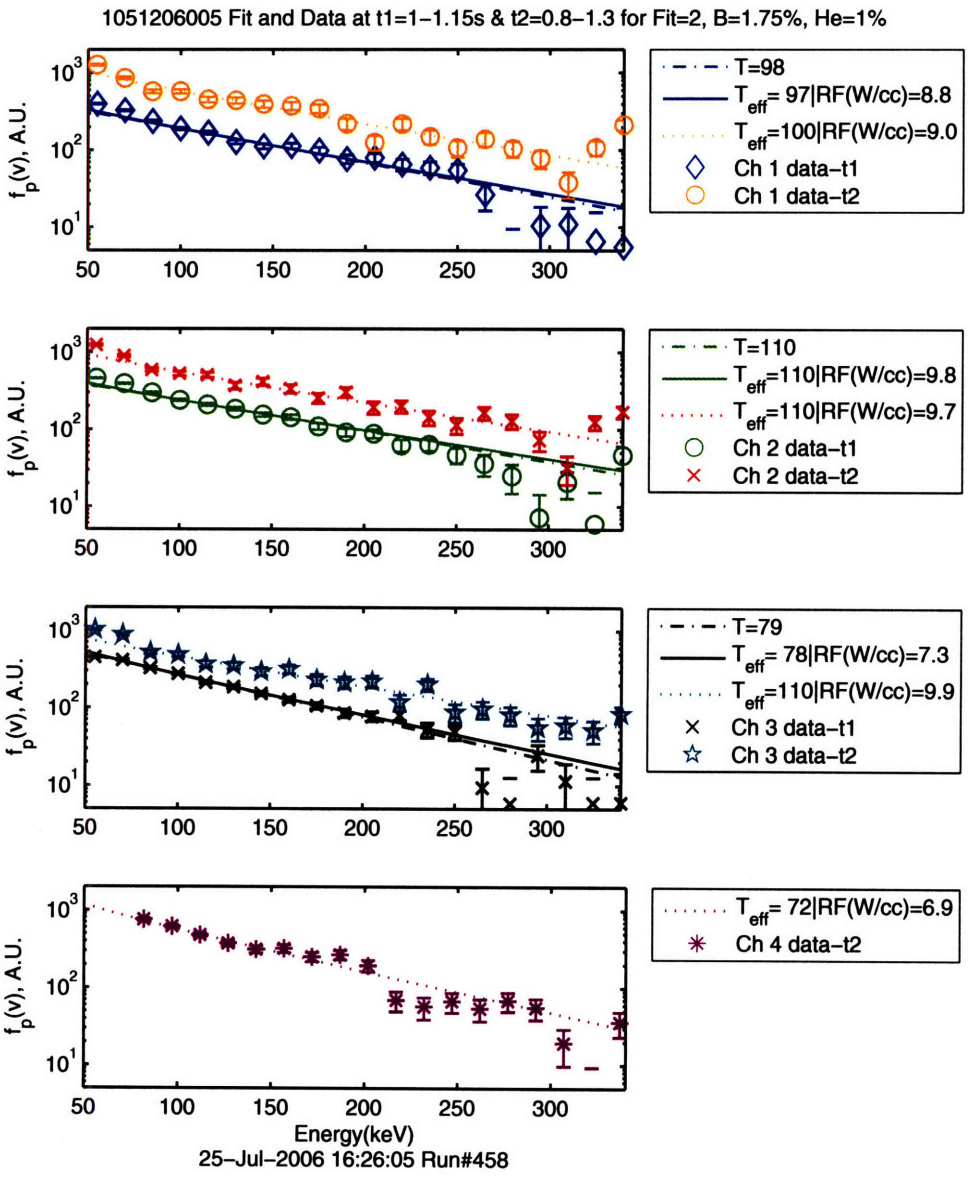

Figure 4-20: Passive and active CX inferred minority distributions, $f_p(v)$, and temperature fits for 1051206005 analysis assuming Z_p=8 cm, 1.75% boron, and 1% helium. The spectra are well-behaved with good temperature fits.

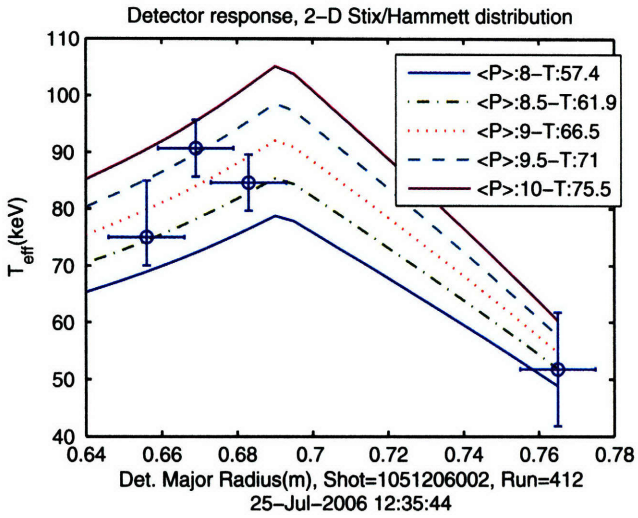

Figure 4-21: 2-D Hammett model distribution pitch angle T_{eff} as a function of major radius for different input mid-plane averaged power densities at Z_p=7 cm. Overlaid on top are the experimentally deduced T_{eff} from Ch1-4. The legend indicates the input power used for each line and the resultant mid-plane pitch-angle averaged T_{eff}, or T_{fa}. The flux surface averaged value can then be determined using the resultant mid-plane distribution function.

an independent comparison of the on-axis fast proton temperatures with the CNPA inferred temperatures at Z_p. After this, the remaining sections documents how the minority temperature scales with the Stix parameter and also provide additional proof that these fast protons are indeed off-axis using the sawteeth analysis.

4.5 Sawteeth Reheat Analysis

The dW/dt sawteeth analysis is based on the procedure used by O'Shea[9] and M. Greenwald. The procedure is modified to include subtraction of the estimated r/a=0 ohmic heating power which O'Shea ignored. Specifically, the fast proton temperature can be inferred if the electron heating power from the fast minority ions is known:

$$T_{fa} = \frac{2}{3}\frac{P_{e,p}\tau_{S,e}}{2n_m} \tag{4.10}$$

where $P_{e,p}$ is the electron heating power and $\tau_{S,e}$ is the fast ion slowing down time on the electrons. The factor of 2 in the denominator converts the slowing down time to an energy exchange time. A full discussion of this can be found in O'Shea's

thesis. Note that the factor on the right is almost the same as ξT_e, with the key difference being the power taken in the Stix parameter is the minority absorbed RF power, not $P_{e,p}$. For high temperature tails ($>\sim$ 20 keV), the fast protons slows down dominantly on the electrons and these two powers eventually become the same. In any event, neglecting finite orbit widths, the use of $P_{e,p}$ makes equation 4.10 valid for all fast proton energy range on a flux surface.

By analyzing the transient temperature response of the electrons immediately after a sawteeth crash, the total electron heating power, $P_{e,tot}$ can be determined. $P_{e,p}$ for a minority heating case can be found from $P_{e,tot}$ via:

$$\frac{3}{2}n_e\frac{dT_e}{dt} = \frac{dW}{dt} = p_{e,tot}\sim p_{e,p} + p_{e,ohmic} \tag{4.11}$$

where $p_{e,ohmic}$ is the ohmic heating due to the plasma current, estimated by results from TRANSP. Power terms based on spatial gradients are ignored since the reheat analysis is done right after a sawteeth crash, when the temperature profiles are expected to be flat.

Using an IDL program from Greenwald, Figure 4-22 shows the $p_{e,tot}$ estimated from each of the sawteeth crashes illustrated for shot 1051206002. The inferred heating power of $\sim$3.2 W/cm^3 and an ohmic heating power at r=0 from TRANSP of $\sim$1.6 W/cm^3 give a T_{fa} of $\sim$15keV for the r/a=0 minority proton distribution. This temperature is lower than the Z_p=7 cm T_{fa} from the CNPA measurements and supports the idea of a hollow minority temperature profile. It must be noted that the error bars of the inferred fast ion temperatures are quite large with this method, since the reheat power, ohmic power, and the minority ion density all have large errors. Also, the $r/a = 0$ channel of the ECE diagnostic used for this analysis has a spatial resolution of $\sim$2 cm.

4.6 Analysis Results from Simple Model

For this thesis, the major conclusions from employing the simple model on Alcator C-Mod discharges are that the C-Mod minority proton temperatures within the examined shots follow the expected Stix scaling and that these fast ions are peaked spatially away from r/a=0, even for an on-axis resonance. This off-axis heating conclusion is independently verified from minority temperatures deduced from dW/dt analysis and explained by the FW/FP AORSA/CQL3D simulations. This section documents these results.

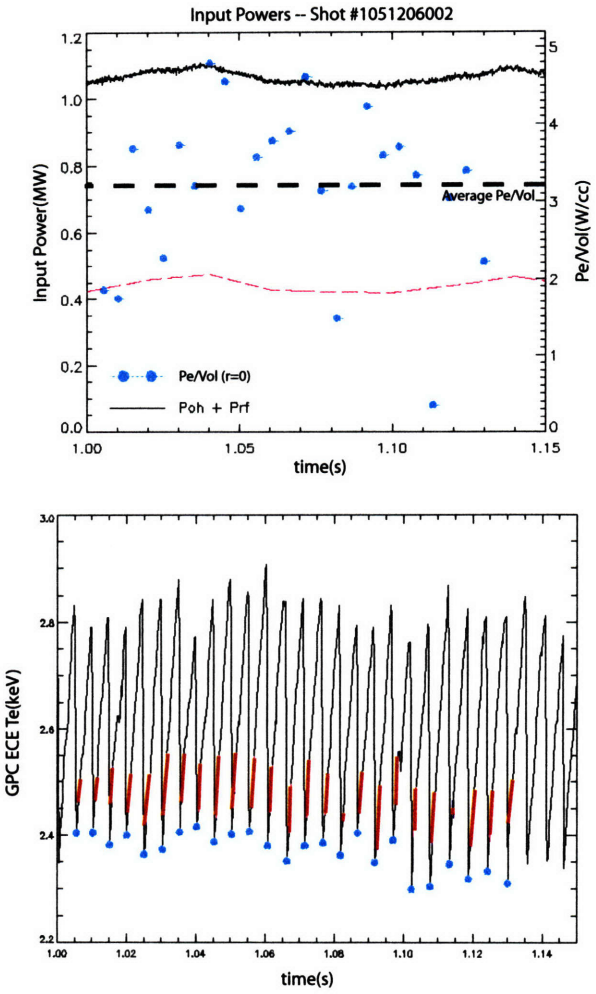

Figure 4-22: Demonstration of the sawteeth reheat analysis based on Greenwald's IDL program. The top plot gives the $p_{e,tot}$ found from each of the sawteeth marked on the bottom plot and are labeled by 'Pe/Vol'. The total ohmic and ICRF powers are also plotted. On the bottom plot, the segment of the electron temperature used for each of the calculations are also highlighted.

As discussed in Chapter 2, Stix calculated that the effective minority proton temperature should scale approximately with the Stix parameter, namely $T_{\text{eff}} \propto \frac{P_{rf}\tau_s}{3n_m} = \xi T_e$ for T_{eff} greater than the critical electron slowing down energy. This critical energy marks the transition between the fast protons dominantly slowing down on bulk ions instead of electrons and is typically ~20 keV for Alcator C-Mod discharges in this thesis. The physical interpretation of the scaling is that the minority tail temperature is determined by the amount of power absorbed during one fast minority ion-to-electron energy exchange time. The RF portion of this scaling has been verified extensively on JET[10] and TFTR[41, 11]. Hammett's power scaling analysis for PLT concentrated mainly on second harmonic deuterium heating.

Off-axis heating profiles are found in Hammett's analysis of the passive CX data from PLT. In order to match the passive CX data, Hammett assumed |E+| profiles with peaks as far as $r/a\sim$ 0.5 in his FPPRF code. However, these PLT shots do not have active beam or dW/dt data to independently verify these heating profiles. His thesis notes that attempts to derive this off-axis effect from a wave/FP code were not successful.

In this thesis, 13 discharges from 1051206 that span a factor of ~6 in the scaling parameter and ~3 in temperature are reviewed with the simple model. These shots have plasma parameters B_T=5.4 T,I_P = 600 kA, $n_H/n_D \sim 3\% - 9\%$, $n_e l \sim 3 - 7 \times 10^{19}/\text{m}^3$, $\sim 0.3 - 0.6$ MW of RF power from t=0.5-1.5 s, and heating resonance at R ~69 cm. The magnetic axes are at ~68-70 cm. The DNB fired from t=1.0-1.15 s. Shots 1-8 and 14-17 are LSN, while 9-13 are IWL. The CNPA sightlines are slightly modified for these discharges, and cover $R \sim 64.5 - 69.5 \pm 1$ cm, instead of the usual 65-70 cm. Each of the viewing cones for the vertical channels have widths of ~2.3 cm, resulting in coverage of R=64.5-66.8 cm for Ch1, R=65.8-68 cm for Ch2, and R=67.2-69.5 cm for Ch3. The horizontal channel is unchanged and remains approximately at the mid-plane with a ~3 cm wide viewing cone at R=69 cm.

The analysis procedure for each shot is as discussed in the previous sections; the input parameters of the model, mainly Z_p, helium fraction, and boron fractions are varied with constraints determined from other diagnostics (for example, the HeII diode for He density) until a reasonable match is found for the active/passive CX count rates and temperatures. Because of the manual nature of this procedure, it is not guaranteed that the best match is found, and the error bars given for the inferred temperatures reflect this. Over 400 analysis runs were performed for these 13 discharges in this thesis. Each takes approximately 5 minutes on a Pentium 4 3.2 GHz PC.

For three of these shots (5, 7, 13), helium is puffed in with the original goal of explicitly seeing its effect on the inferred distributions. As it turns out, this proved difficult since a large amount is required and this makes the shot no longer a repeat of a non-puff shot. Also, contrarily to what is typically assumed, significant helium is found for the shots following those plasmas with puffs. The absolutely calibrated HeII diode is able to provide estimates of the He fraction for the LSN discharges. Coincidentally, the CHROMEX diagnostic also saw the same trends. The input parameters resulting in reasonable fits of the passive and active CX data do require helium fractions similar to what the HeII diode reports. The measured helium fractions ranged from 0-5% for the LSN shots. The inner wall shot with long puff, 13, has a CNPA inferred $\sim$10% n_{He}/n_e.

Concerning the IWL shots, the objective is to increase the boron impurity in the plasma. In the analysis, it is indeed found that a higher boron fraction is needed to reconcile the passive and active data for these IWL shots. Spectroscopically, the Z_{eff} also increased. The good analyses typically require boron fractions of 1-2% for the LSN shots and $\sim$2.5% for the IWL plasmas.

n_H/n_e ratios for these shots are estimated from $\sim 0.85 \times n_H/n_D$ with error bars of $\sim \pm 1\%$. A difficulty with some of these shots, especially the IWL ones, is non-existent n_H/n_D spectroscopic data. This does not affect the CNPA temperature fits, but does affect the inferred power density and the dW/dt deduced temperatures. For the shots with no spectroscopic data, n_H/n_e is assumed to be $6\% \pm 2\%$. Almost all of the shots with n_H/n_D data lie in this range.

Within the experimental error bars, the CNPA deduced T_{eff} indeed scale approximately with the Stix scaling. This trend is evident in the Ch2, Ch3, and flux surface averaged results. The scatter in the data is larger for Ch1 and Ch4. It is possible to infer a flattening of the T_{eff} at higher scaling numbers ($\sim$60 in the following plots), especially for Ch4, but the data in that regime is sparse for all channels; a flattening implies broadening of the fast ion spatial profile which would be consistent at high T_{eff} due to orbit effects. Orbit effects decrease the effective slowing down time since the fast protons travel through cooler parts of the plasma when the orbits are large. This then reduces the T_{eff}. Additionally, the T_{eff} for that point is at the limit of applicability for the simple model because the fitted portion of the spectra is no longer significantly higher in energy than the minority temperature. Next, the anisotropy, or fast ion localization, of the minority proton distribution is again seen from the consistently lower temperatures of the horizontal channel when compared with the Ch2-Ch3 results. These temperature trends do not change significantly with fits from

different distribution models, nor do they change between the active and passive data. Lastly, the fast proton temperatures are found to peak away from $r/a = 0$ for all of these shots, even though the resonance is on the magnetic axis. All of these results are summarized via the accompanying plots:

- Figure 4-23 summaries the T_{eff} data for Ch3, Ch4, the flux surface average at Z_p, and the Z=0, or r/a=0 flux surface average based on dW/dt sawteeth analysis for each shot. The Ch1-Ch3 data is typically more energetic than the Ch4 data, as expected. For all the shots, the CNPA based temperatures are higher than the r/a=0 fast ion temperatures, supporting the CNPA off-axis fast proton peak conclusion.

- Figure 4-24 summaries the Z_p determined from the passive and active CX CNPA data for each shot. All of the shots with on-axis resonance have off-axis peaks.

- Figure 4-25 gives the measured T_{eff} from the Stix distribution fits vs. the Stix scaling for Ch1-4. The Ch1-3 data are from the active CX data. Core averaged (r/a=0-0.5) plasma parameters are used to calculate the Stix parameter.

- Figure 4-26 gives the measured T_{eff} from a simple exponential fit of CNPA data vs. the Stix scaling. The Ch1-3 data are again from active CX. The scaling trend is not affected with a different distribution model.

- Figure 4-27 gives the measured T_{eff} from the Stix distribution for the passive CX analysis. The Ch4 data is the same as Figure 4-25 and re-plotted here for comparison. The linear scaling trend is not affected; in fact the Ch1 data seem to now have less scatter. This could be because the passive fits are not weighted and tend to handle distributions with multiple effective temperatures better, since the un-weighted fits simply takes an average of those effective temperatures.

- Figure 4-28 plots the sawteeth reheat r/a=0 temperatures with the flux surface averaged temperatures against the Stix scaling. The linear trend is evident, and the lower temperatures from the r/a=0 analysis again supports the off-axis fast ion conclusion. There is a possible flattening of the fast proton temperature at high Stix scaling parameter, but this is only supported by one shot (1051206001) with large errors.

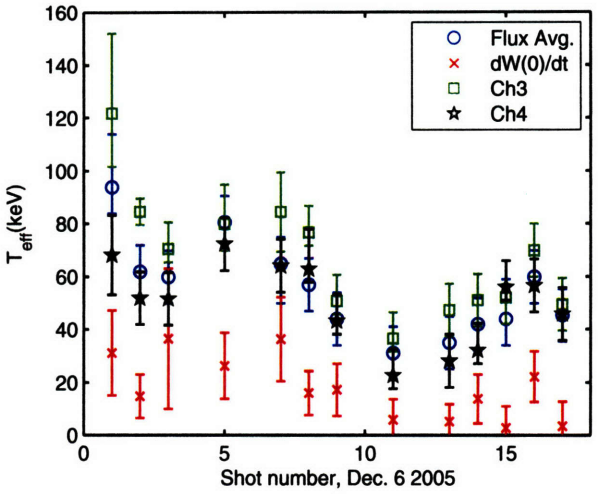

Figure 4-23: Summary of some of the CNPA data from 1051206. For clarity, only the T_{eff} from Ch3 and Ch4 are plotted. The error bars are estimated from varying the input parameters of the simple model. The flux surface averaged temperatures are from the 2-D Hammett/Stix model distribution based on the CNPA data. The dW/dt analysis are measurements of the r/a=0 fast proton temperatures. The error bars on these calculations are estimated by analyzing the uncertainty in n_H/n_D and the r/a=0 ohmic heating power.

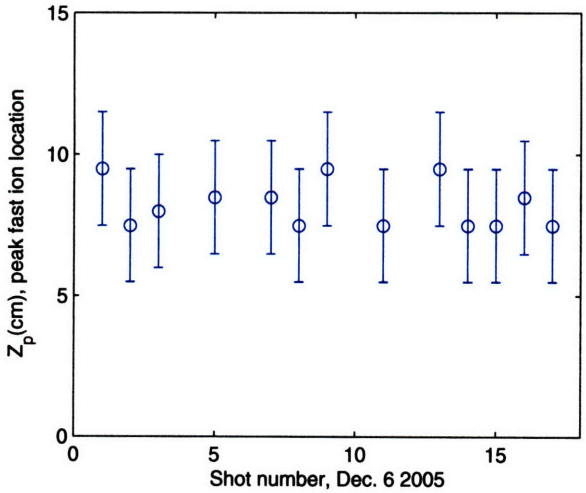

Figure 4-24: Summary of the deduced peak minority ion location from 1051206. Even for these plasmas with on-axis heating resonance, the simple model indicates that the fast ions do not peak at r/a=0.

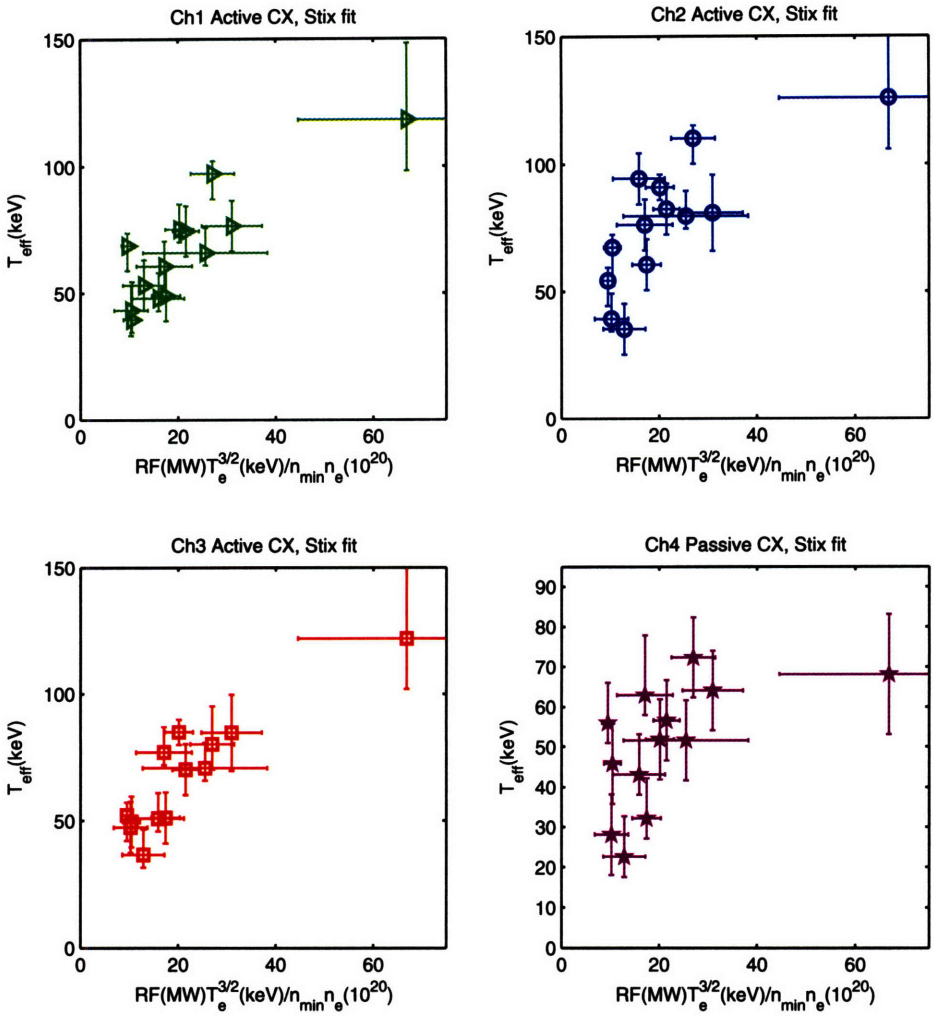

Figure 4-25: Summary of active CX T_{eff} using a Stix distribution fit. Core averaged (r/a=0-0.5) plasma parameters are used to calculate the Stix scaling parameter. The Ch4 data are based on passive CX only.

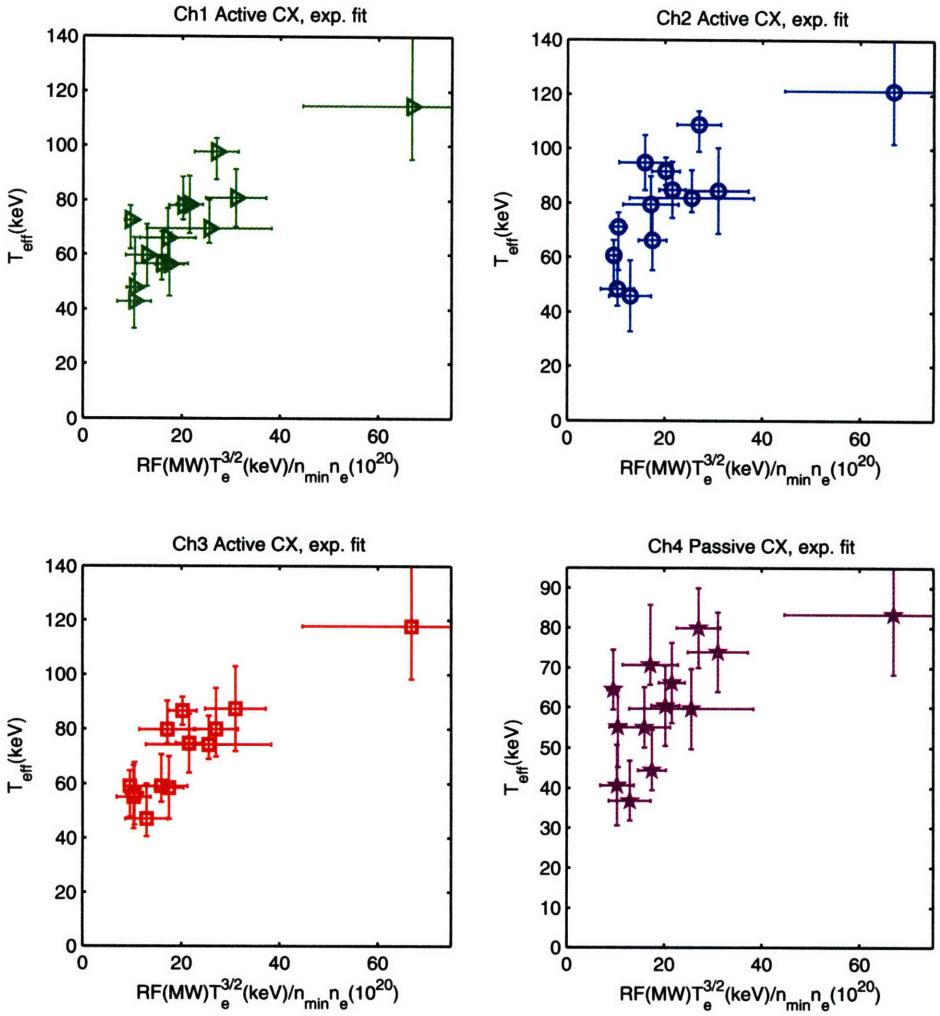

Figure 4-26: Summary of active CX T_{eff} using a Maxwellian distribution fit. Core averaged (r/a=0-0.5) plasma parameters are used to calculate the Stix scaling parameter. The Ch4 data are based on passive CX only.

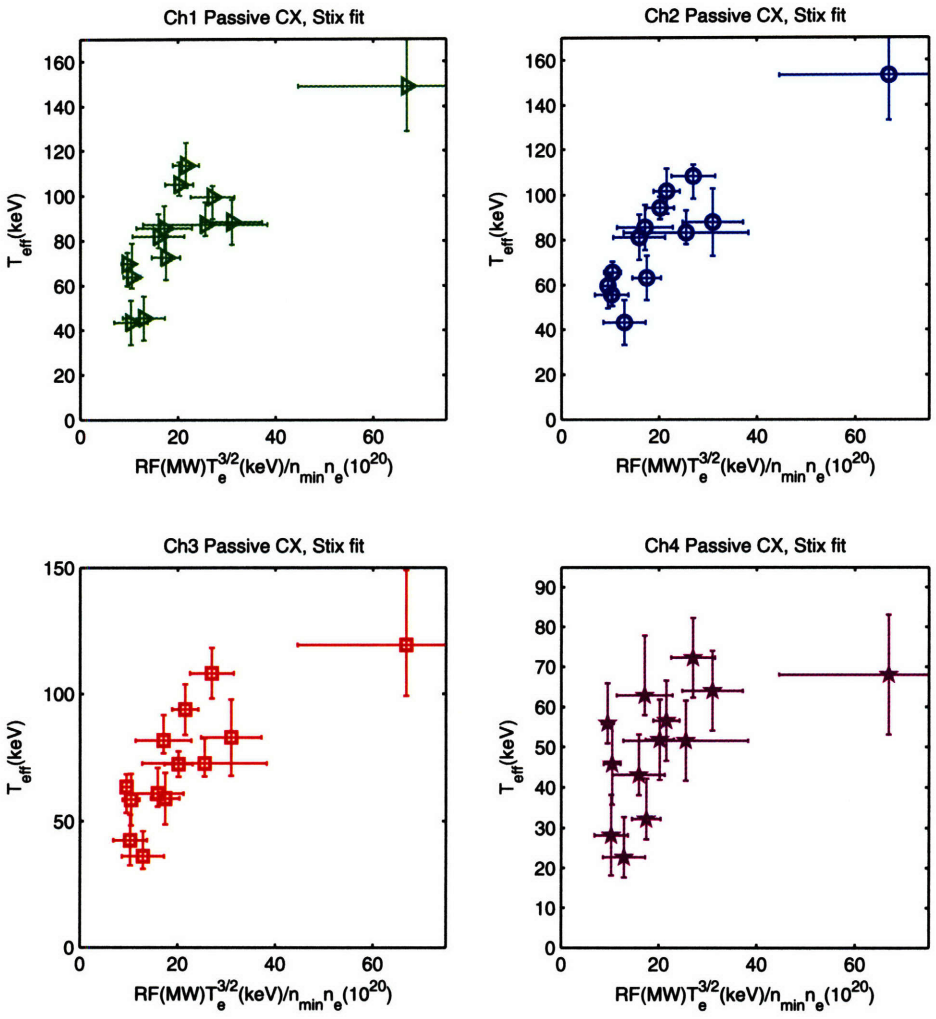

Figure 4-27: Summary of passive CX T_{eff} using a Stix distribution fit. Core averaged (r/a=0-0.5) plasma parameters are used to calculate the Stix scaling parameter. The Ch4 data are re-plotted from Figure 4-25.

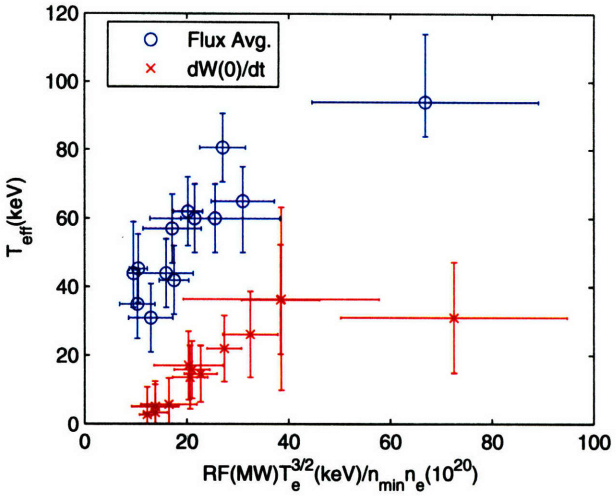

Figure 4-28: Plot of the 1051206 r/a=0 reheat based fast proton temperature and the flux surface averaged CNPA based temperatures as a function of the Stix scaling parameter. The value of the Stix scaling parameter is slightly different for the r/a=0 analysis because r/a=0 plasma parameters are used instead of core averaged parameters.

Before leaving this section, it is noted that for the lower T_{eff}, a more appropriate scaling might take into account the fast proton-bulk ion slowing down time. Incorporating this would then make the scaling a function of T_{eff}. This would decrease the net slowing down time and move some of the lower T_{eff} (~50 keV) points to the left in the scaling plots.

With the CNPA results established, the next section provides comparisons between these data and coupled FW/FP solvers.

4.7 Comparisons with Full Wave/Fokker Planck Simulations

In this section, comparisons between the experimental data discussed above are made with the FW/FP solvers TRANSP TORIC5/FPPRF and AORSA/CQL3D. These AORSA/CQL3D runs are performed by E.F. Jaeger[51] at ORNL. Discrepancies in the peak fast proton temperature and its spatial location are found with the TRANSP simulations while good matches are found with the AORSA/CQL3D simulations. A feasible explanation is given for these differences. This AORSA/CQL3D package is quite new and these are the first Alcator C-Mod results and comparisons with

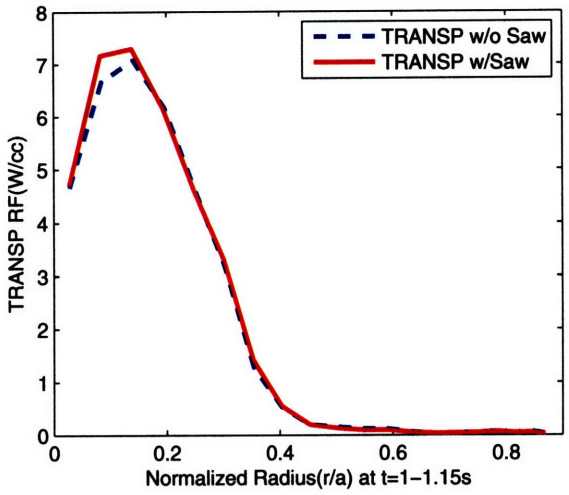

Figure 4-29: TRANSP TORIC5/FPPRF calculated minority absorbed RF power for shot 1051206002. The code calculated ~92% absorption.

TORIC/FPPRF.

To start with, Figures 4-30 and 4-29 compares the TRANSP TORIC5/FPPRF simulations for shot 1051206002 from t=1.0-1.15 s with the available flux surface averaged fast proton temperatures and power deposition from experiment. $N_\phi = \pm 10$ and 31 poloidal modes are used for these simulations. Both runs with and without the sawteeth model are shown; the run with sawteeth has a broader profile as expected. Qualitatively, TORIC5/FPPRF in its current setup predicts significant power deposition at r/a~0 which results in high minority temperatures on-axis. This is counter to the experimental results. Specifically, the inferred r/a=0 temperature is only ~15 keV from the dW/dt reheat analysis. As for the CNPA data, TRANSP under-predicts the power deposition and hence fast ion temperature at r/a~0.3, although the difference is much smaller than the r/a=0 comparison and might be due to the fact that the flux surface temperature is based on the use of Hammett's model distribution. In any case, the r/a=0 result is consistent with O'Shea's earlier finding that FPPRF over-predicts the r/a=0 temperatures. Presumably, the power deposition and fast proton temperature would increase at r/a~0.3 if the simulation reallocated the absorbed power from r/a~0-0.15 outward.

As for the AORSA/CQL3D results, the comparison is better. No sawteeth model is currently available for this package but their effect is expected to be small to moderate, depending on the r/a location. A flavor of this is already given by the TRANSP TORIC5/FPPRF results. Figures 4-32 and 4-31 show the AORSA/CQL3D

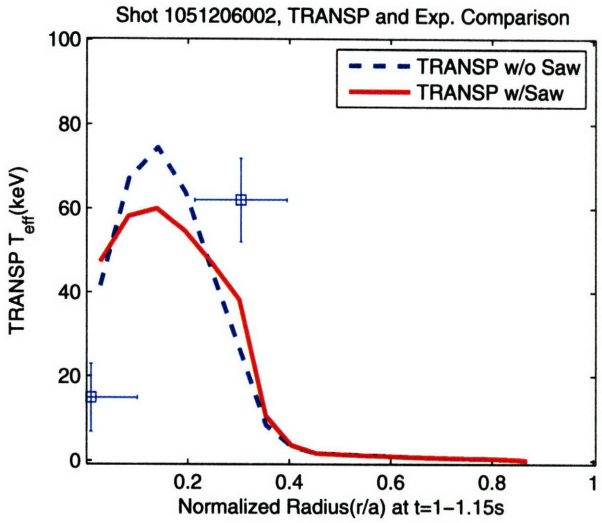

Figure 4-30: TRANSP TORIC5/FPPRF calculated T_{eff} for shot 1051206002 and available experimental data. The value at r/a=0 is from a sawteeth reheat analysis and the point at r/a~0.3 is from the CNPA flux surface averaged T_{eff} using Hammett's 2-D model distribution.

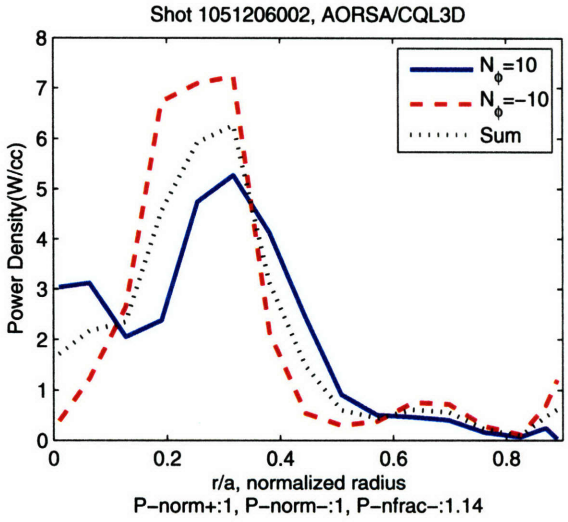

Figure 4-31: AORSA/CQL3D 1051206002 flux surface averaged RF power deposition profiles for $N_\phi = 10$ and $N_\phi = -10$ phasings. The 8% $\rightarrow$ 7% n_H/n_e factor has been applied to the profiles. The symmetric N_ϕ results are approximated by an average of the two cases. The code calculated a ~91% total RF absorption.

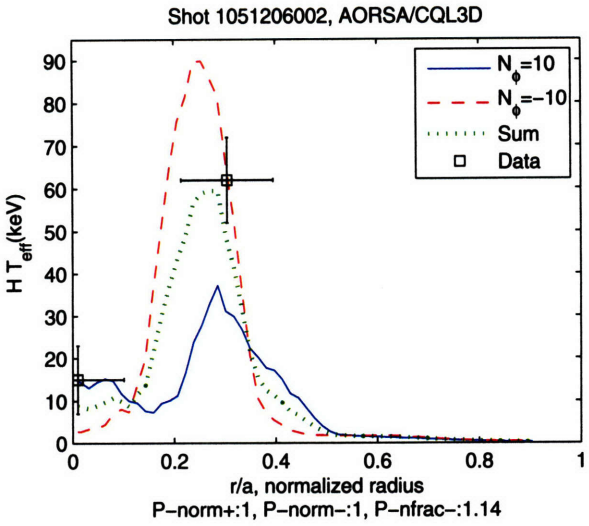

Figure 4-32: AORSA/CQL3D 1051206002 flux surface averaged T_{eff} profiles for $N_\phi = 10$ and $N_\phi = -10$ phasings. The 8% $\rightarrow$ 7% n_H/n_e factor has been applied to the profiles. The symmetric N_ϕ results are approximated by an average of the two cases.

results with $N_\phi = 10$ and $N_\phi = -10$. The current AORSA/CQL3D setup permits only one N_ϕ per simulation; work is ongoing to combine the results from individual N_ϕ runs correctly to approximate the real antenna spectrum. For a rough approximation, the profiles from these two N_ϕ are averaged to estimate the symmetric case. The total power deposited from the two N_ϕ cases are 82% and ~100% respectively; it is not certain why the $N_\phi = -10$ case resulted in higher minority absorption. However, a simple average of the two cases results in 91% absorption which is consistent with the TRANSP case. Additionally, the tail temperatures from both N_ϕ cases are scaled to 7% n_H/n_e from the 8% used for the simulations. This tweak raises the minority temperatures by 8/7.

Even given the preliminary nature of these sophisticated simulations, the AORSA results match the experimental data rather well. The fast proton temperature at r/a=0 is ~10 keV, as measured. The T_{eff} peaks at r/a~0.3-0.4 is around 50 keV which is also consistent with experiment. Comparisons between the distributions at the resonance pitch angle and peak r/a with Ch3 data are also good. Detailed synthetic diagnostic results with these simulations are discussed in the next chapter.

There are several possible reasons why the AORSA/CQL3D combination works better than the TORIC5/FPPRF package. Because the CQL3D and FPPRF codes are nominally based on the same physics, i.e. 2-D bounced averaged orbits coupled to a RF quasi-linear diffusion operator, the differences should be in the wave solver

and/or the coupling code that handles the interaction between the Fokker-Planck and wave solver. Concerning the first option, the fundamental difference between AORSA and TORIC is that FLR effects are completely included in AORSA, since no approximations to the dielectric tensor is made. But for minority heating at moderate tail energies, FLR effects in the wave propagation and power absorption should be small. The second possibility bears more fruit. As it turns out, the iteration to steady-state in the TRANSP TORIC5/FPPRF package is carried out using equivalent Maxwellians[52]. Specifically, the 2-D distribution in FPPRF is not directly used in the TORIC calculation of the power absorption; only average $T_\perp$ and $T_\parallel$ are used. This averaging of the 2-D distribution alters the dynamics of the power absorption because the details of the resonantly localized fast ions are significantly changed. As discussed in Chapter 2, these trapped ions spend the longest time around the resonance and hence absorb significantly more power than average. Also, as the heating continues, the density of these resonantly localized fast ions on each flux surface increases. Because particles can not become easily trapped near $r/a{\sim}0$, there is a tendency for the power absorption to move off-axis along the resonance in the +Z and -Z direction. TORIC5/FPPRF essentially removes this trapped ion density build-up near the resonance. Hence, since the AORSA/CQL3D package retains the complete 2-D bounced average distribution during each iteration, it is able to simulate this off-axis heating effect properly and produce fast ions that are peaked further out then TORIC5/FPPRF. Further support for this explanation comes from examining the AORSA/CQL3D profiles before steady-state. In fact, at the 0th iteration, AORSA indeed predicts significant power density at r/a=0 for the minority ions with a Maxwellian distribution. This is shown in Figure 4-33. Nonetheless, further study with more extensive simulations are needed to confirm this conjecture and confirm the AORSA results.

4.8 Conclusion

In the previous sections, the main physics results of this thesis are discussed. A simple NPA model from JET is extended and adapted for the CNPA data. Extensive modeling is used to account for the effects of impurity CX and beam halos. Using these methods, effective peak fast minority proton temperatures for each channel are deduced, along with their spatial location. Flux surface averaged temperatures are also available from the CNPA data via a 2-D model distribution proposed by Hammett. These CNPA temperatures scaled as expected with a Stix scaling parameter. How-

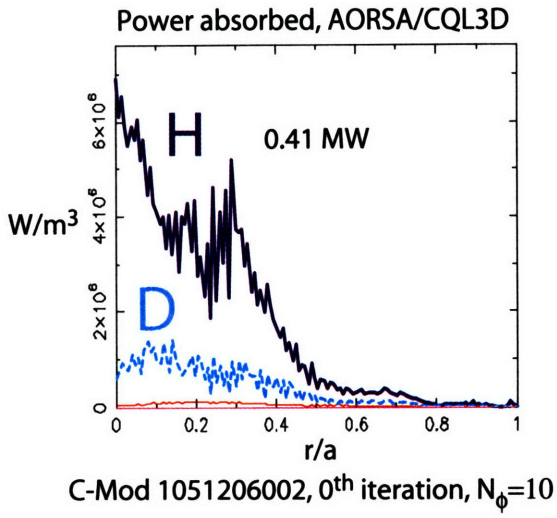

Figure 4-33: AORSA/CQL3D power absorption before iteration for Alcator C-Mod shot 1051206002. The power density at r/a=0 is significant, similar to the TRANSP TORIC5/FPPRF result. H and D represent the power to hydrogen and deuterium, respectively. At the final iteration, there is very little absorption due to second harmonic heating of deuterium. This figure is adapted from Jaeger[51].

ever, these fast protons are all found to be peaked off-axis, even though the resonances for the examined plasmas are all on-axis. This observation is independently confirmed via estimates of the fast ion temperature at r/a=0 using a sawteeth reheat technique. These r/a=0 temperatures are consistently lower than the ones from the CNPA. First comparisons between TRANSP TORIC5/FPPRF simulations and the experimental are relatively poor, in contrast to good agreement with AORSA/CQL3D simulation results. An explanation resolving this discrepancy is proposed which involve the use of equivalent Maxwellian distributions in the TRANSP TORIC5/FPPRF package.

Chapter 5

Synthetic Diagnostic Results

5.1 Introduction

As discussed in the previous chapters, for comprehensive comparisons between the CNPA experimental data and simulations, a synthetic diagnostic that accounts for the plasma profile details for each of the CNPA channels is needed. In other words, the use of a full simulated diagnostic permits the fast proton profiles to be determined. Mathematically, a synthetic diagnostic involves solving equation 4.1 with specified minority distributions. In general, a synthetic diagnostic is a reduction of the data set instead of solving the inverse problem and is therefore easier but not uniquely determined.

For this thesis, two complete synthetic diagnostics are implemented. The first is a passive CX only Fortran package that is natively implemented into CQL3D. The addition of this package to the CQL3D code permits the fusion NPA community to compare their experimental NPA results with CQL3D for energies up to ~100 keV using arbitrary sightlines. It is mentioned here for completeness as part of the work done for this thesis.

The results discussed in the following sections are from the second synthetic diagnostic. This diagnostic is a Matlab based post-processor for CQL3D that includes both passive and active CX. CX with hydrogen-like impurities are also accounted for. The plasma and sightlines are modeled in detail on a R-Z poloidal cross section of the plasma. In the next several sections, the use of this synthetic diagnostic is shown through a sample analysis of the AORSA/CQL3D data for shot 1051206002. Both the $N_\phi = 10$ and $N_\phi = -10$ cases are studied. As discussed in the last chapter, the real antenna spectrum is made up of both phasings. However, because of the inability to run both phasings simultaneously in the AORSA simulation, the $N_\phi = \pm 10$

results are again approximated by averaging the distributions from the $N_\phi = 10$ and $N_\phi = -10$ cases. Although it is not clear that this averaging approach is adequate, it is the simplest one available until the AORSA/CQL3D coupling code is rewritten to handle both phasings simultaneously. However, even at this preliminary stage, the comparison between these simulations and the CNPA data is reasonable and validates the use of the sample model for estimating the fast proton temperature and its spatial location. For contrast, a poorer comparison from a GENRAY[30]/CQL3D simulation of 1051206002 is also discussed. Unfortunately, TORIC/FPPRF minority distributions are not available from TRANSP to continue the comparison from the last chapter.

5.2 Analysis Procedures

The processes required for the full simulated diagnostic is similar to the calculations needed for the simple model. A step-by-step description is given in this section for the analysis of the Ch3 viewing cone for shot 1051206002. The bulk plasmas parameters used are taken from $t \sim 1$ s, during the active DNB period.

First, the plasma bulk parameters are established on a R-Z grid with a poloidal cross section of the plasma. This is done using EFIT results and the bulk plasma parameter as a function of major radius or r/a. The bulk plasma parameters are taken from Zhurovich's IDL fitting program, discussed in Chapter 1; a minimum Z_{eff} of 1.5 is imposed for shot 1051206002. Figure 5-1 shows the plasma density from this 2-D mapping process along with a sample viewing chord. Other flux surface parameters, such as the electron temperature and the background FRANTIC based D neutral density are also re-mapped this way. The size of the grid shown is 200×199 and spans Z=-0.69 to 0.69 m and R=0.43 to 0.92 m.

After the grid is established, the sightlines can be determined. The CNPA viewing cones are essentially vertical or horizontal, therefore the grid points for sightlines approximating those cones are easily ascertained. For each channel, results from three synthetic chords spanning the width of the real viewing cone at Z=0 for the vertical channels or R=0.69m for the horizontal channel are averaged to approximate the real diagnostic views. For example, the three sightlines that approximate Ch3 are R=0.672, 0.683, and 0.694 m. One of these simulated sightlines for Ch3 and its associated grid points in the plasma is shown in Figure 5-1. With the chords established, the penetration out of the plasma for each of these grid points is calculated using the Janev cross-sections[45]; this is similar to the $P(E)$ calculation in the last chapter but

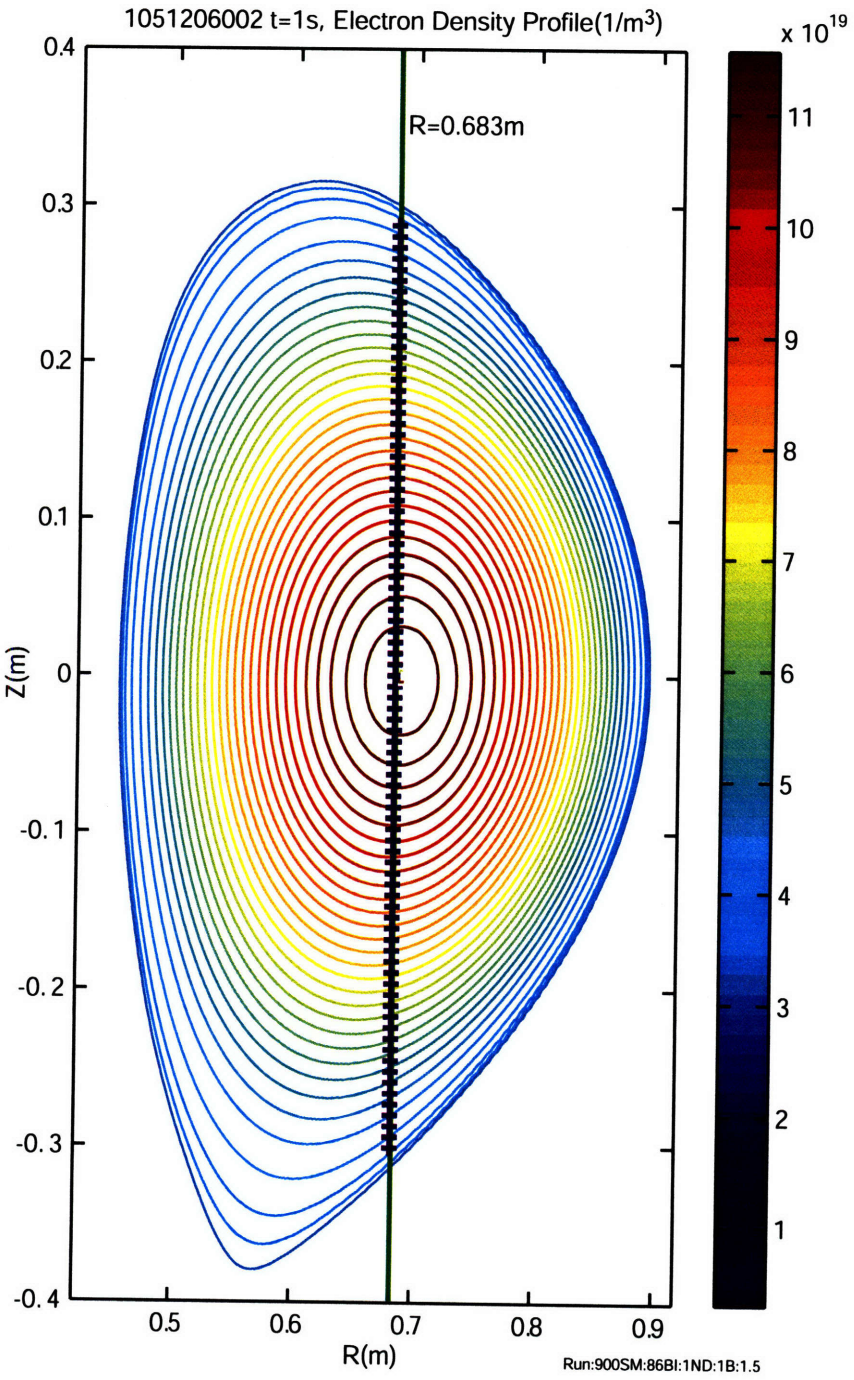

Figure 5-1: Electron density profile for shot 1051206002 at t=1 s. A sample sightline for the synthetic diagnostic is also plotted; the crosses indicate grid points that are within the LCFS and are determined automatically by the code.

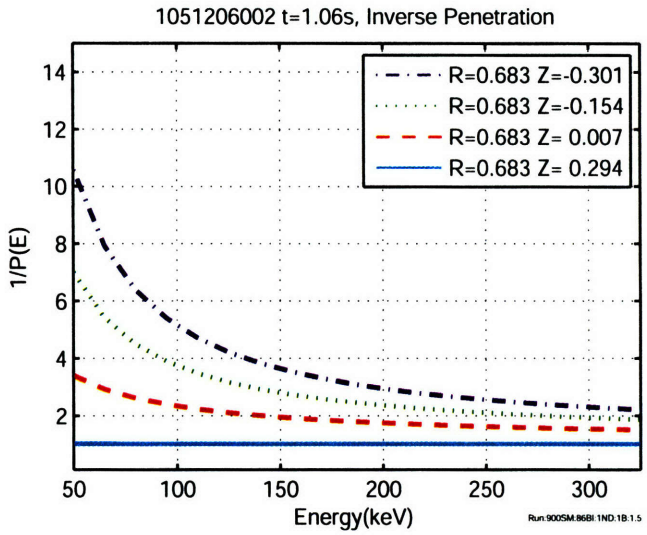

Figure 5-2: Inverse penetration curves for some of the marked gird points in Figure 5-1 based on Janev's neutral stopping cross-sections. The distances in the legends are in meters. Attenuation from neutral gas in the port duct are not included in the above curves.

now plasma parameters for each grid point are used. This results in plasma induced attenuations shown in Figure 5-2. Attenuation in the port duct due to residue neutral gas is accounted for separately.

Next, the electron donor densities are setup on the R-Z grid. For passive CX this is relatively simple since all the required quantities are flux surface functions. For the boron and helium impurities, equation 4.7 is used for each grid point assuming a constant n_b/n_e or n_{he}/n_e. Figure 5-3 gives a plot of this for the assumed 1.5% boron impurity in shot 1051206002. Things are slightly more difficult for active CX, since the beam and related densities are not flux surface functions. For the beam components themselves, the penetration as a function of major radius is determined by the procedure discussed in section 4.3.1. The halo density is now solved for as a function of major radius using plasma parameters averaged along $Z \pm 10$ cm for each R grid point, the mentioned beam densities, and the model from Section 4.3.2. These calculations result in beam and halo profiles shown in Figure 5-4. Lastly, the beam-induced impurity densities are implemented onto the 2-D grid. These are the trickiest to ascertain since these HL impurities still follow field lines but are not flux surface functions. A simple approximation which seems to work well is used here; the active CX $n_{imp,HL}$ densities from section 4.3.3 are used again and simply scaled by

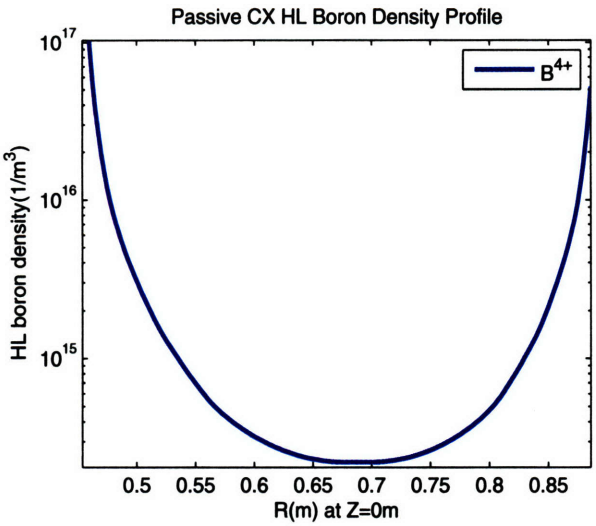

Figure 5-3: HL boron density profile used for passive CX calculations. The Z=0 vs. R profile shown here is mapped onto the $R-Z$ grid in Figure 5-1 for the synthetic diagnostic calculations.

$n_{imp,HL}/n_e$ for each grid point. This should be adequate for the core ($r/a \sim 0-0.5$) of the R-Z grid where the fast ions are dominantly located. Also, it is expected that the beam created HL impurities at larger r/a should not affect the vertical channels significantly because of the long field line distance ($\sim 2\pi R_0 q$, with q now greater than $\sim$1.5) they have to travel to intercept those chords. This approximation results in beam induced profiles shown in Figure 5-5.

With the electron donor densities established, the active and passive CX factors (i.e. the denominator of equation 4.2) for each of the grid points of the sightline are determined. All that is left is to step through each of these grid points, determined the local distribution from the CQL3D output, and multiply that by the CX and $P(E)$ factors to determine a local $\Delta F(E)$. The CQL3D distributions are based on mid-plane coordinates; these are re-mapped to a specific grid point by again using $v_{\|,\mathrm{mid}}/v = \sqrt{(1 - R_{\mathrm{tip}}/R_{\mathrm{mid}})}$, where R_{tip} is the R of the sightline and R_{mid} the equivalent midplane major radius for the flux surface. Summing the $\Delta F(E)$ from the grid points of the sightline then completes the expected $F(E)$ of that chord. In other words, equation 4.1 is solved. To illustrate, Figure 5-6 shows the relative contribution to the active CX $N_\phi = \pm 10$ $F(E)$ along one of the Ch3 sightlines. Clearly, the signal is primarily coming from $Z \sim$7 cm, as deduced from the simple model in the last chapter. The contribution from the lower portion of the discharge is smaller due to additional plasma attenuation; the CQL3D distributions themselves are up-down

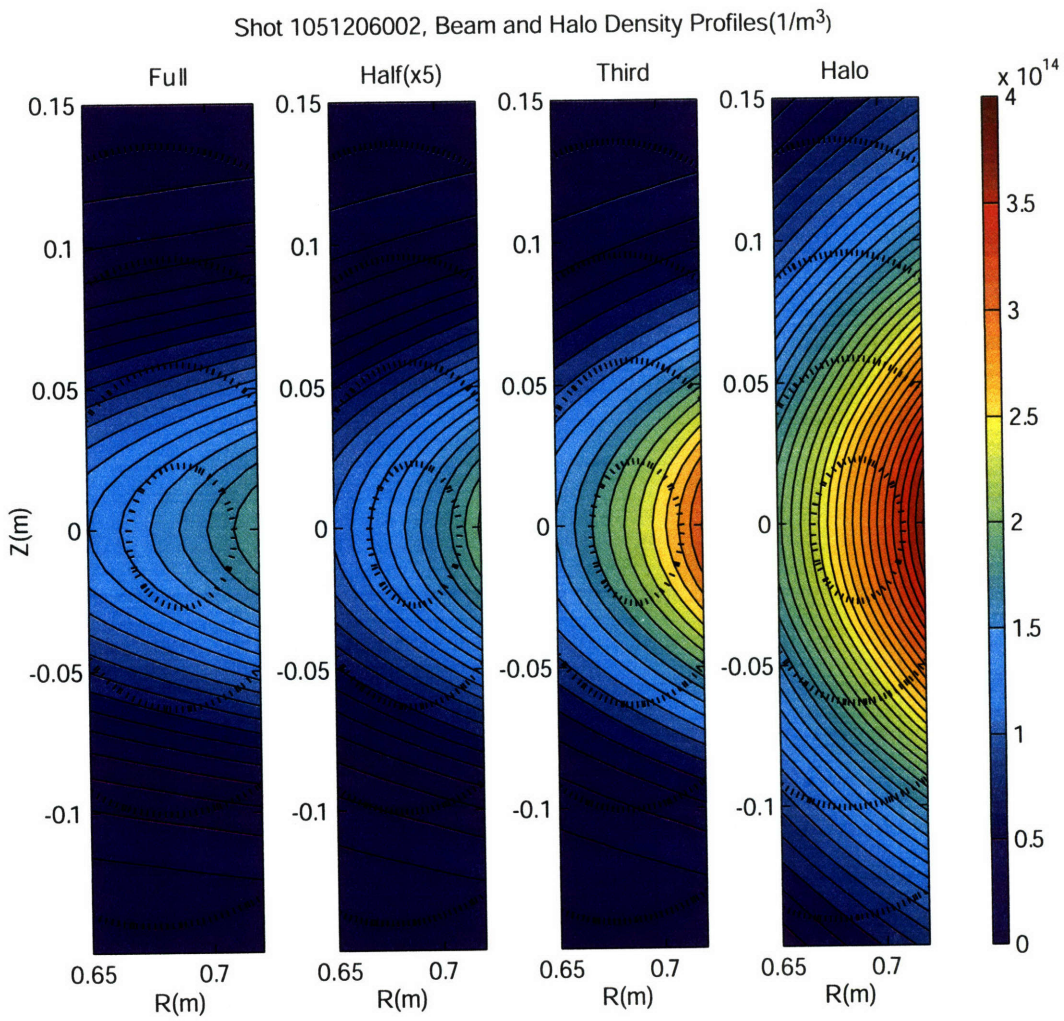

Figure 5-4: DNB and halo densities profiles used for active CX calculations. The half component density is multiplied by 5 for clarity. The dashed contours represents plasma flux surfaces.

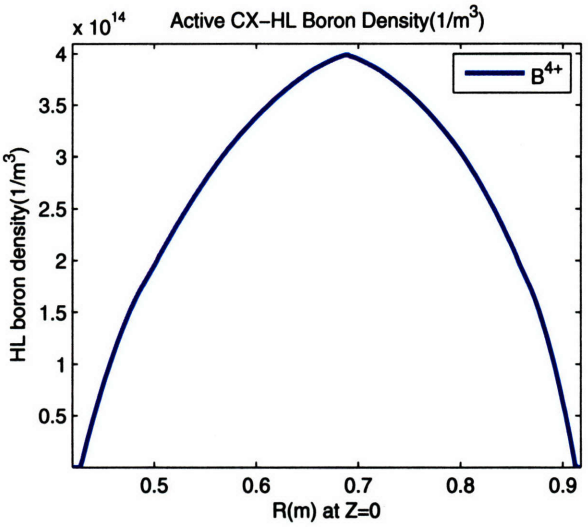

Figure 5-5: HL boron density profile used for active CX calculations. The Z=0 vs. R profile shown here is mapped onto the $R-Z$ grid in Figure 5-1 for the synthetic diagnostic calculations.

symmetric. With these calculations, the $F(E)$ from the three chords that approximate each channel are then averaged to simulate the real detector response for the given CQL3D minority distribution, as discussed above.

5.3 1051206002 Synthetic Diagnostic Analysis

In this section, the results from employing the calculations discussed above are shown for shot 1051206002. The simulated detector response from the AORSA/CQL3D $N_\phi = 10$, $N_\phi = -10$, and $N_\phi = \pm 10$ are given. The CNPA data match the AORSA/CQL3D well, although a higher than measured active/passive count rate is seen. In addition, for contrast, results from the same calculation using 1051206002 minority distributions from GENRAY/CQL3D are also discussed. GENRAY is not a full-wave solver and employs a ray-tracing technique that tends to focus the emitted RF power at r/a=0 which results in synthetic diagnostic spectra that do not fit the CNPA data. As discussed earlier, the ray-tracing approximation is not justified for these low density Alcator C-Mod plasmas because the wavelengths at 80 MHz are comparable to the size of the plasma.

Overall, the preliminary results are encouraging and show that the use of sophisticated FW/FP coupled codes such as AORSA/CQL3D is required to simulate the energetic proton populations in Alcator C-Mod with some degree of accuracy. It

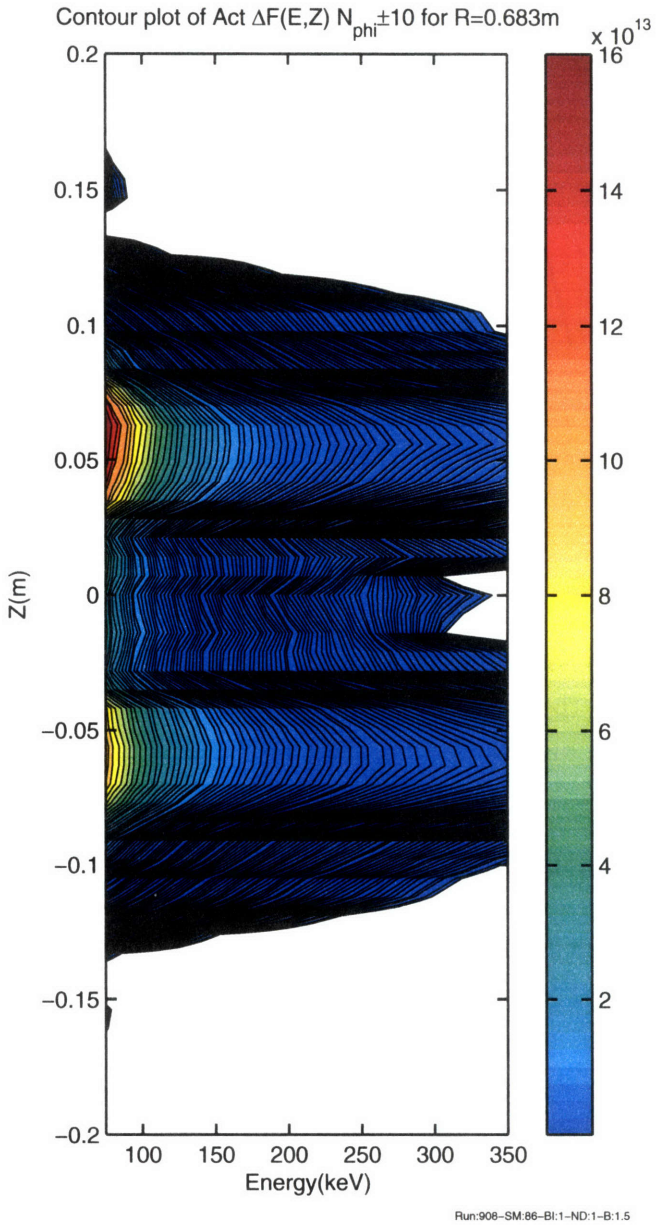

Figure 5-6: Relative fast neutral hydrogen emission rate with attenuation for the sightline in Figure 5-1. These data are for the $N_\phi = \pm 10$ case with active CX. The unfilled portions indicate an emission rate smaller than $\sim 10^{-9}$. Integrating along Z gives $F(E)$ for the sightline. The contours are logarithmic.

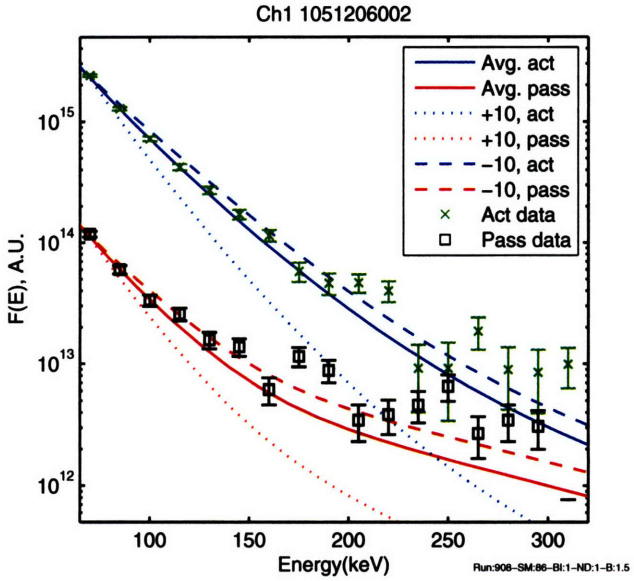

Figure 5-7: Ch1 AORSA/CQL3D synthetic diagnostic results assuming a 1.5% boron impurity. Both the active and passive CX are shown along with the simulated spectra. The spectra are normalized to the first CNPA data point for clarity. In the legend, 'act' and 'pass' stand for active and passive CX respectively. 'Avg.' indicates $N_\phi = \pm 10$ or an average of the N_ϕ=10 and N_ϕ=-10 results. The error bars are based on counting statistics only.

should be noted, however, that fast ion radial transport has not been accounted for in these runs and could affect these results if included.

Starting off, Figures 5-7 to 5-10 compare the active and passive CX based synthetic diagnostic $F(E)$ against the experimental $F(E)$. For these plots, all the spectra are normalized to the first CNPA data point to facilitate comparisons. To note, a better normalization constant might be determined by doing a least squares fit of the synthetic spectra with the data. The $N_\phi = \pm 10$ average $F(E)$ is typically dominated by the $N_\phi = -10$ case since the fast protons in that case are closer to $r/a = 0$ which results in both higher temperatures and count rates. The general features of the experimental spectra, such as the rapid rise past ~150 keV during passive CX, are reproduced by the synthetic diagnostic. This rise is again due to HL boron CX. The slopes, or effective temperature as a function of energy, of the distributions also show reasonable agreement.

However, certain phenomena, such as the 'negative' temperature regions in the ~200-250 keV portion of the Ch1 data, are not in the synthetic diagnostic spectra; orbit effects not included in the synthetic diagnostic could be to blame. Additionally,

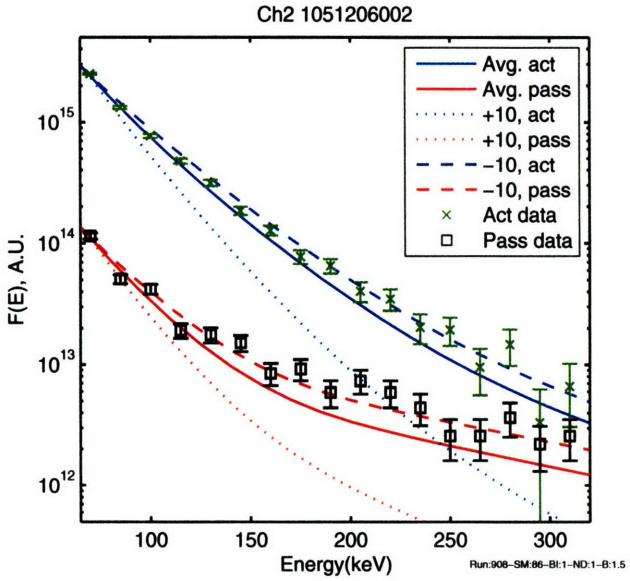

Figure 5-8: Ch2 AORSA/CQL3D synthetic diagnostic results assuming a 1.5% boron impurity. Both the active and passive CX are shown along with the simulated spectra. The spectra are normalized to the first CNPA data point for clarity. In the legend, 'act' and 'pass' stand for active and passive CX respectively. 'Avg.' indicates $N_\phi = \pm 10$ or an average of the N_ϕ=10 and N_ϕ=-10 results. The error bars are based on counting statistics only.

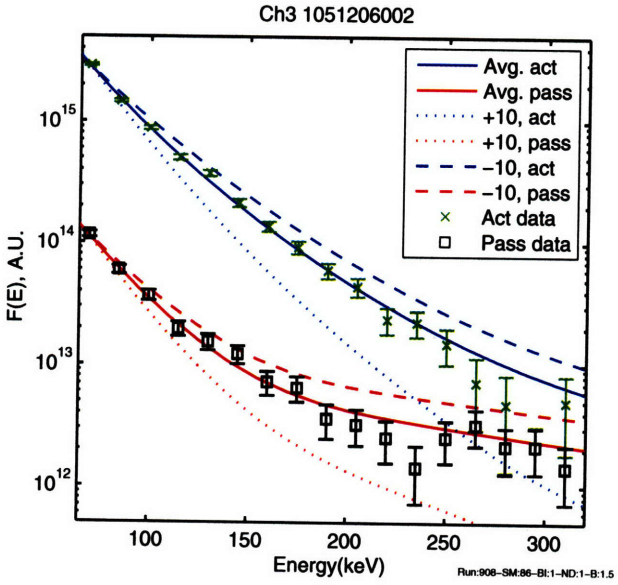

Figure 5-9: Ch3 AORSA/CQL3D synthetic diagnostic results assuming a 1.5% boron impurity. Both the active and passive CX are shown along with the simulated spectra. The spectra are normalized to the first CNPA data point for clarity. In the legend, 'act' and 'pass' stand for active and passive CX respectively. 'Avg.' indicates $N_\phi = \pm 10$ or an average of the N_ϕ=10 and N_ϕ=-10 results. The error bars are based on counting statistics only.

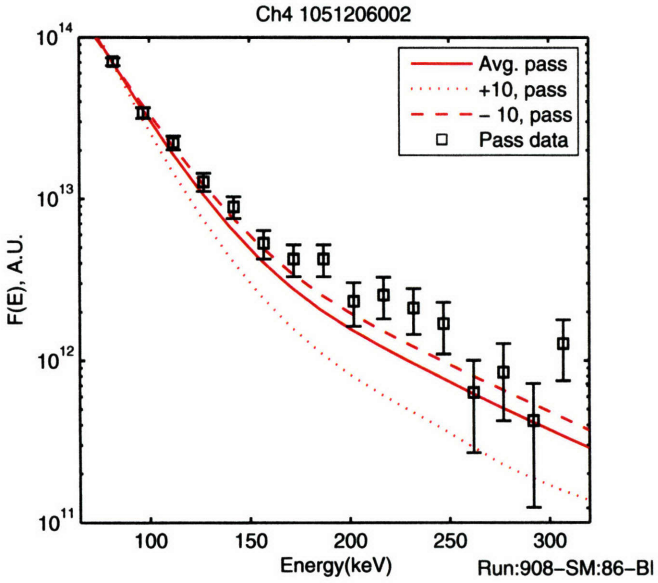

Figure 5-10: Ch4 AORSA/CQL3D synthetic diagnostic results assuming a 1.5% boron impurity. The passive CX are shown along with the simulated spectra. The spectra are normalized to the first CNPA data point for clarity. In the legend, 'pass' stand for passive CX. 'Avg.' indicates $N_\phi = \pm 10$ or an average of the N_ϕ=10 and N_ϕ=-10 results. The error bars are based on counting statistics only.

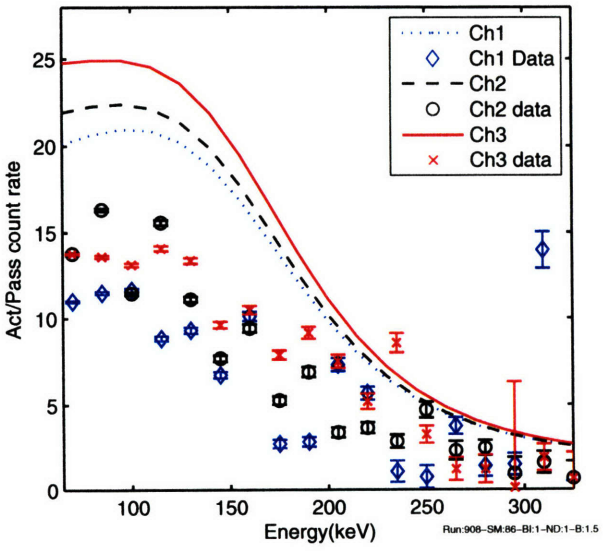

Figure 5-11: AORSA/CQL3D and experimental active/passive count rate. The simulated results are from the $N_\phi = \pm 10$ average case. The error bars are based on counting statistics only.

the shape of the simulated spectra at the higher energies will change if a different boron impurity density is used, as discussed in the previous chapter. On the other hand, qualitatively, the real spectra seem to be well matched by the synthetic results at these higher energies with the estimated 1.5% boron impurity density.

In terms of count rates, Figure 5-11 gives the active/passive count rate ratio for both the $N_\phi = \pm 10$ synthetic spectra and the data. The known toroidal tilt of $\sim$1 cm and finite toroidal aperture size ($\sim$2 cm) discussed in the last chapter are not accounted for in this synthetic diagnostic. Accounting for these details might lower the synthetic active/passive count rate ratio by $\sim$10-15%. Without these effects, the real active/passive count rate ratio is $\sim$60% of the predicted as indicated in the figure.

Various possibilities exist to resolve this count rate discrepancy. First, because the background neutral density rises rapidly with r/a and the beam related neutral donors decreases with r/a, a shift of a couple of centimeters outward in Z for the spatial location of the simulated minority distribution would lower the synthetic active/passive count rate ratio noticeably. This would probably occur if spatial diffusion is accounted for. Also, the 1-D FRANTIC neutral density model might not be adequate for this sort of detailed comparison; for example, the neutral density is typically not a flux surface function. Orbit effects might be important again due to the very small but finite $v_\parallel$ that the sightlines can accept; in other words the fast ions might be experiencing a region of higher background neutral density during passive CX then calculated since the fast ions do not have to be strictly at their turning point for the detectors to see them. Another possible explanation might be the DNB neutralizer not reaching steady-state, which would result in lower neutral beam current than expected. However, this is at best a $\sim$10% effect since other checks are in place to ensure that the neutralizer is operating above a $\sim$80% efficiency[53]. Lastly, the simple halo model employed could have simply overestimated the halo densities. In general, a complete model for these neutrals and electron donors is very complicated as the full 3-D geometry of the tokamak must be taken into account, since neither the beam or the background neutrals are flux surface quantities. This type of code is not available currently.

In whole, the effective temperatures of the spectra are relatively unaffected by this modest count rate discrepancy. This is because the shape of $F(E)$ does not explicitly depend on the ratio of beam to background neutral density. In both passive and active CX, the absolute hydrogen neutral density simply determines when HL boron impurity CX becomes important. The shape of the passive CX spectra, as discussed, is more affected by this boron impurity CX since most of the active CX spectra is

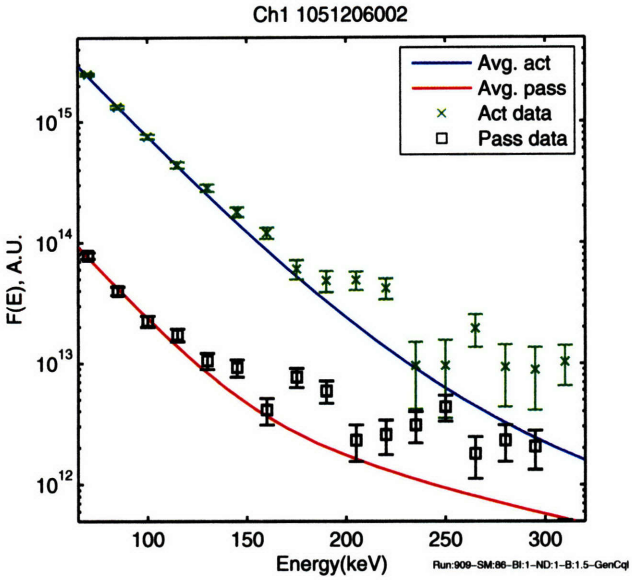

Figure 5-12: Ch1 GENRAY/CQL3D synthetic diagnostic results assuming a 1.5% boron impurity. Both the active and passive CX are shown along with the simulated spectra. The spectra are normalized to the first CNPA data point for clarity. In the legend, 'act' and 'pass' stand for active and passive CX respectively. The error bars are based on counting statistics only.

dominated by halo and third beam component neutrals.

It must be stated in general that this preliminary comparison is reasonably good. It suggests that poor wave focusing and preferential heating of trapped minority ions are the primary physics responsible for the off-axis peaking behavior, and not spatial diffusion. This analysis also validates the off-axis heating and temperature results from the last chapter. For contrast, Figures 5-12 to 5-16 show the same synthetic diagnostic calculations for minority distributions from GENRAY/CQL3D. This code predicts a power absorption of ~91%, similar to the results from TORIC/FPPRF and AORSA/CQL3D. As stated, the use of the GENRAY ray tracing code results in significant power deposited at $r/a = 0$, shown in Figures 5-17 and 5-18. Although the spectra comparison for the Ch1 and Ch2 data is reasonable, the large on-axis fast ion temperature makes the Ch3 and Ch4 synthetic spectra too energetic. To note, the decent temperature comparisons for Ch1 and Ch2 are not unexpected, as Figure 5-17 shows that the effective flux surface averaged temperatures at $r/a > 0.15$ for the GENRAY/CQL3D case are comparable with the results from AORSA/CQL3D. The main difference is again the large on-axis temperatures which dominantly affects the channels with viewing cones intercepting that region. For the count rate comparison,

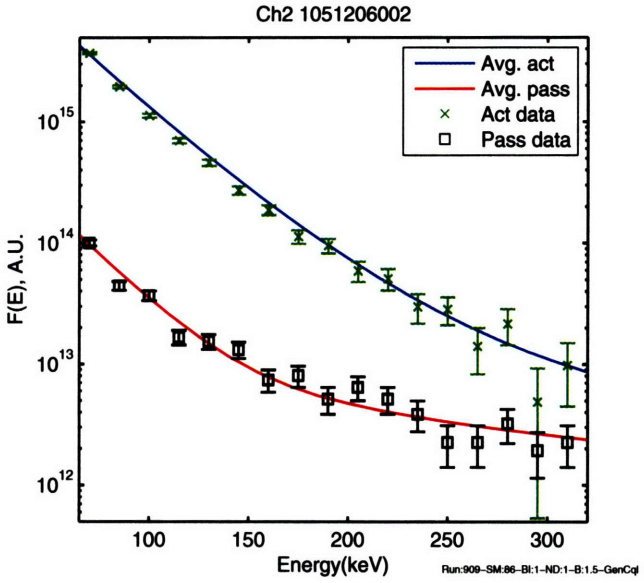

Figure 5-13: Ch2 GENRAY/CQL3D synthetic diagnostic results assuming a 1.5% boron impurity. Both the active and passive CX are shown along with the simulated spectra. The spectra are normalized to the first CNPA data point for clarity. In the legend, 'act' and 'pass' stand for active and passive CX respectively. The error bars are based on counting statistics only.

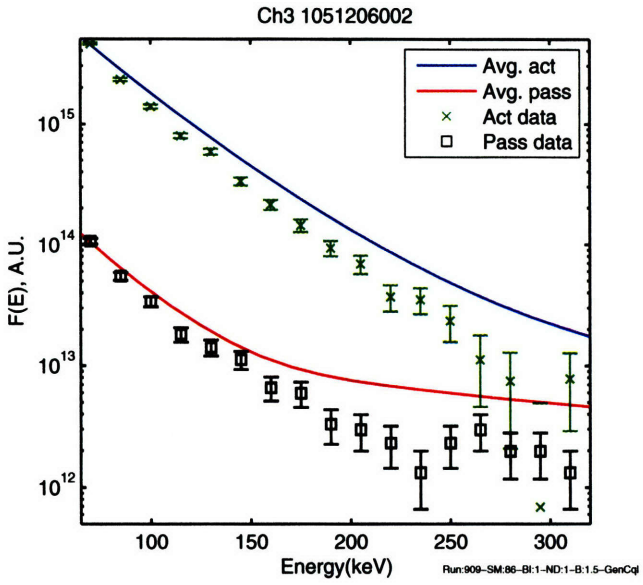

Figure 5-14: Ch3 GENRAY/CQL3D synthetic diagnostic results assuming a 1.5% boron impurity. Both the active and passive CX are shown along with the simulated spectra. The spectra are normalized to the first CNPA data point for clarity. In the legend, 'act' and 'pass' stand for active and passive CX respectively. The error bars are based on counting statistics only.

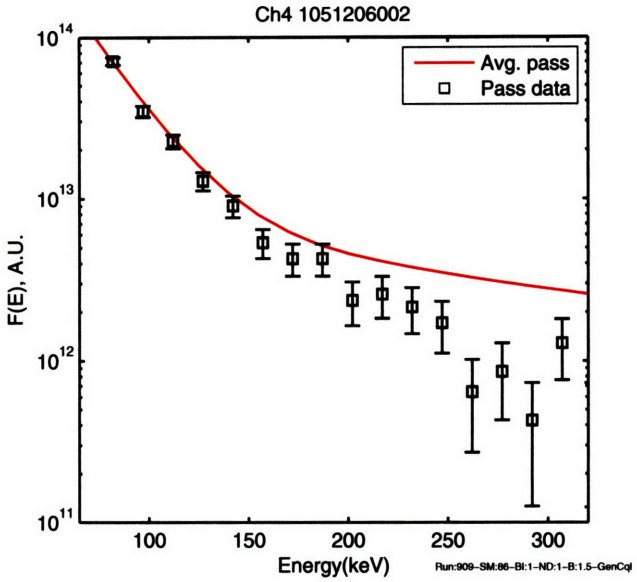

Figure 5-15: Ch4 GENRAY/CQL3D synthetic diagnostic results assuming a 1.5% boron impurity. The passive CX are shown along with the simulated spectra. The spectra are normalized to the first CNPA data point for clarity. In the legend, 'pass' stand for passive CX. The error bars are based on counting statistics only.

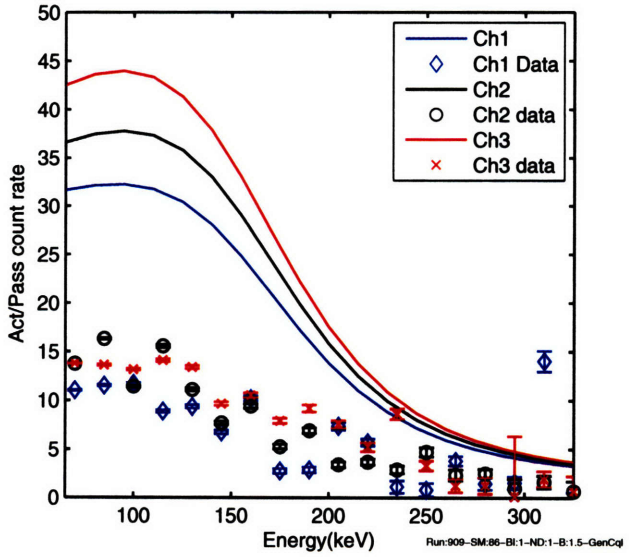

Figure 5-16: GENRAY/CQL3D and experimental active/passive count rate. The error bars are based on counting statistics only.

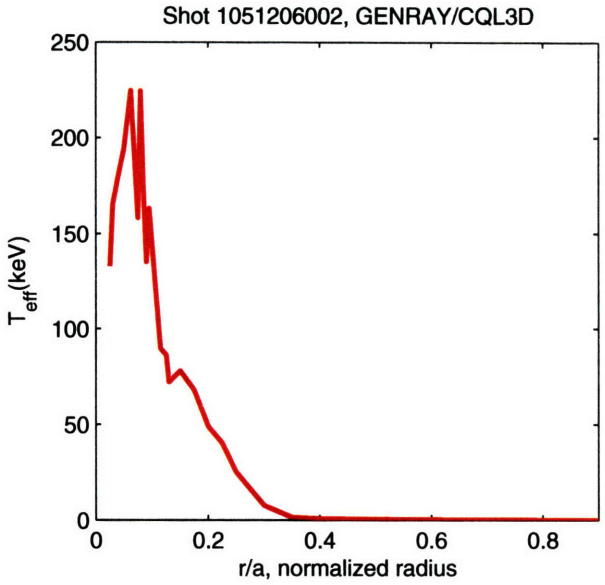

Figure 5-17: GENRAY/CQL3D flux surface averaged temperature profile for shot 1051206002.

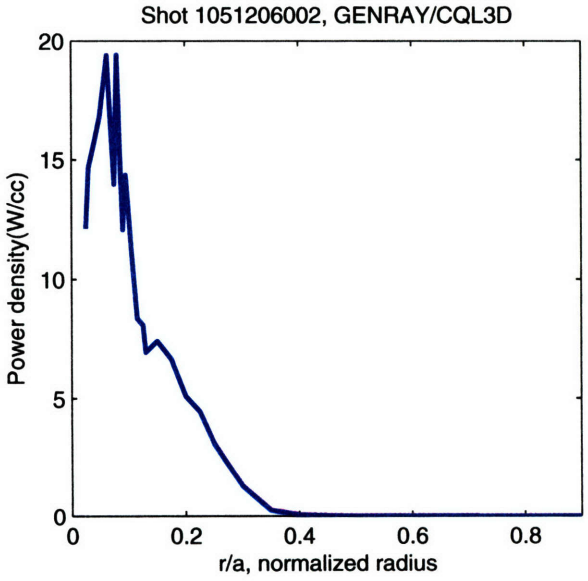

Figure 5-18: GENRAY/CQL3D RF flux surface averaged power deposition profile for shot 1051206002.

the general shift of the minority distributions closer to $r/a = 0$ results in a predicted active/passive ratio ~3 times higher than the measured one.

5.4 Conclusion

A synthetic diagnostic for both active and passive CX analysis is implemented for CQL3D. Using this simulated diagnostic, preliminary results from the new FW/FP AORSA/CQL3D code are compared with CNPA data for shot 1051206002. Reasonable agreement is found for the shape of the spectra, but moderate discrepancies are encountered for the active/passive CX count rate. Including spatial diffusion effects should improve this count rate comparison. Several other possibilities are also proposed to resolved these differences. In contrast, significantly larger differences are found from a comparison of the CNPA data with synthetic diagnostic calculations based on GENRAY/CQL3D. Overall, these preliminary results are encouraging and show that the use of complex FW/FP coupled codes such as AORSA/CQL3D is required to simulate these energetic populations in Alcator C-Mod with some degree of accuracy. Lastly, these calculations support the off-axis heating conclusions and temperature measurements of the previous chapter.

Chapter 6

Conclusions and Future Work

6.1 Summary

The primary focus of this thesis work is the measurement and analysis of energetic minority protons created from ICRF heating in the Alcator C-Mod tokamak. The core minority proton temperature and phase-space anisotropy are directly measured for the first time in Alcator C-Mod through a new neutral particle analyzer diagnostic. The minority temperatures are found to scale approximately with the Stix parameter in a series of low density discharges. Although the heating resonance of all the studied plasmas is on-axis, the minority protons for all of these shots are peaked away from r/a=0, in contrast to what is typically assumed for discharges on Alcator C-Mod. This is independently confirmed with estimates of the r/a=0 minority proton temperature using a sawteeth re-heat analysis. Detailed comparisons of these experimental results with several leading simulation packages found that only a correctly coupled full-wave/Fokker-Planck solver such as AORSA/CQL3D can reproduce the experimental features with accuracy. This off-axis heating result has been seen on other machines, noticeably PLT, but this is the first time that both concrete experimental and simulation results are available for comparison. In whole, the thesis is comprised of both extensive new experimental and numerical work, summarized in detail below.

Experimentally, a new multi-channel Compact Neutral Particle Analyzer is designed, constructed, and implemented on Alcator C-Mod. This diagnostic successfully measured directly, for the first time, the core energetic minority proton population. A notable innovation of the CNPA includes the use of fast digitization techniques to replace traditional real-time pulse-height analysis systems typically employed. These techniques permit much greater flexibility in the operation of the diagnostic and elim-

inate errors in the pulse height data that can affect traditional systems. An example of these errors are shifts in the baseline of shaping amplifiers that are easily corrected when the fast digitization techniques are used.

In terms of diagnostic physics, a simple model with impurity CX applied by the JET, JT-60U, and TFTR teams for analyzing their NPA data is extensively modified for use with the CNPA data set. This modified model includes detailed beam profiles and halo CX. These modifications permit the peak minority proton temperature to be estimated and its spatial location to be inferred via a comparison of the active and passive CX count rates. Lastly, hydrogen-like boron is identified as a key electron donor in the high energy range of the CNPA.

Application of this modified simple model to the CNPA data set shows that the minority proton temperatures scale approximately with the Stix parameter, and that these fast protons are peaked off-axis even for an on-axis heating resonance. This off-axis peaking is a result of the fact that ICRF waves heat ions in $v_\perp$ dominantly, which tends to create trapped minority ions with banana tips close to the heating resonance, and poor wave focusing. Moreover, trapped ions are also preferentially heated. These effects combine to drive the power deposition away from $r/a \sim 0$ because it is very difficult to trap ions near $r/a \sim 0$. The experimental measurements are compared with numerical simulation results from TORIC5/FPPRF, AORSA/CQL3D, and GENRAY/CQL3D. Comparisons of the experimental flux surface averaged temperatures and spatial location with TRANSP's TORIC5/FPPRF are poor possibly because of the use of equivalent Maxwellian distributions in the TORIC5 full-wave solver. The AORSA/CQL3D comparisons, on the other hand, are good because the full 2-D fast proton distribution is kept intact between the full-wave and Fokker-Planck solver during each iteration of the code. Keeping track of the 2-D minority distribution rigorously allows resonance localization of the minority ions to occur; this permits the hollow power deposition and minority temperature profiles to be simulated properly. Going further, comprehensive comparisons of the CNPA experimental spectra with simulation results from AORSA/CQL3D and GENRAY/CQL3D are done using a new synthetic diagnostic written for this thesis. The AORSA/CQL3D synthetic spectra show reasonable agreement with the CNPA data. Results from the GENRAY/CQL3D comparison show noticeable disagreement. This disagreement is attributed to the use of ray-tracing techniques in GENRAY which tends to focus ICRF power at $r/a \sim 0$. In closing, the AORSA/CQL3D code is most able to reproduce the minority proton features seen by the CNPA, and validates the use of the modified simple model for interpreting the CNPA data.

Overall, these experimental and theoretical studies form a solid foundation for the examination of even more complex wave-energetic particle interactions on Alcator C-Mod, such as due to toroidal Alfvén eigenmodes.

6.2 Future Work

With the feasibility of measuring energetic ICRF heated minority protons established on Alcator C-Mod, several possible avenues of new research can be taken. In this section, upgrades to the CNPA diagnostic and modeling are discussed, along with some potential future experiments.

In terms of hardware and diagnostic engineering, various upgrades to the diagnostic should be implemented. The addition of vertical channels spanning the entire plasma major radius should be considered. This would permit extensive analysis of discharges with off-axis resonance heating layers. However, this upgrade would require extensive re-engineering of the F-Port Top diagnostic flange and modifications to the F-Port Top CXRS periscope which is currently occupying the outboard portion of the port. Another difficult but potentially rewarding upgrade could be a detector array with a tangential view of the DNB. A simpler improvement involves extending the energy range of the diagnostic by using shaping amplifiers that have a higher voltage rail than the current HXR shaping amplifiers. The lower energy range can be extended by using thinner foils if desired; experimental study is needed to verify an optimum thickness. Additionally, the PHA procedure could be rewritten to incorporate detailed gaussian fitting of each pulse to improve energy resolution and to recover piled-up pulses. Similarly, the digitizers can be operated at faster frequencies for smoother voltage outputs to facilitate detailed fitting. Outside of the CNPA diagnostic, more accurate impurity density measurements are needed in general. At a minimum, the CXRS diagnostic should be absolutely calibrated so that absolute boron densities can be determined.

From an analysis point of view, the AORSA/CQL3D simulations should be re-run when the AORSA/CQL3D coupling code is modified to handle multiple N_ϕ simultaneously. After this, more shots can be analyzed with the synthetic diagnostic. If possible, a TORIC/CQL3D coupling should be attempted to confirm that proper handling of the distributions between the full-wave and Fokker-Planck solver results in off-axis peaking of the minority protons, and to study the effect of retaining all the FLR terms in the dielectic tensor. Lastly, orbit effects and spatial diffusion could be included in the analysis by using the Monte-Carlo TORIC/ORBIT-RF code[54]. In

the general sense, an accurate FW/FP code is important for experiments that depend on details of the fast minority species because the measurement is quite difficult.

Experimentally, more dedicated plasma time is required with the new long pulse DNB to extend the basic scaling study discussed in this thesis. The operating space for Alcator C-Mod is unique and hence this scaling study should be continued; it is easy on Alcator C-Mod to create both very energetic or very weak minority distributions in reactor-relevant plasma regimes. The heating efficiency as a function of current could be studied to confirm that fast proton orbit losses are minimal. Another experiment related to the plasma current is the effect of sawteeth crashes on the fast protons; some very preliminary CNPA data suggest that the effect is noticeable for large sawteeth. However, no correlation between sawteeth and the CNPA count rates are found for the 600 kA discharges in this thesis. Second harmonic proton heating could be studied by lowering the toroidal field; some passive second harmonic CNPA data are already available for shot date 1050726, or July 26th, 2005. Lastly, experiments involving toroidal Alfvén eigenmodes should be pursued with the CNPA diagnostic to study the interaction of these eigenmodes with energetic minority protons.

Appendix A

Calibration of the Alcator C-Mod CNPA via Rutherford scattering of deuterons

A.1 Introduction

Calibration of the Alcator C-Mod CNPA 3-channel F-Top array was accomplished via detection of Rutherford scattered deuterons from a 500 $\AA$ thick gold foil in the 40-142 keV energy range. Rutherford scattering was used in order to limit the particle flux to the CNPA. The calibration was performed at the MIT PSFC accelerator facility operated by the HEDP group. The resultant calibration is within ~3% of the previous 15-60 keV CNPA calibration which used the Alcator C-Mod diagnostic neutral beam and an Am^{241} X-ray source.

A.2 Experimental Timeline and Setup

The calibration experiment was performed over a period of three days, from April 24-26, 2006. The setup of the experiment is illustrated in Figures A-1, A-2, and A-3.

The first two run days consisted of characterizing the backscatter from the beam using a standard Ortec ion-implanted silicon detector apertured to simulate a ~1 mm^2 CNPA detector. Both the HEDP group's Erbium target and a gold foil were tested as the beam target in order to determine an optimum backscatter for calibration. The gold foil produced a relatively sharp peak consistent with scattering theory. Hence, the CNPA was installed on the third day and a gold foil was used as the backscatter

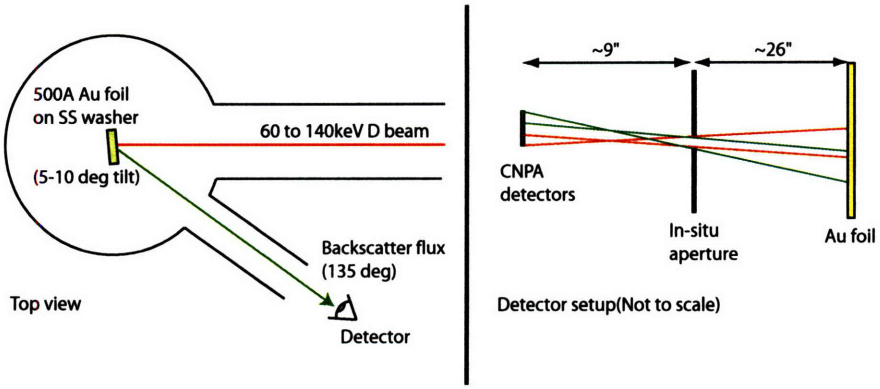

Figure A-1: Left: Experiment schematic setup. The backscatter from a thick Erbium target was also tested. Right: CNPA detector setup for the calibration. The detector sightlines were configured to sweep the foil and washer vertically, starting from the center and traversing downwards. The three adjoining $\sim$1 mm^2 square detectors and in-situ aperture are exaggerated for clarity. The top and bottom detector sightlines are shown.

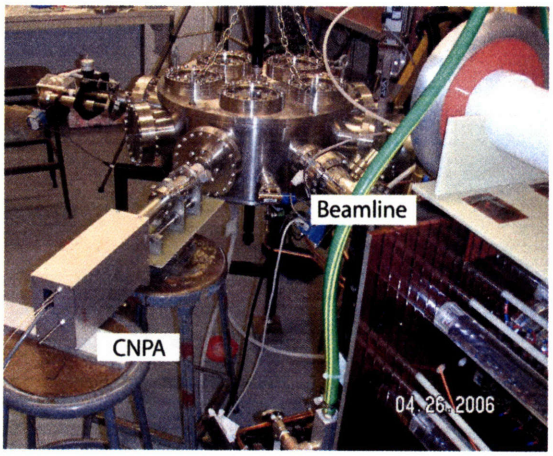

Figure A-2: External view of the accelerator facility. The CNPA is mounted on the port located at the left of the beamline. The micrometer before the bellows section on the CNPA controls the in-situ aperture.

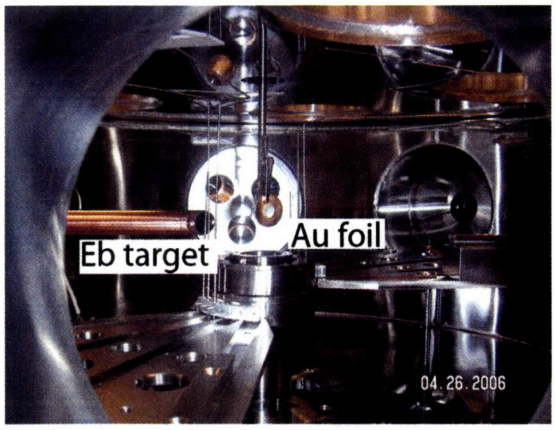

Figure A-3: View of the internal beam chamber through the diagnostic port on the left of the beam. The gold foil is suspended on a nickel mesh and covers a standard washer. The washer is secured by a stainless steel alligator clip mounted on a linear motion feedthrough which permits the foil to traverse vertically. The retractable Erbium target is also shown.

target. The 1550$\mathring{A}$ Al protective foil normally in front of the CNPA detector F-Top array was removed. Deuterium beam energies from 60-142 keV were used.

The 4th channel of the CNPA, which is not part of the F-top array, is calibrated using a standard alpha source. That calibration is not discussed in this appendix.

The rest of this document summarizes the physics involved, the backscattered data, and the CNPA calibration results.

A.3 Rutherford Scattering in a Finite Thickness Target and Experimental Model

In this section, the theory behind Rutherford scattering is given, and its application to the CNPA calibration is discussed.

From Krane[55], the Rutherford differential cross section for a light beam ion elastically scattering from a heavy stationary target is:

$$\frac{d\sigma}{d\Omega} = \left(\frac{zZe^2}{16\pi\epsilon_0 E_b}\right)^2 \frac{1}{\sin^4\frac{\theta}{2}} \tag{A.1}$$

where z is the charge of the incident ion and Z the target, E_b is the beam energy, and θ the scattering angle.

From conservation of momentum and energy, the energy of the scattered beam

ion after the collision is[56]:

$$E_s = \frac{E_b}{(\frac{A_T}{A_b}+1)^2}\left[\cos(\theta) + \sqrt{\left(\frac{A_T}{A_b}\right)^2 - \sin^2\theta}\right]^2 \tag{A.2}$$

where A_T is the atomic number of the target and A_b the atomic number of the beam.

For a foil that is non-negligibly thick in terms of beam and backscatter ion energy attenuation, a relation involving equation A.1 and A.2 that also accounts for the change in ion energy is needed to predict the absolute flux to a given detector. Assuming the variation of θ over the detector viewing solid angle is small, the beam and backscatter ions remain collimated and mono-energetic as they slow down, and no significant total beam ion losses through nuclear or backscattering reactions, the number of backscatter particles to a detector for a dx thick foil slice at a specified θ is:

$$F(x)dx = 4\pi n_b v_b n_T \frac{d\sigma}{d\Omega}(E_b(x))A\Omega dx \tag{A.3}$$

where n_b and v_b are the density of beam ions and their velocity before impact, n_T the density of the target, $E_b(x)$ the energy of the beam as a function of foil depth, and $A\Omega$ the etendué of the detector. Here, $x = 0$ corresponds to the front of the foil. A separate calculation using the SRIM[34] code is used to determine $E_b(x)$.

Stated in another way, the model assumes that each of the dx slices in the foil emit a certain number of particles to the detector at a sharp specific energy.

The energy of the particles hitting the detector from the slice in equation A.3 can be determined via additional SRIM calculations, or approximated as:

$$E_d(x) = E_s(E_b(x)) - \frac{(E_b(0) - E_b(x))}{\cos\theta'} \tag{A.4}$$

θ' is the nearest angle between the beam and the sightline, or $\pi - \theta$. This form of $E_d(x)$ assumes that the backscattered particle experiences the same energy lost coming back out of the foil (scaled by an apparent thickness) as it did when it was first shot in. When compared with detailed SRIM calculations, the above approximation has less than a $\sim 10\%$ error for a foil that causes a $\sim 20\%$ energy loss from the initial beam. The approximation is good at the lowest energy of the calibration experiment, 60keV, and excellent at the higher energies, where the beam energy lost from slowing down in the 500Å Au foil becomes less than $\sim 10\%$. Moreover, for these calibration experiments, the detailed SRIM based calculations give E_d's that are typically only

1-3 keV less than the E_d's estimated from equation A.4.

The constant θ approximation should also be excellent for the collimated sightlines in these experiments, since θ varies by less than $\sim$1 deg over the viewing solid angles. Additionally, if only the relative intensity as a function of energy is required, only the θ dependence in E_s matters. The θ dependence of E_s is weaker than the differential scattering cross section θ dependence. Hence, for these experiments, a constant θ of $\sim$135 deg is assumed. Note that θ is defined relative to the beam, not the target.

Lastly, the sharp range assumption is adequate since ions experience continuous slowing down in the target via ion-electron Coulomb collisions which result in an average energy loss as a function of target depth with small phase-space and real-space spread. For example, the SRIM code shows that a 60 keV D beam traversing a 500 Å Au foil slows to 52.7keV with a standard deviation of 2.5 keV.

Putting all this together, qualitatively, the following scenarios emerges. For a light ion beam hitting a heavy target made up of only one element, the detected energy spectrum, $D(E)$, is a sharp peak very close to the beam energy for a negligibly thick target. The peak broadens with increasing target thickness and eventually disappears. This is due to increasing lower energy backscatter which dominates the total spectra because of the $1/E_b^2$ dependence in equation A.1. *This conclusion is independent of the target Z because the backscattering cross section is never large enough to cause significant loss of the beam before it is slowed by the target to less than half its initial energy.* Hence, a very thin foil in terms of beam energy is required for producing a sharp peak for calibration. However, these thin foils are destroyed easily by beam current since they are not supported and can not be cooled.

An alternative is to examine backscatter from a thick heterogenous target composed of a heavy-Z thin front layer and a very thick lower-Z support backing. Specifically, for the CNPA calibration experiments, firing the beam at the 500Å thick gold layer on the rim of the washer produces a useable backscatter peak even though significant lower energy backscatter occurs as the beam stops in the washer. This is due to the fact that the scattering cross section has a Z^2 dependence which results in a larger backscatter flux from the thin gold layer and permits the gold induced backscatter to be easily picked out from the rest of the spectrum.

Note that backscatter of the half and third components of the D beam also occurs, but because their energies and densities are lower to begin with, their Au induced backscatter is typically lost in the lower energy continuum.

Figure A-4 graphically illustrates the qualitative spectra shapes for the different targets discussed.

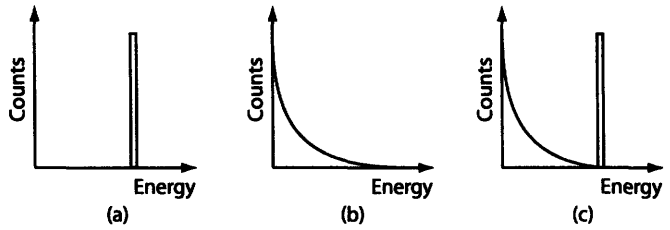

Figure A-4: Qualitative backscatter spectra for different target setups. (A) A negligibly thick homogenous foil. (B) A thick homogenous target. (C) A heterogenous target with a thin heavy-Z layer on top of a thick low-Z layer.

In order to interpret the spectra from the experiment for calibration purposes, what is needed is an accurate estimate of the backscatter peak energy. The absolute intensity is not required. For a finite thickness foil where the scattering cross section is nearly constant, $F(x)$ does not vary much and a flat peak similar to Figure A-4(c) is expected based on the above model, with the edges defined by $E_d(0)$ and $E_d(a)$, where a is the thickness of the foil. The midpoint of the peak is simply the average $E_d(x)$ in the foil. In reality, de-collimation and finite spread of the beam occurs, and the peak can be more Gaussian-shaped. However, the average $E_d(x)$ is still typically an excellent approximation for the peak in these cases.

The following tables summaries $E_b(x)$, $F(x) \propto 1/E_b^2(x)$, $E_d(x)$, and the resultant midpoint energy of the Au backscatter peak used for the CNPA calibration experiments. The SRIM code in Monte-carlo mode is used for $E_b(x)$, and equation A.4 is used for $E_d(x)$. A 2 keV reduction is imposed on the midpoint energies in accordance with the differences between equation A.4 and detailed SRIM calculations as discussed above.

Table A.1: Rutherford scattering energies for different D beam energies and Au foil depths. E_b is the energy of the beam at the specified depth and E_d is the energy of the backscattered particles emitted from that depth. A 2 keV reduction is imposed on the midpoint energies in accordance with the difference between equation A.4 and detailed SRIM calculations.

x(Å)	$E_b(x)$	$1/E_b^2$	$E_d(x)$
60keV D Beam			

Continued on next page...

x(Å)	$E_b(x)$	$1/E_b^2$	$E_d(x)$
0	60.0	2.78E-04	58.0
125	58.2	2.95E-04	53.7
250	56.4	3.14E-04	49.4
375	54.5	3.37E-04	44.9
500	52.7	3.60E-04	40.7
		Midpoint(keV):	**47.3**
80keV D Beam			
0	80.0	1.56E-04	77.3
125	78.0	1.64E-04	72.5
250	75.9	1.74E-04	67.6
375	73.8	1.83E-04	62.7
500	72.0	1.93E-04	58.2
		Midpoint(keV):	**65.7**
100keV D Beam			
0	100.0	1.00E-04	96.6
125	97.8	1.05E-04	91.4
250	95.6	1.09E-04	86.2
375	93.4	1.15E-04	81.0
500	91.3	1.20E-04	76.0
		Midpoint(keV):	**84.3**
120keV D Beam			
0	120.0	6.94E-05	116
125	117.7	7.22E-05	110
250	115.4	7.51E-05	105
375	112.9	7.85E-05	99
500	110.7	8.16E-05	94
		Midpoint(keV):	**103**
140keV D Beam			
0	140.0	5.10E-05	135
125	137.6	5.28E-05	130
250	135.2	5.47E-05	124
375	132.8	5.67E-05	118
500	130.2	5.90E-05	112

Continued on next page...

x(Å)	$E_b(x)$	$1/E_b^2$	$E_d(x)$
		Midpoint(keV):	**122**

Based on these results, the spectra from the backscatter experiments can be used to calibrate the CNPA.

A.4 Experimental Data and CNPA Calibration Spectra

The following pages present the backscatter spectra recorded by the CNPA on the third day of the experiment and the CNPA calibration results based on those spectra. The backscatter spectra from 60, 80, 100, 120, and 142 keV D beams are first shown. A summary of the calibration is then presented.

All the spectra, with the exception of the 142keV point, provide calibration points for all three channels of the CNPA. These are plotted in Figures A-5 to A-9. The beamline is about 1/8" lower than the mid-plane of the target chamber and typically shifted to the right for these shots. The extractor voltage was used to keep the beam at the same location on the washer for each shot, and to quickly lower the current when the 1.5 s long CNPA digitizer shot was completed. This minimizes damage to the foil and fluence to the CNPA. Because of the downshift, Ch3 is nominally viewing nearest to the center of the beam in these shots and have the highest count rates. The 60, 100, and 120 keV data were taken with the in-situ aperture opened to $\sim$1.2 mm^2. This aperture setting corresponds to an $A\Omega$ of $\sim 2\times10^{-11}$m^{2}str and a viewing area of $\sim$5 mm$\times$5 mm on the target. The 80 keV data are a sum of the many shots taken to optimize count rates and aperture opening; the location of the backscatter peaks for these shots do not move with these changes and the sum was done simply to improve statistics. Lastly, the 142 keV data provides a rough calibration point for Ch3 only because the backscatter count rates are low at these high energies. Attempts to take multiple shots at this voltage to increase the available data resulted in trips to the beam.

Note that count rate comparisons between different energies and estimates of the beam density should use Ch3 data, since that sightline is closest to the beam center.

A software discriminator setting of 0.25V and PHA V.4 are used for these spectra; lowering the discriminator does not result in significant changes to the backscatter peaks since the total count rate is less than 100k/s and pile-up effects are still small.

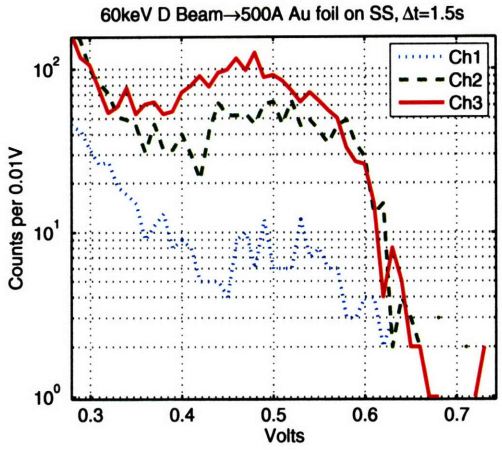

Figure A-5: 60keV D→Au backscatter peaks detected by the CNPA

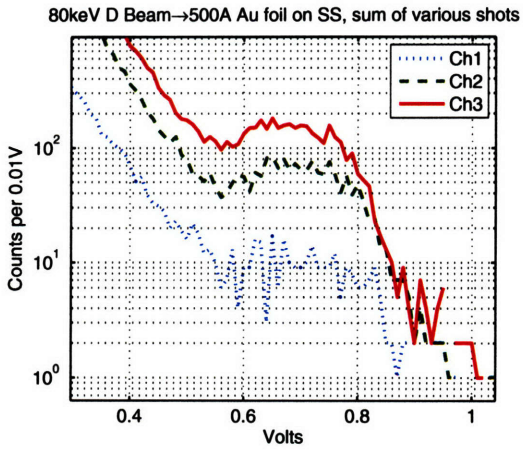

Figure A-6: 80keV D→Au backscatter peaks detected by the CNPA.

To determine the calibration voltage for each backscatter peak for the mid-point energies in table A.1, a linear background subtraction is first performed on the peak and followed by a Gaussian fitting routine. Figure A-10 gives an example of this procedure. Coincidentally, these Gaussian fit derived calibration voltage points are almost always within a few percent of the same points determined from a simple examination of the spectra. This analysis is summarized in table A.2.

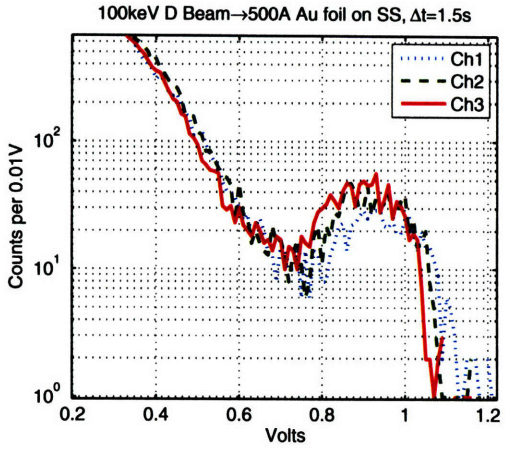

Figure A-7: 100keV D→Au backscatter peaks detected by the CNPA.

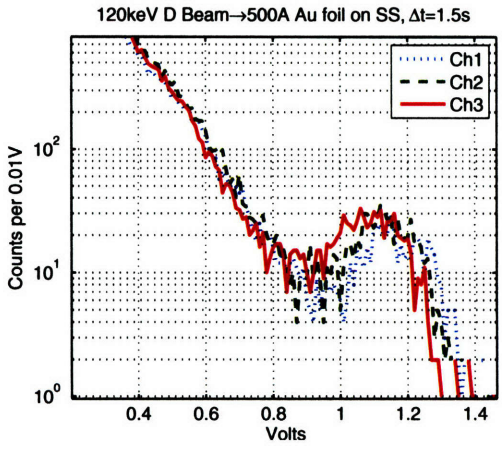

Figure A-8: 120keV D→Au backscatter peaks detected by the CNPA.

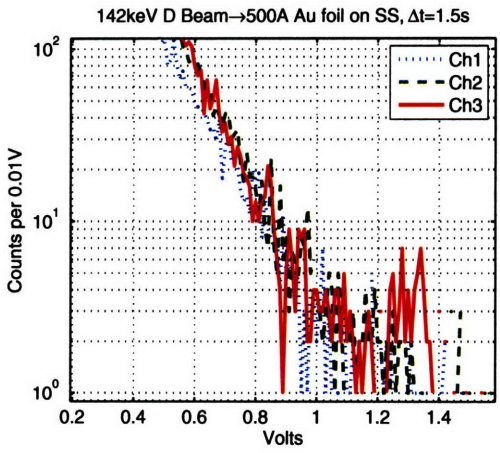

Figure A-9: 142keV D→Au backscatter peaks detected by the CNPA.

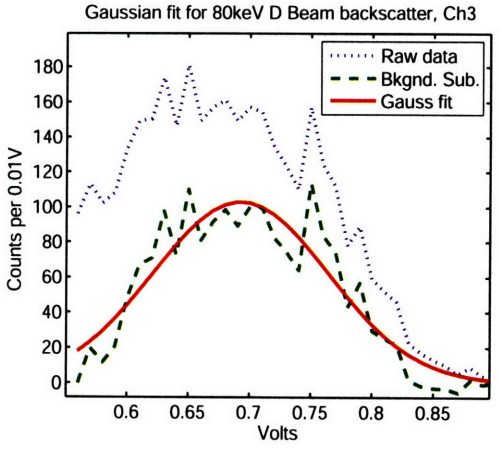

Figure A-10: An example of the background subtraction and Gaussian fitting routine used to determine the mid-point of the backscatter peak.

Table A.2: Summary of available CNPA calibration energy vs. voltage data. The bold points are from the backscatter experiments. The 59.5 keV data are from an Am^{241} X-ray source. Beam-into-gas Alcator C-Mod DNB shots make up the rest of the set. On average, the errors in the energies and voltages are less than 8%.

Energy(keV)	Ch1	Ch2	Ch3
13.4	0.125	0.120	0.112
19.0	n/a	0.172	0.171
24.0	0.220	0.215	0.215
47.3	**0.511**	**0.510**	**0.484**
59.5	0.650	0.640	0.620
65.7	**0.700**	**0.704**	**0.693**
84.3	**0.940**	**0.917**	**0.903**
103	**1.17**	**1.13**	**1.09**
122	**n/a**	**n/a**	**1.32**

The final CNPA calibrations using the data above are plotted in Figures A-11 to A-13. The voltage to keV fits for channel 1 to 3 without the CNPA 1550 $\mathring{A}$ Al protective foil are:

$$V(E)_1 = 0.0117E - 0.0485 \quad \text{(A.5)}$$

$$V(E)_2 = 0.0114E - 0.0412 \quad \text{(A.6)}$$

$$V(E)_3 = 0.0111E - 0.0429 \quad \text{(A.7)}$$

The estimated error is less than 8%.

Additionally, the slopes of the lower energy continuous spectra from these CNPA shots matches well with the slopes from similar shots using the standard Ortec detector.

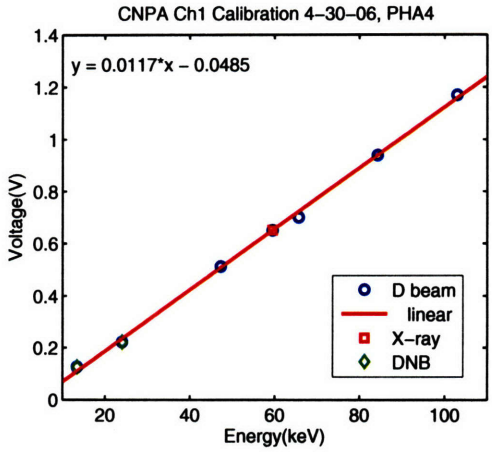

Figure A-11: CNPA energy to voltage response and associated calibration for channel 1.

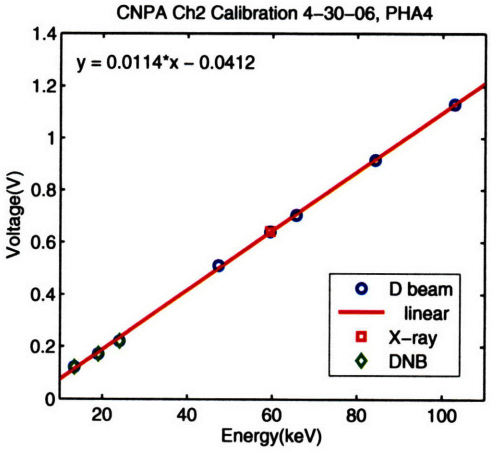

Figure A-12: CNPA energy to voltage response and associated calibration for channel 2.

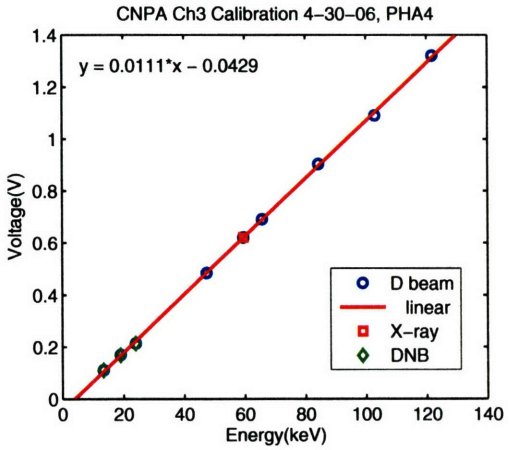

Figure A-13: CNPA energy to voltage response and associated calibration for channel 3.

Appendix B

Derivation of $P(E)$ and its effect on T_{eff}

B.1 The Penetration Factor

Because both the plasma and residue gas neutrals can scatter the CNPA neutral signal, a model is needed to account for this attenuation in order to correctly infer the minority tail distribution.

In the plasma, these neutral stopping reactions include ion impact ionization, electron impact ionization, and charge exchange. These processes can be accounted for by using an effective neutral stopping cross section calculated by Janev[45]. These cross sections include all three reactions, consider excited neutral states, and are functions only of the electron density, electron temperature, Z_{eff}, and relative collisional energy. The dependence on Z_{eff} assumes a carbon impurity. The dependence on the exact impurity species is weak and thus the assumption of a carbon-only impurity is not an issue. Also, the dominant light impurity in Alcator C-Mod is boron and should be closely approximated by carbon. These Janev neutral stopping cross sections are estimated to have errors less than $\sim$ 15% for the CNPA energy range of 75 to 350 keV.

Once the energetic neutral leaves the plasma, they can also be scattered or ionized. The dominant process in this case is neutral impact ionization, which is well characterized by the ion impact ionization cross section and is a function of the relative neutral collisional energy. It is assumed that these ions are deflected out of the CNPA sightline during this ionization process via both angular scattering and Larmor motion. Theoretical calculations and experimental results show that other

elastic and inelastic scattering processes are less than $\sim 10\%$ of the impact ionization cross section. Overall, for edge pressures lower than ~ 0.15 mtorr, $\sim 90\%$ of the core CNPA signal attenuation and scattering is caused by the plasma.

Mathematically, the fraction of energetic neutral particles originating from $\vec{r_0}$ in the plasma and reaching the detector can be determined by the line integral:

$$P(E) = e^{-\int_{\vec{r_0}}^{\vec{r_d}} \frac{d\vec{r}}{\lambda}} \tag{B.1}$$

where $\vec{r_d}$ is the location of the detector, and λ is the mean free path of the neutral signal along the sightline. $P(E)$ is refer to as the penetration factor; dividing the CNPA measured distribution, $F(E)$, by this factor accounts for the effects of signal attenuation.

The attenuation due to residue neutral gas after the energetic neutrals leave the plasma can be explicitly stated for equation B.1 via:

$$P(E) = P_p(E) e^{\frac{-\Delta X_{duct}}{\lambda_n}} \tag{B.2}$$

where $P_p(E)$ now accounts for the attenuation caused by the plasma, and ΔX_{duct} is the length of the vacuum vessel duct that the neutral signal has to traveled through; this is ~ 3.4 m for the vertical CNPA channels and ~ 2 m for the horizontal channel. λ_n is the neutral impact ionization mean free path based on a residue gas density determined from the background neutral pressure and a temperature of ~ 300 K.

For the simple CNPA model, where it is assumed all the energetic neutral signal originates from the center of the plasma, $P_p(E)$ in equation B.2 can be solved either by strict integration which includes plasma profile effects, or estimated quickly using average plasma quantities:

$$P_p(E) = e^{\frac{-\Delta X}{\lambda_p}} \tag{B.3}$$

where ΔX is the distance the signal travels in the plasma, and $\lambda_p = (n_e \sigma_s)^{-1}$, based on averaged plasma quantities. ΔX is simply taken to be the distance from the center to the last closed flux surface. The average density and temperature can be rapidly inferred from either TCI or Thomson measurements. As show later, the dependence on T_e is weak and hence an estimate is adequate. This simple approach permits the penetration correction factor to be determined in-between shots.

Figure B-1 give a comparison of the two methods and show that for the plasmas of interest, the quick approach induced errors of less than 10%. The simple method consistently over-estimates the correction factor for energies greater than ~ 150 keV,

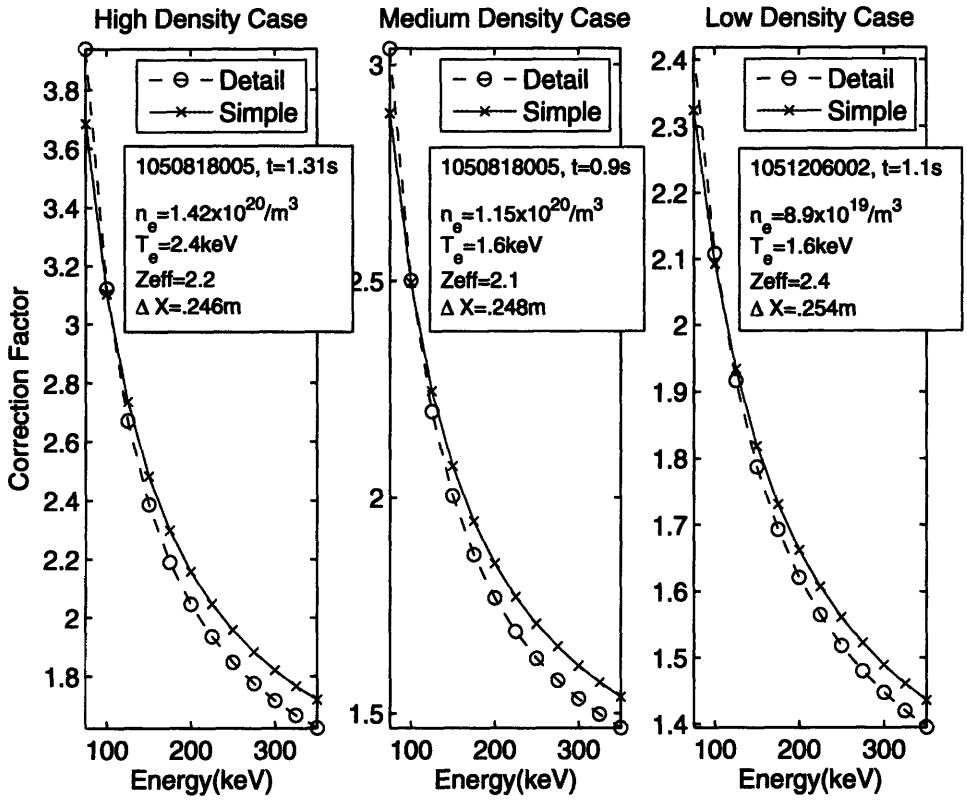

Figure B-1: $P_p(E)^{-1}$ calculated for various L-mode Alcator C-Mod plasmas using both the simple(equation B.3) and detailed numeric approach that accounts for plasma profile details. The parameters taken for equation B.3 are shown for each case; the average density used is derived from TCI measurements. The detail numeric method includes the effects of plasma density, temperature, and Z_{eff} profiles. The 'High-Medium-Low' density labels are relative for the CNPA comparison, since all three plasmas are at the low to medium density range of the Alcator C-Mod operating regime.

while the 75 keV point is consistently under-estimated. An analysis of this $\sim 10\%$ error, given in the next section, show that the fast approach increases the inferred minority temperature by only $\sim 3\% - 6\%$, depending on the exact value of T_p. Hence its use for accurate rapid analysis is justified.

For the detailed synthetic diagnostic implemented in CQL3D, the neutral attenuation is determined rigorously for each energetic neutral emitting grid point.

B.2 Sensitivity of T_p to Errors in $F(E)$

To determine the sensitivity of the extracted minority tail temperature to errors, the effect of altering the CNPA distribution on T_p has to be first estimated. Specifically, the change to the inferred temperature due to a change in the slope of a Maxwellian model is examined via Taylor expansion.

The simple Maxwellian model is defined by:

$$T_p = \frac{\epsilon}{\ln(\alpha)}$$

where $\epsilon = E_2 - E_1$, and E_i indicates the energies used for the Maxwellian fit. $\alpha = \frac{f_1}{f_2}$, where f_1 and f_2 are the distribution values for E_1 and E_2 respectively.

This work is mainly interested in the sensitivity of T_p relative to changes in α due to, for example, errors in the assumed penetration factor. To examine this, a Taylor expansion is performed with respect to α. Also, define $d\alpha = \beta\alpha_0$. β is thus the fractional error in α. Assuming β is small:

$$\Delta T_p(\alpha_0) \approx \frac{-\epsilon\beta}{\ln(\alpha_0)^2}$$

Rearranging further and substituting for α_0:

$$\frac{\Delta T_p}{T_p} \approx \frac{-T_p\beta}{\epsilon}$$

where for a typical CNPA case of $\epsilon = 275$ keV and $T_p = 70$ keV, an approximate temperature change of only 2.5% for a 10% change in α is found. The minority temperature is hence insensitive to minor errors in the distribution.

B.3 Sensitivity of $P(E)$ to errors in bulk plasma parameters

Having determine the approximate temperature sensitivity based on errors in the distribution, errors in plasma parameters that could affect α are now examined. In particular, the change in α due to uncertainties in the densities, temperature, and Z_{eff} taken in the $P(E)$ calculation are reviewed.

In figure B-2, the inverse penetration factor and its variances are examined for a low density Alcator C-Mod plasma. The plot in the upper left shows the inverse penetration factor as a function of energy, and the plasma parameters taken. This is the baseline factor used for comparison. Also plotted is the inverse factor calculated from the detailed penetration model that includes the effect of plasma density, temperature, and Z_{eff} profiles. Clearly again, the quick estimate is excellent and only deviates from the detailed calculation by less than $\sim$ 10%. Therefore, the simple model, based on equation B.3, is used for this sensitivity study.

Because this work is mainly interested in the relative distribution as a function of energy when calculating T_p, the inverse penetration factor can be normalized to the first data point at 75 keV; call this $C_b(E)$ for the baseline case. Now, as different plasma parameters for each case i are varied, different $C_i(E)$ are calculated. Taking the ratio $\gamma_i(E) = C_i(E)/C_b(E)$ then specifically gives the change in α for each variation i. Furthermore, by letting $E_1 = 75$ keV (i.e. first data point, and always = 1 for normalized cases), and $E_2 = 350$ keV, β_i, the fractional error in α for each case i, is then simply equal to $1 - \gamma_i(E_2)$. The contour plots in figure B-2 are these β_i for different Z_{eff}'s, densities, and temperatures. The figure shows that inverse penetration factor is not very sensitive to bulk plasma T_e and Z_{eff} errors, at worst up to $\sim$ 5% for Z_{eff}'s spanning 1.5 to 3.0 and T_e from 1.4 keV to 2 keV. The largest changes are due to errors in density; about $\sim$ 5% for a $\sim$ 10% change in density. The effect of Z_{eff} and temperature changes are minimal as expected, since the dominant neutral stopping processes are charge-exchange and ion impact ionization.

Hence, $\sim$ 10% errors in the density used to calculate $P(E)$ should only result in $\sim 1\% - 2\%$ additional error for T_p.

In summary, the CNPA inferred T_p is not significantly affected by errors in $P(E)$ due to even large uncertainties in the plasma parameters used for the penetration calculation. This is due to both the insensitivity of T_p to $10\% - 20\%$ errors in the experimental distributions, and the insensitivity of $P(E)$ itself.

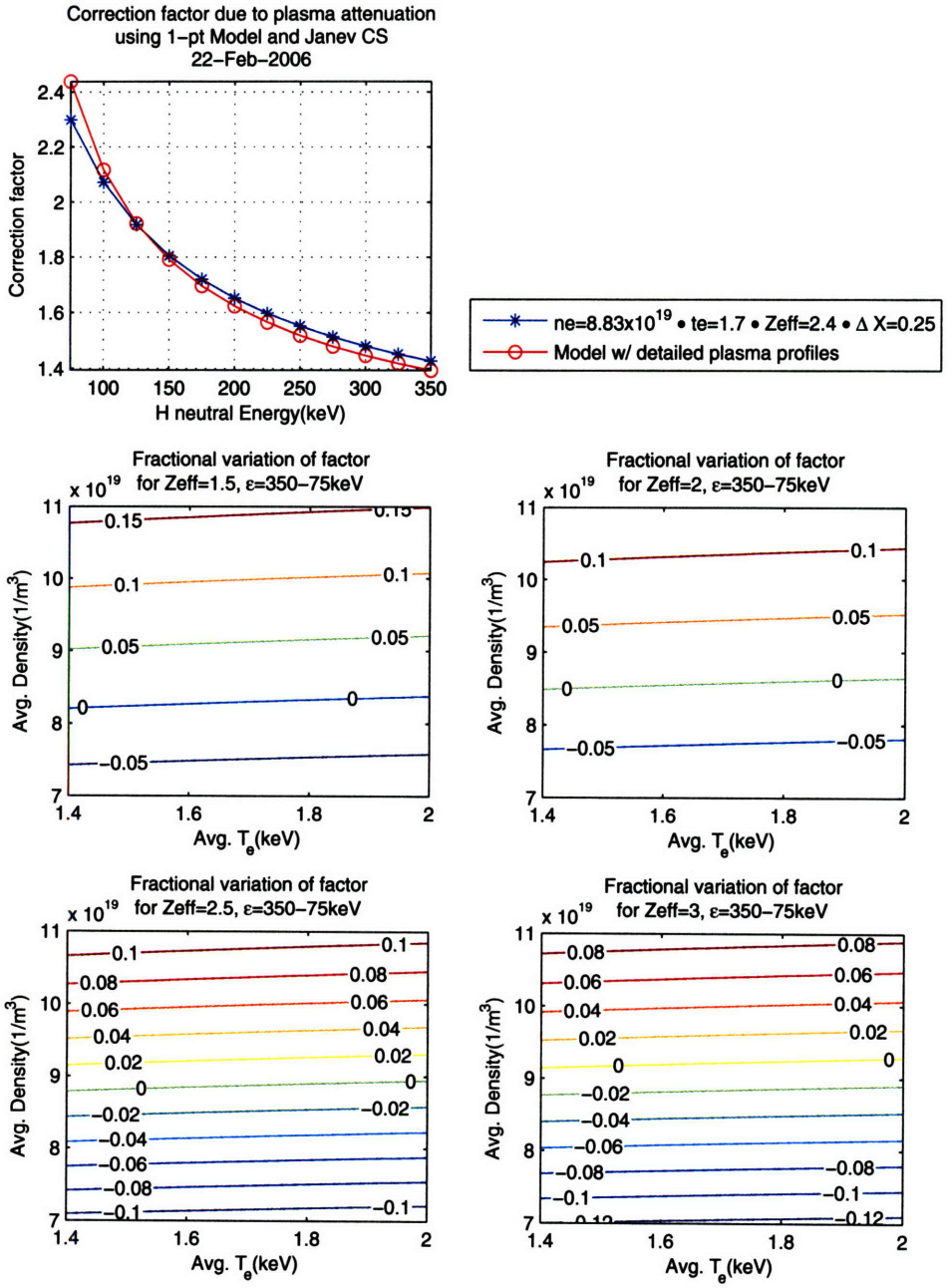

Figure B-2: Inverse penetration, or correction, factor comparison, shot 1051206002, t=1 to 1.5 s. The detailed model is for t=1.09 s only, while the simple model is averaged over t=1 to 1.5 s. The panels show that the dominance dependence is density.

Appendix C

Beam Halo Model

C.1 Introduction

In order to derive accurate minority distributions from CNPA measurements, knowledge of the fast proton neutralizing electron donor is required. In particular, the CX cross section depends on the type of donor and the relative collisional energy. For Alcator C-Mod, confined fast protons are typically in the 0-350 keV range. The CNPA operates in the 75-350 keV bracket. In this energy range, the main CX donors are expected to be hydrogen or deuterium neutrals and hydrogen-like impurities. Specifically, hydrogen-like boron is estimated to be the most significant donor in the ~200-350 keV range, with beam and halo neutrals dominating below 200 keV for active CX experiments. For shots with large He injections or He plasmas, singly ionized He could be the dominant donor in the entire range.

Thus, for active CX neutral particle analysis with the DNB, a beam halo density model is required. This is clearly a beam induced effect that can not be resolved via background subtraction.

For the purposes of this appendix, two halo neutral issues are involved and investigated. First, halo neutrals could directly increase fast proton CX in the relevant energy range of 75 to 200 keV. Second, the fast proton CX in the 200-350 keV range could also indirectly increase because the halo neutrals can create hydrogen-like impurities. On first glance, the first effect should be more important because the B^{5+} electron capture cross section with bulk temperature thermal neutrals is relatively low.

The rest of this appendix consists of sections that resolve these issues in detail; the first gives a simple 1-D diffusion halo neutral model, while the other two examines the results of the model and their implication for the CNPA for a typical low density

L-mode Alcator discharge.

C.2 Diffusion Model for Beam Halos Neutrals

A rate balance for these halo D neutrals, or simply n_0, in the DNB volume is:

$$\frac{\partial n_0}{\partial t} = \sum_{k=1}^{3} \alpha_k - n_0\beta + D_{n_0}\nabla^2 n_0 \tag{C.1}$$

where $\alpha_k = n_i n_{b,k} \langle\sigma v\rangle_{cx,k}$, with n_i corresponding to the local D ion density, $n_{b,k}$ the density of the k^{th} component of the DNB, and $\langle\sigma v\rangle_{cx,k}$ the CX rate. $\beta = n_e \langle\sigma v\rangle_{ei}$ is the electron impact ionization rate per D neutral. The rightmost term corresponds to D neutral losses from transport, modeled through a diffusion coefficient based on CX of these D neutrals with bulk plasma ions. Specifically, CX with bulk ions do not permit net neutral losses but it does result in neutral random walk, assuming the bulk ions are isotropic and at the same temperature. The diffusion coefficient is then $D_{n_0} = k_b T_i / m_d \nu_{cx}$. ν_{cx} here is estimated by $n_i \sigma_{cx}(v_{D,mp}) v_{D,mp}$, where $v_{D,mp}$ is the most probable speed of the bulk D ions based on their temperature. This number typically is slightly lower than the true averaged rate in the ~1-2 keV range. Recombination and D ion impact ionization are negligible compared with the birth and loss rates considered above. D neutral losses through impurity ionization collisions or impurity CX are not included in this simple halo analysis but these should be at best a ~10% effect. Lastly, at densities around $10^{20}/\mathrm{m}^3$, less than ~1% of the DNB is in the n_p=2 state and hence excited DNB neutrals should not significantly affected the rate balance[38]. At most the total beam-bulk plasma CX reactivity would increase by ~5%. These two small neglected effects might also somewhat counterbalance each other.

Because the time scale of interest (~1ms) is much longer than the characteristic time scales in equation C.1 (~ 10 μs), a steady state solution by setting $\frac{\partial n_0}{\partial t} = 0$ is sought. A cylindrical coordinate system with the Z-axis aligned with the radically injected Alcator DNB is first imposed. The r-axis at θ equal to 0 or π in this cylindrical system thus corresponds to the toroidal direction in the tokamak. Therefore, the Z-axis along the beam is the major radius axis of the plasma. See, for example, Figure 4-5. Ignoring transport in the Z-direction and plasma variations in r and θ,

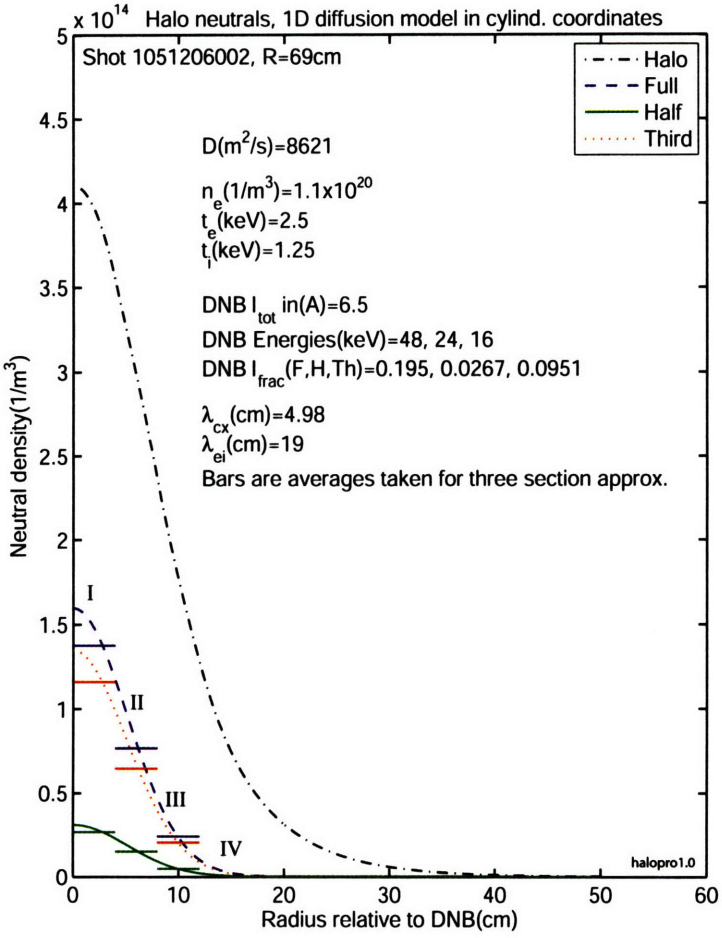

Figure C-1: DNB and halo neutral density profiles for shot 1051206002 at R=69 cm. The Z-axis is aligned along the DNB. For the calculation, each component of the beam is approximated by three regions of constant source density. Correspondingly, these regions from equation C.3 are labeled. The bars overlaying the beam profiles show the constant α_k's taken for the approximation and the thickness of each region. The neutral hydrogen current in particles/sec for each component is given by $\frac{I_{tot} in I_{frac}}{1.6 \times 10^{19}}$, with the dissociation factor and penetration already accounted for. The bulk ion temperature is estimated as half the electron temperature.

equation C.1 for a specified Z point becomes:

$$D_{n_0}\frac{\partial}{r\partial r}(r\frac{\partial n_0}{\partial r}) = n_0\beta - \sum_{k=1}^{3}\alpha_k \tag{C.2}$$

Without the rightmost term, the above equation is simply modified Bessel's equation. The summation terms, if they are arbitrary functions of r, result in an inhomogeneous equation that is not easily solved. In theory an integral can be carried out to resolve equation C.2 for many different types of $\alpha_k(r)$. However, if the α_k's are constants within a specified region, as approximated in Figure C-1 for shot 1051206002, an analytical solution is available for each region. If desired, the regions can be numerous and thin enough to approximate any DNB source profile. However, for the estimates needed here, the three step approximation in the figure is more than adequate for modeling the DNB gaussian-shaped source profile. These gaussian source profiles in the figure are determined by spectroscopic measurements of the DNB component mix at the DNB neutralizer and calculations of the plasma penetrability of those components. Finally, the general neutral halo density solutions for the four regions are:

$$\begin{aligned} n_0(r)_I &= C_1 I_0(\lambda r) + \gamma_I\beta \\ n_0(r)_{II} &= C_2 I_0(\lambda r) + E_2(\lambda r) + \gamma_{II}/\beta \\ n_0(r)_{III} &= C_3 I_0(\lambda r) + E_3(\lambda r) + \gamma_{III}/\beta \\ n_0(r)_{IV} &= E_4 K_0(\lambda r) \end{aligned} \tag{C.3}$$

where I_0 and K_0 are modified bessel functions, and λ is equal to $(\beta/D_{n_0})^{1/2}$. γ_i is $\sum_{k=1}^{3}\alpha_k$ for each region. C_i and E_i are constants that are determined by the boundary conditions between each region. These boundary conditions are $n_0(a)_i = n_0(a)_{i+1}$ and $n_0'(a)_i = n_0'(a)_{i+1}$. In general the bulk plasma based parameters such as β and D_{n_0} are functions of r and θ, but for estimates near the core it is adequate to use averaged values. Keeping these parameters constant also permit the simple analytical solution given by equation C.3.

As shown in Figure C-1, for the examined low density Alcator C-Mod plasma, the thermal halo neutral density is significantly higher than the DNB component densities. Figures C-2 to C-5 illustrate halo density changes due to different bulk plasma densities (n_i ~0.8 to 1.5 $x10^{20}/m^3$) and temperatures (T_e ~2 to 3 keV). The beam deposition profile and fractions are not changed from the default case in

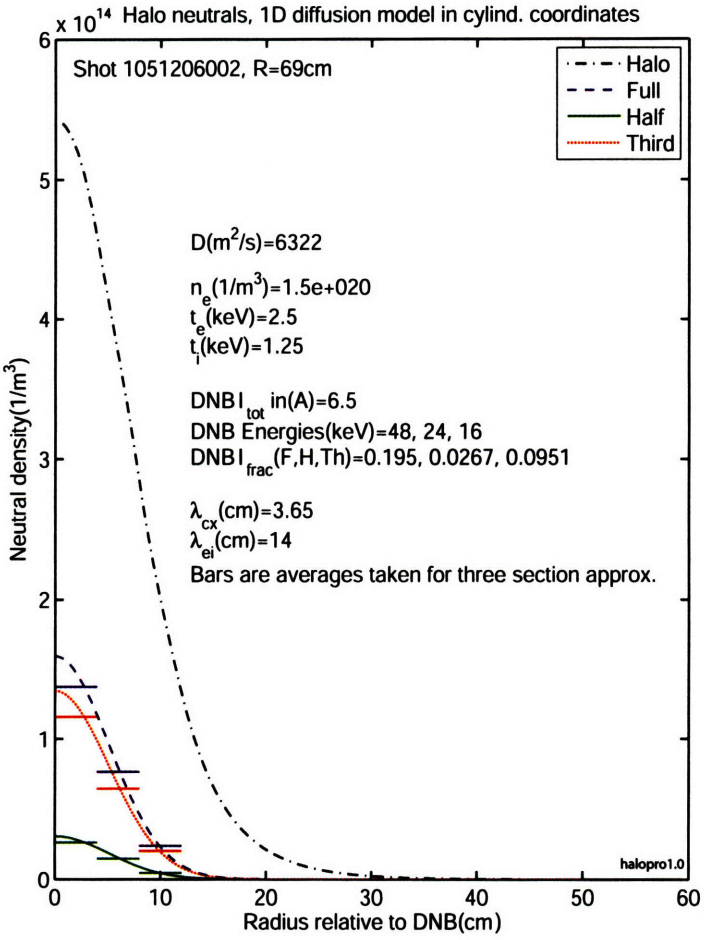

Figure C-2: DNB and halo neutral density profiles for shot 1051206002 at R=69cm. The plasma density has been increased to $1.5 \times 10^{20}/\mathrm{m}^3$ compared with the default case in Figure C-1.

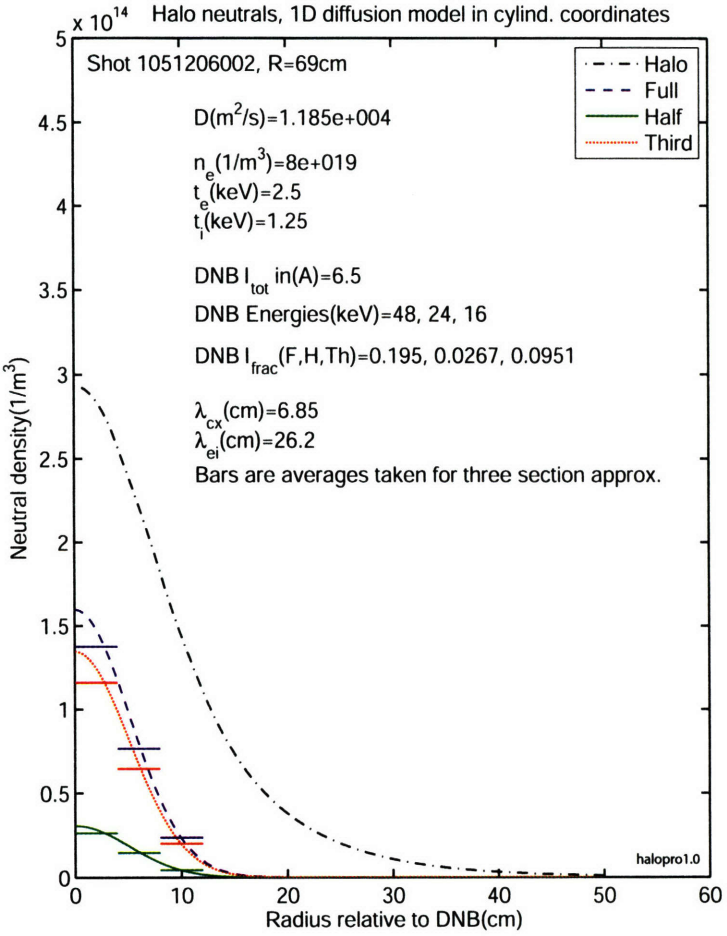

Figure C-3: DNB and halo neutral density profiles for shot 1051206002 at R=69 cm. The plasma density has been decreased to $8 \times 10^{19}/\mathrm{m}^3$ compared with the default case in Figure C-1.

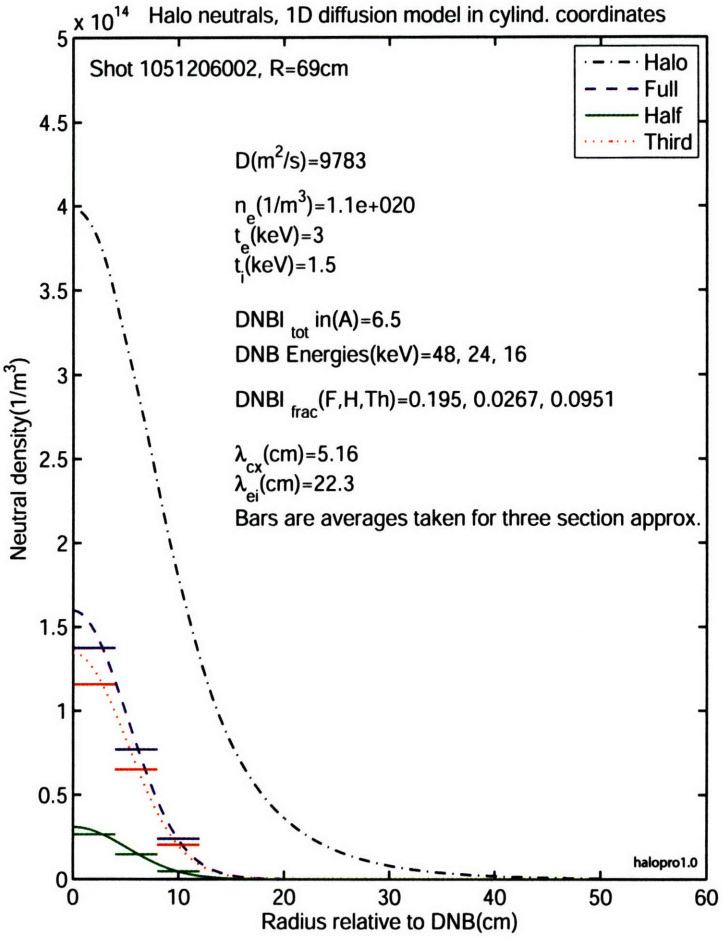

Figure C-4: DNB and halo neutral density profiles for shot 1051206002 at R=69 cm. T_e and T_i have both been increased by 20% compared with the default case in Figure C-1.

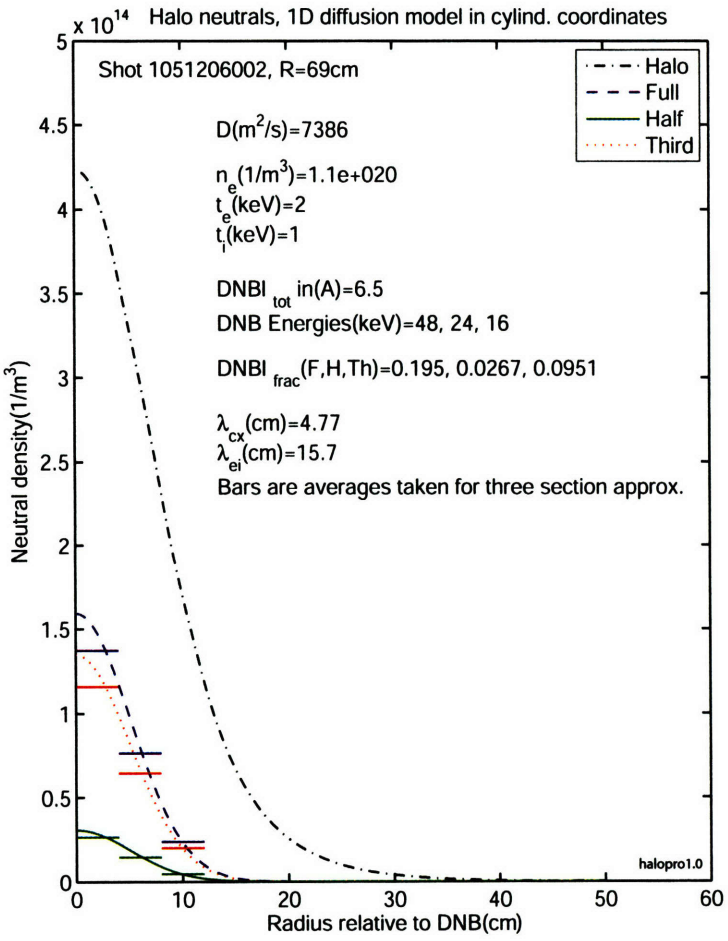

Figure C-5: DNB and halo neutral density profiles for shot 1051206002 at R=69 cm. T_e and T_i have both been decreased by 20% compared with the default case in Figure C-1.

Figure C-1 in order to illustrate the profile dependence on bulk plasma parameters. As expected, the halo profile narrows and peaks with smaller D_{n_0} and via versa. Broadly speaking, lower density plasmas have higher neutral diffusion coefficients, but these greater diffusive losses can be compensated by better penetration of lower energy beam components which increases α_k, and lower electron impact ionization rates. Higher density plasmas evoke the opposite arguments. In terms of temperature changes, similar balancing forces are involved. The electron impact ionization rate increases with decreasing T_e, but D_{n_0} has the opposite dependence. Note that the ion temperature used here is half of the electron temperature; this tends to underestimate the ion temperature noticeably; however, for the illustrative purposes it is an adequate approximation. The real diffusion coefficients based on neutron rate inferred T_i are higher. The beam neutral CX rates and attenuation are weak functions of T_e because they are really determined by the beam neutral velocity. Thus, the DNB component profiles are not affected noticeably by T_e changes. Overall, the qualitative conclusion that the thermal halo neutral population is substantial and possibly dominating for the examined low density Alcator C-Mod plasma is robust and not altered by noticeable plasma parameter changes.

On a broader note, the low density plasma examined above is also characteristic of the type of plasmas on Alcator C-Mod where beam diagnostics can be readily employed because of decent penetration and weaker noise backgrounds. Therefore the effect of a substantial halo neutral population that is also wider than the FWHM of the DNB should be considered for any Alcator C-Mod neutral beam based diagnostic.

C.3 Direct Fast Proton Neutralization from Halo Neutrals

For the CNPA, the effect of halo D neutrals on the CX rate is dominating. This is primarily due to the sightline geometry of the diagnostic. The vertical channels intersect the DNB perpendicularly and have effective fast proton-beam neutral CX rates of $n_b\sigma_{cx}(E_p + E_b)v(E_p + E_b)$, where E_p and E_b are the energies of the fast minority proton and beam neutral respectively. The thermal halo D neutrals on the other hand effectively have $E_b = 0$. In the CNPA energy range of ~75-200 keV before hydrogen-like impurity CX dominates, the proton CX cross section increases rapidly with decreasing collision energy. Hence, thermal D halo neutral CX is significantly greater than direct beam neutral CX per fast proton. Specifically, the magnitude of

fast proton-halo CX is determined via the following equation, which gives the fraction of the fast proton-halo neutral CX rate over the total fast proton CX rate with D and H neutrals as a function of energy for a specified beam radius:

$$f_{cx}^{halo} = \frac{n_0 \sigma_{cx}(E_p) v(E_p)}{n_0 \sigma_{cx}(E_p) v(E_p) + \sum_{i=1}^{3} n_{b,i} \sigma_{cx}(E_p + E_{b,i}) v(E_p + E_{b,i})} \tag{C.4}$$

where the sum in the denominator is taken over all three components of the DNB.

In order to solve equation C.4, a beam radius r must be chosen. The ratio of halo density to full component beam density is typically 2 to 3 at r=0 and increases rapidly pass r=FWHM/2 of the DNB. Figure C-6 give this ratio as a function of r for the profiles in Figure C-1. f_{cx}^{halo} is thus minimum at r=0, and examining it at that point will reveal if halo induced CX is dominant for the whole beam. Furthermore, if only the relative rate of CX is important, assuming only fast proton-halo neutral CX for the cross section will probably not be a bad approximation since the next major contributor to the total CX reaction rate after halo neutrals is from the third energy component of the DNB, which only skew the energy dependence by at most 17 keV. In either case, the CNPA CX calculations are simplified since their dependence on DNB beam details is weak. These issues are illustrated quantitatively in two figures. The first, Figure C-7, plots the terms in the denominator of equation C.4 at r=0 for shot 1051206002 and shows that most of the fast proton neutralization does indeed come from halo neutrals and the third component of the DNB. The second, Figure C-8, graphs equation C.4 and reveals that over the energy range of interest, the halo neutrals contribute more than ~70% to the total fast proton neutralization rate. Practically, assuming fast proton neutralization only from halo neutrals results in less than ~10% systematic error in the derived distribution over the 75-200 keV fast proton energy range. Additionally, this error decreases with increasing beam radius because of the increased halo fraction. Note that again these results will change slightly when higher neutron rate inferred T_i's are used.

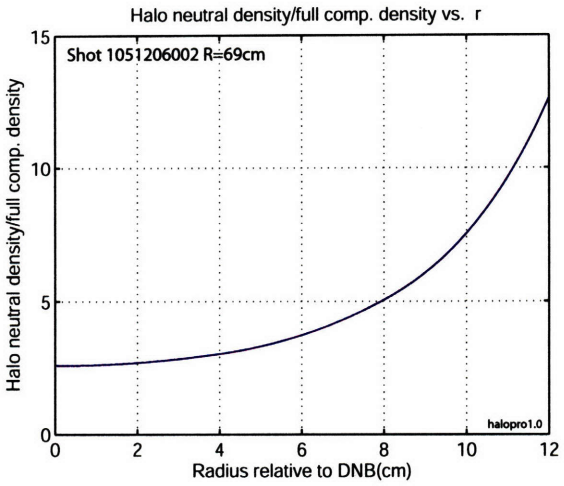

Figure C-6: Calculated halo neutral density divided by DNB full component density for shot 1051206002 vs. beam radius.

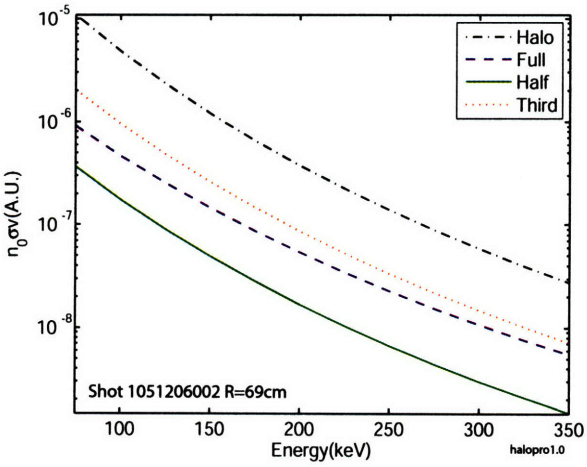

Figure C-7: Plots of the four denominator terms in equation C.4 using the r=0 densities from Figure C-1 vs minority proton energy. Clearly the dominant electron donors are the halo neutrals and third DNB component.

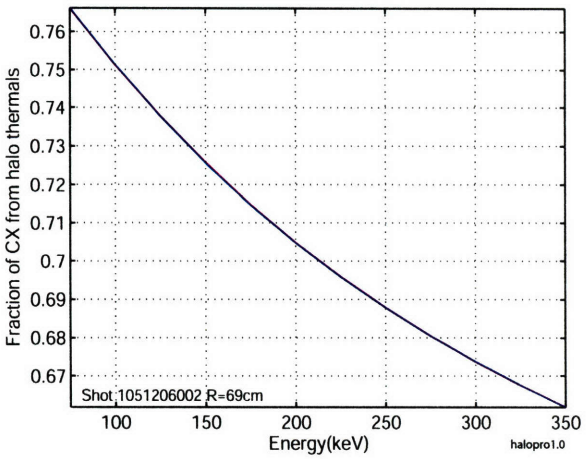

Figure C-8: f_{cx}^{halo} from equation C.4 using the r=0 densities from Figure C-1 vs minority proton energy. In the energy range of ~75 to 200 keV, a relative error of less than ~10% would be incurred in the minority temperature if only halo charge exchange is assumed.

Appendix D

Absolute Calibration of the Alcator C-Mod He-II diode

D.1 Introduction

Estimates of the helium concentration in Alcator C-Mod plasmas are required for effective operation of D(He^3) discharges, and for various analysis such as accurate interpretation of CNPA data.

Different spectroscopic methods of determining the He fraction are available. For example, changes in Z_{eff} can be used to infer a He concentration for strong He puffs. However, this method only works for very strong puffs and could be affected by other impurities. A more accurate method involve measuring helium line emission from the plasma. To that end, a diode detector installed and operated by J. Terry is available which measures the sightline integrated plasma emission in the HeII(4→3, 4686Å) region when the proper filter is installed. The detector is absolutely calibrated in Watts/m^2str and has the same sightline as the Mcpherson XUV spectrometer. The signal consists of both the HeII line emission and the bremmsstrahlung radiation within a ~3nm region of the line. It is dominated by emission from electron-impact excited He^{1+} ions at the edge of the plasma.

In theory, because the detector is absolutely calibrated, the signal can be simulated and an average helium fraction inferred. However, this approach is difficult since it requires getting absolute intensities to match. Without this simulation, the detector can only be used to infer relative He density changes for similar discharges.

However, another type of diode calibration which allows the absolute He fraction to be estimated for different discharges is possible. The He^3 concentration in the core

of the plasma can be calculated via break-in-slope methods during D(He^3) heating. With data covering different types of discharges, these RF-inferred He fractions can be used to calibrate the diode for absolute core He concentration estimates given the right scaling. This assumes that the bremsstrahlung background is first accounted for. The differences between He^3 and He^4 are assumed to be small and hence ignored.

The rest of this appendix summaries this calibration process and the RF inferred n_{He^3}/n_e data used from the 2005 Alcator C-Mod campaign. This helium data is first reviewed and followed by the calibration analysis. It is shown that a $n_{He}/n_e \sim \gamma/n_e^2 T_e^{1.5} Z_{\text{eff}}$ scaling, where γ represents the diode signal in Watts/m^2str, give an approximately correct fit of the data. The scaling assumes the edge He^{+1} density is mainly sustained by a balance between CX of He^{+2} with D neutrals or other non fully stripped ions and electron impact ionization. When core plasma values are used in the scaling, only the LSN and USN data match. However, the use of edge plasma values for the scaling reconciles the diverted data with the inner wall limited data but results in larger scatter. A radiative recombination based scaling is also tested but found to be inadequate. Overall, this CX scaling permits rough helium densities to be inferred using the HeII diode signal.

D.2 RF Inferred n_{He} Data

A total of 51 break-in-slope deduced helium concentration data points, provided by A. Parisot, are available during discharges with the HeII filter on the diode. These involve plasmas from 1050725, 1050728, 1050729, and 1050802. The data set span average densities of ~1 to ~2.5x$10^{20}/m^3$ and T_e from ~1.5 to ~3 keV. Table D.1 and Figure D-2 summaries the available data and associated plasma parameters. A complication with this data set is that these break-in-slope based helium concentration estimates are typically greater than the final helium concentrations extracted from detailed TORIC simulations by ~1 to 3%. This can be taken into account by adjusting the final diode inferred helium fraction with a proportional reduction; for example, a 1% reduction for a ~10% helium plasma scaling to a 3% reduction for a ~30% He discharge. This seems reasonable since it is unlikely for a break-in-slope estimate of 4% to be reduced by TORIC to less than 3.5%.

Figure D-1 illustrates the sightline of the diode for these runs.

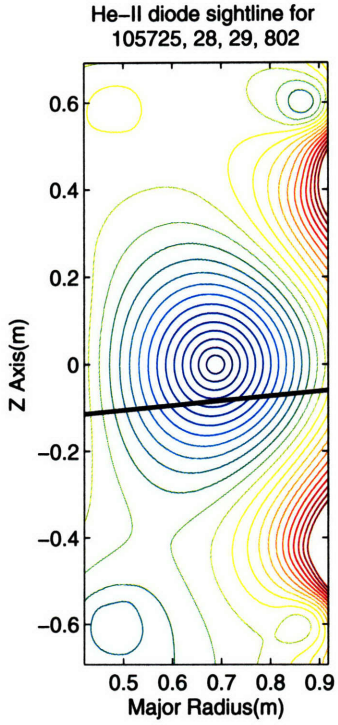

Figure D-1: The HeII diode sightline for shots outlined in table D.1

.

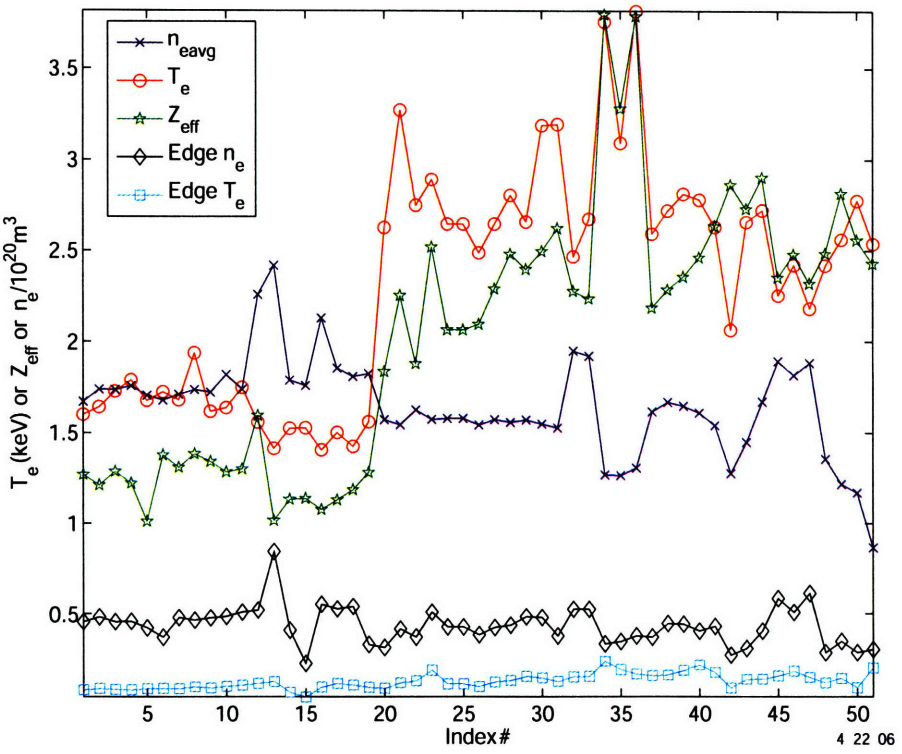

Figure D-2: Some of the plasma parameters for the discharges in table D.1. The values are taken are averaged over 150 ms.

Table D.1: Break-in-slope He^3 concentration estimates for various D(He^3) plasmas during the 2005 campaign(Parisot).

Index	Shot	Puff	Time	Est. He3 conc	Shape/Equil.
1	1050725008	70 ms @ .3 sec	1	6%	LSN
2	1050725011	100 ms @ .3 sec	1	7%	LSN
3	1050725012	120 ms @ .3 sec	0.9	8%	LSN
4	1050725012	120 ms @ .3 sec	1	8-9 %	LSN
5	1050725013	130 ms @ .3 sec	1	7-8 %	LSN
6	1050725015	140 ms @ .3 sec	0.78	8-9 %	LSN
7	1050725015	140 ms @ .3 sec	1	10%	LSN
8	1050725016	200 ms @ .3 sec	0.88	13-14 %	LSN
9	1050725018	100 ms @ .3 sec	1	6-7 %	LSN
10	1050725020	100 ms @ .3 sec	1	8%	LSN
11	1050725022	100 ms @ .3 sec	1	7%	LSN
12	1050725023	100 ms @ .3 sec	1.5	7-8 %	LSN
13	1050728005	200 ms @ .3 sec	1.3	13%	LSN
14	1050728006	200 ms @ .3 sec	0.9	13%	LSN
15	1050728013	150 ms @ .55 sec	0.9	9-10 %	LSN
16	1050728013	150 ms @ .55 sec	1.3	10-11 %	LSN
17	1050728014	150 ms @ .5 sec	1.3	11%	LSN
18	1050728020	200 ms @ .5 sec	1.3	13%	LSN
19	1050728034	200 ms @ .5 sec	1.25	12%	LSN
20	1050729002	250 ms @ .3 sec	0.8	18%	USN
21	1050729002	250 ms @ .3 sec	1.3	18%	USN
22	1050729003	250 ms @ .3 sec	0.8	18%	USN
23	1050729003	250 ms @ .3 sec	1.1	16%	USN
24	1050729004	250 ms @ .3 sec	0.9	18%	USN
25	1050729004	250 ms @ .3 sec	0.9	18%	USN
26	1050729004	250 ms @ .3 sec	1	16%	USN
27	1050729004	250 ms @ .3 sec	1.1	16%	USN
28	1050729004	250 ms @ .3 sec	1.2	16%	USN
29	1050729004	250 ms @ .3 sec	1.3	15%	USN

Continued on next page...

Index	Shot	Puff	Time	Est. He3 conc	Shape/Equil.
30	1050729006	250 ms @ .3 sec	1.1	16%	USN
31	1050729008	250 ms @ .25 sec	1.1	16%	USN
32	1050729015	150 ms @ .2 sec	0.9	18%	IWL
33	1050729016	150 ms @ .2 sec	0.9	17%	IWL
34	1050729019	100 ms @ .2 sec	1.1	19%	IWL
35	1050729020	100 ms @ .2 sec	0.74	18%	IWL
36	1050729020	100 ms @ .2 sec	0.9	19-20 %	IWL
37	1050802004	100 ms @ .2 sec	0.916	15%	IWL
38	1050802005	150 ms @ .2 sec	1.05	23%	IWL
39	1050802005	150 ms @ .2 sec	1.29	20%	IWL
40	1050802006	120 ms @ .2 sec	1.05	18%	IWL
41	1050802006	120 ms @ .2 sec	1.3	18%	IWL
42	1050802008	100 ms @ .2 sec	0.8	15%	IWL
43	1050802018	150 ms @ .2 sec	1.06	18%	IWL
44	1050802019	200 ms @ .2 sec	1.06	23%	IWL
45	1050802023	200 ms @ .2 sec	0.8	25%	IWL
46	1050802023	200 ms @ .2 sec	1.05	25%	IWL
47	1050802023	250 ms @ .2 sec	0.78	27%	IWL
48	1050802026	150 ms @ .2 sec	0.8	30%	USN
49	1050802027	150 ms @ .2 sec	0.8	30%	USN
50	1050802028	150 ms @ .2 sec	0.8	25%	USN

D.3 Calibration

D.3.1 Background Subtraction

Before the HeII diode signal can be used for the scaling study, the visible bremsstrahlung contribution must be subtracted out. This is done by using diode data from a no He shot, such as 1051206002 or 1051104006, and scaling this baseline signal by $n_e^2 Z_{\text{eff}}/T_e^{0.5}$ for each of the shots in table D.1 using core plasma parameter values. The results are plotted in Figure D-3 for scaled bremsstrahlung backgrounds based on shot 1051206002. Coincidentally, the plot shows that there is no HeII signal for index 32-36; these are not used for the scatter plot and fitting process discussed later.

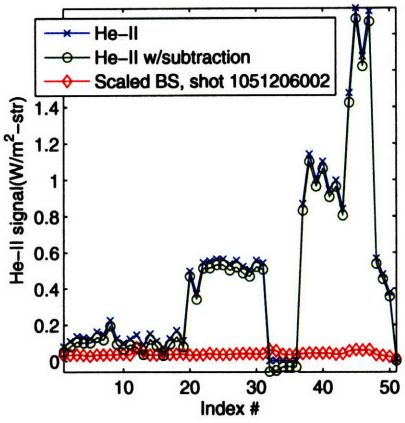

Figure D-3: HeII signals for shots in table D.1 with bremsstrahlung background subtraction based on shot 1051206002. There is no HeII signal for index 32-36; these are not used for the scatter plot.

D.3.2 Scaling Models

As discussed, the HeII diode signal is typically dominated by emission from the edge of the plasma, specifically at the LCFS and in the SOL layer. This 4→3 HeII line stems from de-excitation of electron-impact excited He^{+1} ions. Mathematically, the number of 4686 Å photons per second per m^2str hitting the detector is:

$$\gamma = \int n_e n_{He^{1+}} \langle \sigma v \rangle_{e-ex} \, B dl \tag{D.1}$$

where n_e and $n_{He^{1+}}$ are the electron and hydrogen-like helium density, $\langle \sigma v \rangle_{e-ex}$ the electron-impact excitation rate of ground state He^{1+} to the n=4 level, B is the n=4→3 branching ratio, and the integral is taken over the sightline. Again, the diode signal is γ and given in Watt/m^2str.

Because the SOL and LCFS typically have temperatures greater or near the ionization energy of He^{+1} and neutral He (~54 eV), the helium population in these regions are overwhelmingly He^{+2} ions. The ionization mechanism is predominantly electron-impact ionization. Hence, if CX dominates, the He^{+1} population can be estimated via:

$$n_{He^{1+}} = \frac{\sum_s n_{He^{2+}} n_s \langle \sigma v \rangle_{cx-s}}{n_e \langle \sigma v \rangle_{ei}} \tag{D.2}$$

where the sum is taken over all electron donors, and the denominator consists of the electron impact destruction term. The electron donor is dominantly neutral deuterium, but non-fully stripped impurities can also contribute. On the other hand,

if radiative recombination determines the He^{+1} population, then:

$$n_{He^{1+}} = \frac{n_{He^{2+}} \langle \sigma v \rangle_R}{\langle \sigma v \rangle_{ei}} \tag{D.3}$$

These equations result in two different scalings for the HeII emission. For CX, substituting equation D.2 into equation D.1 and solving for $n_{He^{2+}}$ result in:

$$\frac{n_{He^{2+}}}{n_e} = \kappa_{cx} \frac{\gamma}{n_e^2 T_e^{1.5} Z_{\text{eff}}} \tag{D.4}$$

where $\langle \sigma v \rangle_{cx}$ is assumed to scale as $T_e^{1.5}$ since at temperatures below 1 keV the neutral D-He^{2+} CX cross section increases linearly with collisional energy, and the Z_{eff} term is meant to account for electrons from non-fully stripped ions. κ_{cx} is the constant determined by the available helium concentration data.

For radiative recombination, using Hutchinson's recombination rate formula(equation 6.3.27)[38] and neglecting the terms in the bracket, the scaling becomes:

$$\frac{n_{He^{2+}}}{n_e} = \kappa_{re} \frac{\gamma T_e^{0.5}}{n_e^2} \tag{D.5}$$

where κ_{re} is again the constant determined by the available helium concentration data.

Based on quick estimates, the He^{1+} density should be dominated by CX from neutral D, and equation D.4 should be the right scaling.

In order to verify the CX scaling, the RF inferred Helium data is plotted for both scalings using core and edge plasma parameters. For the core, the TCI averaged density, Thomson scattering peak temperature, and average Z_{eff} are used. For the edge, the Thomson density and temperature values at r=89 cm are used. This result in 4 scatter plots given by Figure D-4. Clearly, the radiative recombination scaling using either edge or core plasma parameters does not reconcile the LSN, USN, and IWL data. The CX scaling using core plasma parameter reveal a linear scaling for the LSN and USN data with relatively large scatter. A linear fit to determine κ_{cx} using only the diverted discharge data provide a κ_{cx}=9.26 m^2-str-$(m^3)^2$-$keV^{1.5}$/Watts calibration for the HeII diode when core n_e in $10^{20}/m^3$ and T_e in keV are used for equation D.4. Finally, the LSN, USN, and IWL data can be reconciled with significant scatter if edge parameters are used with the CX scaling. This results in a linear fit of $\kappa_{cx} = 5.4 \times 10^{-3}$ m^2-str-$(m^3)^2$-$keV^{1.5}$/Watts for edge n_e in $10^{20}/m^3$ and T_e in keV . Both of these core and edge linear fits have forced zero intercepts, representing

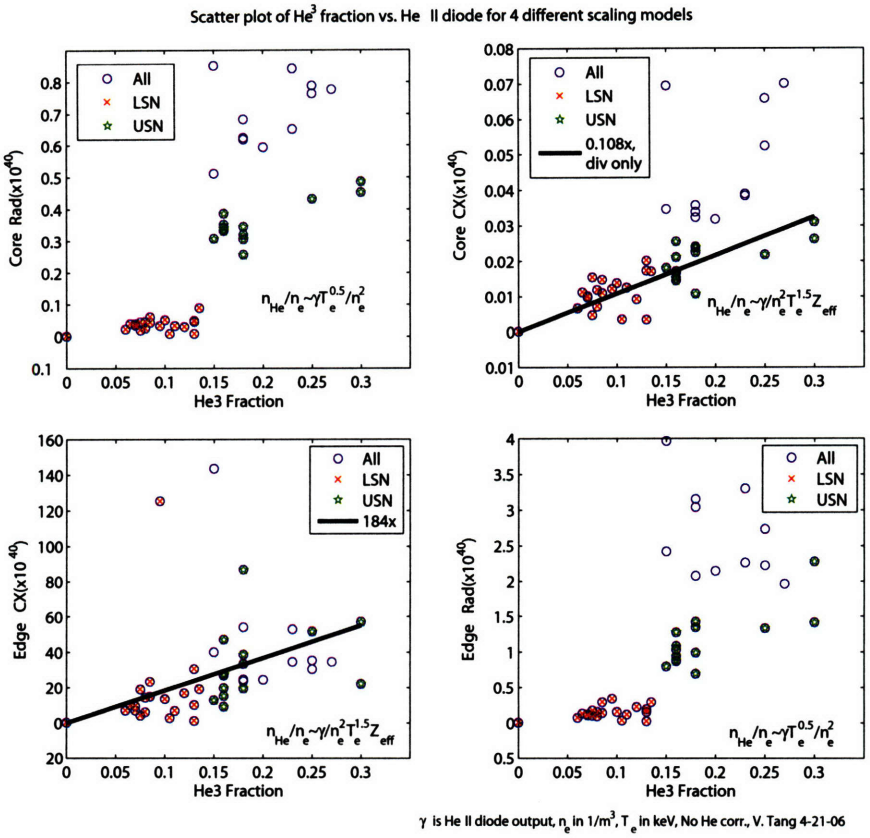

Figure D-4: Scatter plots for 4 different scaling models

zero helium fractions for zero signal after background bremsstrahlung subtraction. However, the two scalings do not give the same estimate of n_{He}/n_e; the edge based one which reconciles the IWL data usually results in a significantly lower estimate. The core base scaling gives realistic numbers for the LSN and USN shots.

Because of the large scatter, the error in using the CX scaling to infer helium concentration is high. For both scalings, an error of at least $\sim$30% is expected.

Further work, perhaps in conjunction with a simulated diode diagnostic, is necessary to narrow this error. Also, more data over wider plasma parameters would be useful.

Bibliography

[1] http://www.iter.org.

[2] M. Greenwald et al. Overview of Alcator C-Mod Program. *Nucl. Fusion*, 45:S109, 2005.

[3] John Wesson. *Tokamaks.* The International Series of Monographs on Physics, 118. Oxford University Press, third edition, January 2004.

[4] J.D. Lawson. Some criteria for a useful thermonuclear reactor. Technical report, United Kingdom Atomic Energy Research Establishment, 1955.

[5] F. Najmabadi et al. The ARIES-AT advanced tokamak, Advanced technology fusion power plant. *Fusion Engineering and Design*, 80:3–23, 2006.

[6] J.D. Lindl et al. The physics basis for ignition using indirect-drive targets on the National Ignition Facility. *Physics of Plasmas*, 11, 2004.

[7] International Fusion Research Council. Status report on fusion research. *Nuclear Fusion*, 45:A1–A28, 2005.

[8] http://www.jet.efda.org.

[9] P. O'Shea. *Measurements of ICRF power deposition and thermal transport with an ECE grating polychromator on the Alcator C-Mod tokamak.* PhD thesis, Massachusetts Institute of Technology, June 1997.

[10] K.G. McClements et al. Interpretation of Measurements of ICRF Heated Minority Proton Distributions in JET. *Nuclear Fusion*, 37:473, 1997.

[11] M. P. Petrov, R. Bell, R. V. Budny, N. N. Gorelenkov, S. S. Medley, R. B. White, and S. J. Zweben. Effective temperatures, sawtooth mixing, and stochastic diffusion ripple loss of fast H^+ minority ions driven by ion cyclotron heating in the Tokamak Fusion Test Reactor. *Physics of Plasmas*, 6:2430–2436, June 1999.

[12] G. W. Hammett. *Fast Ion Studies of Ion Cyclotron Heating in the PLT Tokamak.* PhD thesis, Princeton University, March 1986.

[13] R. J. Fonck, D. S. Darrow, and K. P. Jaehnig. Determination of plasma-ion velocity distribution via charge-exchange recombination spectroscopy. *pra*, 29:3288–3309, June 1984.

[14] A. L. Roquemore, G. Gammel, G. W. Hammett, R. Kaita, and S. S. Medley. Application of an E|| B spectrometer to PLT charge-exchange diagnostics. *Review of Scientific Instruments*, 56:1120–1122, May 1985.

[15] V. G. Kiptily, S. Popovichev, S. E. Sharapov, L. Bertalot, F. E. Cecil, S. Conroy, and M. J. Mantsinen. Gamma-diagnostics of alpha-particles in ^{4}He and D-T plasmas. *Review of Scientific Instruments*, 74:1753–1756, March 2003.

[16] E.F. Jaeger et al. Sheared Poloidal Flow Driven by Mode Conversion in Tokamak Plasmas. *Physical Review Letters*, 90(19), May 2003.

[17] R.W Harvey and M.G. McCoy. The CQL3D Fokker-Planck Code. Technical Report Montreal Canada, IAEA TCM Advances in Simulation and Modeling of Thermonuclear Plasmas, 1992.

[18] M. Brambilla. Numerical simulation of ion cyclotron waves in tokamak plasmas. *Plasma Physics and Controlled Fusion*, 41:1–34, January 1999.

[19] T. H. Stix. Fast-wave heating of a two-component plasma. *Nuclear Fusion*, 15:737–754, October 1975.

[20] R. S. Granetz, C-Mod DNB Group, and A. A. Ivanov. A Long-pulse Diagnostic Neutral Beam for Alcator C-Mod. *APS Meeting Abstracts*, page 1013, October 2003.

[21] N.P. Basse et al. Diagnostic Systems on Alcator C-Mod. To be published.

[22] T.H. Stix. *Waves in Plasmas.* 1992.

[23] P.L. Colestock and V.L. Granatein. *Wave Heating and current Drive in Plasmas.* Gordon and Breach, 1985.

[24] M. Porkolab. Plasma heating by fast magnetosonic waves in tokamaks. Technical Report PFC/JA-93-19, MIT PSFC, 1994.

[25] F.W. Perkins. ICRF Heating Theory. *IEEE Transactions on Plasma Science*, 12, 1984.

[26] E.F. Jaeger. Quasilinear evolution of non-thermal ion distributions in ion cyclotron resonance heating. Presentation, 2006. SciDac Conference.

[27] C. S. Chang and P. Colestock. Anisotropic distribution function of minority tail ions generated by strong ion-cyclotron resonance heating. *Physics of Fluids B*, 2:310–317, February 1990.

[28] P.J. Catto et al. A quasilinear, Fokker-Planck description of fast wave minority heating permitting off-axis tangency interactions. *Physics of Plasmas*, 1, 1994.

[29] W.W. Heidbrink and G.J. Salder. The behaviour of fast ions in tokamak experiments. *Nuclear Fusion*, 34, 1994.

[30] A.P. Smirnov and R.W. Harvey. The Genray Ray Tracing Code. Technical Report CompX-2000-01,Ver. 2, CompX, March 2003.

[31] K. Shinohara, D. S. Darrow, A. L. Roquemore, S. S. Medley, and F. E. Cecil. Solid state neutral particle analyzer array on national spherical torus experiment. *Review of Scientific Instruments*, 75:3640–3642, October 2004.

[32] R. O'Connell et. al. Measurement of fast electron distribution using a flexible, high time resolution hard x-ray spectrometer. *Rev. Sci. Instrum.*, 74(3):2001–2003, March 2003.

[33] Glenn F. Knoll. *Radiation Detection and Measurement.* Wiley, third edition, December 1999.

[34] J.F Ziegler, J.P. Biersack, and U. Littmark. *The Stopping and range of Ions in Solids.* Pergamon Press, 2nd. edition, 2003.

[35] J.E. Liptac. *Lower Hybrid Modeling and Experiments on Alcator C-Mod.* PhD thesis, Massachusetts Institute of Technology, 2006.

[36] H.O. Funsten et al. *IEEE Trans. Nuc. Sci.*, 48, 2001.

[37] http://w3.pppl.gov/ pshare/help/transp.htm.

[38] I. H. Hutchinson. *Principles of Plasma Diagnostics.* Cambridge University Press, 2002.

[39] A. A. Korotkov, A. Gondhalekar, and A. J. Stuart. Impurity Induced Neutralization of Megaelectronvolt Energy Protons in JET Plasmas. *Nuclear Fusion*, 37:35–51, 1997.

[40] T.G. Winter. Electron transfer and ionization in collisions between protons and the ions He^+, Li^{2+}, Be^{3+}, B^{4+}, and C^{5+} studied with the use of a Sturmian basis. *Physical Review Letters A*, 35:3799–3809, May 1987.

[41] S. S. Medley, M. P. Petrov, A. L. Roquemore, and R. K. Fisher. Operation of the TFTR pellet charge exchange diagnostic in the pulse counting mode during H^+ radio frequency minority heating. *Review of Scientific Instruments*, 70:841–844, January 1999.

[42] V. I. Afanassiev, Y. Kusama, M. Nemoto, T. Kondoh, S. Y. Petrov, S. S. Kozlovskij, M. Satoh, A. Morioka, Y. Tsukahara, T. Nishitani, H. Kimura, K. Hamamatsu, S. Moriyama, M. Saigusa, and T. Fujii. Neutral particle analysis in MeV energy range and relative role of He^+ and C^{5+} ions in fast proton neutralization in ICRF and combined ICRF/NBI-heated JT-60U plasmas. *Plasma Physics and Controlled Fusion*, 39:1509–1524, October 1997.

[43] S. Tamor. *J. Comput. Phys.*, 40:104, 1981.

[44] J. E. Rice, F. Bombarda, M. A. Graf, E. S. Marmar, and Y. Wang. Observations of Alcator C-Mod plasmas from a five chord high energy resolution x-ray spectrometer array. *Review of Scientific Instruments*, 66:752–754, January 1995.

[45] R.K. Janev et al. Penetration of energetic neutral beams into fusion plasmas. *Nuclear Fusion*, 29:2125, 1989.

[46] B. Lipschutlz and K. Marr. Private communication.

[47] M. J. May, K. B. Fournier, J. A. Goetz, J. L. Terry, D. Pacella, M. Finkenthal, E. S. Marmar, and W. H. Goldstein. Intrinsic molybdenum impurity density and radiative power losses with their scalings in ohmically and ICRF heated Alcator C-Mod and FTU tokamak plasmas. *Plasma Physics and Controlled Fusion*, 41:45–63, January 1999.

[48] D.A. Pappas et al. Molybdenum sources and transport in the alcator c-mod tokamak. Technical Report JA-99-10, MIT PSFC, 1999.

[49] M. J. May, A. P. Zwicker, H. W. Moos, M. Finkenthal, and J. L. Terry. MLM-based monochromator for molybdenum impurity monitoring on the Alcator C-MOD tokamak in the 30-130 Å range. *Review of Scientific Instruments*, 63:5176–5178, October 1992.

[50] A. Parisot. Private communication.

[51] E.F. Jaeger et al. Quasiliner evolution of non-thermal distributions in ion cyclotron resonance heating of tokamak plasmas. *Plasma Physics and Controlled Fusion*, 2006(To be submitted).

[52] C.K. Philips and P.T. Bonoli. Private communication.

[53] R. S. Granetz. Private communication.

[54] M. Choi, V. S. Chan, R. I. Pinsker, C. C. Petty, S. C. Chiu, J. Wright, P. Bonoli, and M. Porkolab. Simulation of fast Alfvén wave interaction with beam ions over a range of cyclotron harmonics in DIII-D tokamak. *Nuclear Fusion*, 46:409–+, July 2006.

[55] Kenneth S. Krane. *Introductory Nuclear Physics.* John Wiley and Sons, 1988.

[56] J.R. Lamarsh and A.J. Baratta. *Introduction to Nuclear Engineering.* Prentice Hall, 3rd. edition, 2001.